Extending Scatterometry to emerging Industrial Sectors

Author:
Jonas Skovlund Møller Madsen

Supervisors:
Poul Erik Hansen
Søren Alkærsig Jensen
Jesper Nygård

This thesis has been submitted to the PhD School of The Faculty of Science, University of Copenhagen
Ph. D. in Physics

A collaboration between:
DFM A/S
Niels Bohr Institute - University of Copenhagen

Contents

Abstract

Advances in nanotechnology research promise new and old products embedded with the technology of the future. However, for this technology to successfully penetrate the market, it needs to be accompanied by relevant metrology. This thesis presents part of the work done at the scatterometry group at DFM. In Scatterometry, a nanostructured surface is reconstructed based on its optical signal through inverse modeling. The main focus is to investigate novel ways to apply scatterometry to two new emerging industries, namely: Nanostructured plastic and nanowires. The thesis starts off by introducing and motivating the work in Chapter 1 and continuous describing the theory of scatterometry in Chapter 2. A method to approximate grating defects based on a semi-analytical model and/or a neural network is demonstrated in Chapter 3. The semi-analytical model allows for increasingly complex structures to be modeled, without increasing the computation time. The neural network approach benefits from the current trends of "Internet of Things" and "Big Data". Chapter 4 introduces the concept of imaging scatterometry, a new user-friendly technique developed at DFM. The technique is compared to conventional spectroscopic scatterometry, atomic force microscopy, and confocal microscopy. An attempt to increase the wavelength range of the imaging scatterometer is described in Chapter 5. The thesis continues by presenting the work done concerning the characterization of nanostructured plastic under production in Chapter 6. Here it is shown how a scatterometer can be deployed at the fabrication site and used to characterize produced parts at a pace faster than they are fabricated and thus allowing for inline characterization. The developed scatterometer was operated by fabrication personnel. In this way over 250 nanostructured samples where characterized within hours. This immediate feedback also allowed the operators to change production parameters at the fly to optimize the process. Furthermore, it is demonstrated how imaging scatterometry can be used to measure the same samples. Chapter 7 is dedicated to metrological optimizations in scatterometry and Chapter 8 demonstrates how scatterometry can be combined with other measurement techniques to make a more robust reconstruction. The work on Nanowires is presented in Chapter 9. Here it is shown how imaging scatterometry can be used to determine if the different process steps in Molecular Beam Epitaxy has been successful or not. Scatterometry measurements on the final wires are presented at the end of the chapter. Here we see that we can characterize the wires using conventional scatterometry, but the imaging system lacks information to perform a robust reconstruction. Lastly, the work is concluded with a discussion of research topics for the future in Chapter 10.

Dansk Resume

Fremskridt i nanoteknologi lover nye, såvel som gamle, produkter med fremtidens teknologi. Før at denne teknologi succesfuldt kan komme på markedet, er det nødvendigt, at den bliver støttet af relevant metrologi. Denne afhandling præsenterer et udsnit af arbejdet udført i skatterometrigruppen på DFM. I skatterometri bliver en nanostruktureret overflade rekonstrueret baseret på dens optiske signal gennem inversmodellering. Afhandlingen fokuserer primært på to nye, frembrusende, industrier: nanostruktureret plastik og nanotråde. Afhandlingen starter med at introducere og motivere arbejdet i Kapitel 1 og fortsætter med at beskrive teorien bag skatterometri i Kapitel 2. En metode til at approksimere gitterdefekter, baseret på en semi-analytisk model og/eller et neuralt netværk, er demonstreret i Kapitel 3. Den semi-analytiske model gør det muligt at simulerer mere komplekse strukturer uden at forøge beregningstiden. Det neurale netværk gør brug af nutidige trends som "Internet of Things" og "Big Data". Kapitel 4 introducerer konceptet billeddannende skatterometri, som er en ny brugervenlig teknik som er udviklet på DFM. Teknikken sammenlignes med konventionel skatterometri, atomarkraft mikroskopi og konfokal mikroskopi. Et forsøg på at udvide den spektrale rækkevidden for det billeddannende skatterometer er beskrevet i Kapitel 5. Afhandlingen fortsætter med at præsentere arbejdet med karakterisering af nanostruktureret plastik under produktion i Kapitel 6. Her er det vist, hvordan et skatterometer kan blive anvendt i et produktionsmiljø til at karakterisere emner hurtigere, end de bliver produceret og derved tillade "in-line"-karakterisering. Det udviklede skatterometer blev betjent af produktionspersonel. På denne måde blev det brugt til at karakterisere over 250 nanostrukturerede emner på nogle timer. Den øjeblikkelige tilbagemelding gjorde det muligt for operatørerne at ændre produktionsparametre løbende for at optimere processen. Ydermere er det demonstreret, hvordan et billeddannende skatterometer kan blive brugt til at opmåle de samme emner. Kapitel 7 er dedikeret til metrologiske optimeringer af skatterometri, og Kapitel 8 demonstrerer, hvordan skatterometri kan blive kombineret med andre måleteknikker for at få en mere robust rekonstruktion. Arbejdet med nanotråde er præsenteret i Kapitel 9. Her bliver det vist, hvordan billeddannende skatterometri kan blive brugt til at bestemme, om forskellige procestrin i Molekylær Stråle Epitaksi er gået godt eller ej. Skatterometri-målinger på nanotråde er præsenteret sidst i kapitlet. Her ser vi, at vi kan karakterisere trådene ved at bruge konventionel skatterometri, men at det billeddannende system mangler information for at kunne udføre en robust rekonstruktion. Til slut bliver arbejdet konkluderet med diskussion af fremtidige forskningsemner i Kapitel 10.

List of Publications

[I] *Study on Micrograting Using Imaging, Spectroscopic, and Fourier Lens Scatterometry*
J. S. Madsen, P.E. Hansen P. Boher, D. Dwarakanath, J. F. Jørgensen, B. Bilenberg, J. Nygård and M. H. Madsen
Journal of Micro- and Nano-Manufacturing, vol. 5 (2017). (Preprint on page 38)

[II] *In-line characterization of nanostructured mass-produced polymer components using scatterometry*
J. S. Madsen, L. H. Thamdrup, I. Czolkos, P. E. Hansen, A. Johansson, J. Garnaes, J. Nygård and M. H. Madsen
Journal of Micromechanics and Microengineering, vol. 27, (2017). (Preprint on page 74)

[III] *Modeling surface imperfections in thin films and nanostructured surfaces*
P.-E. Hansen, **J. S. Madsen**, S. A. Jensen, M. H. Madsen, and M.Karamehmedovic
Proceedings of SPIE - International Society for Optical Engineering, (2017). (Manuscript not included in this thesis)

[IV] *Plasmonic color metasurfaces fabricated by a high speed roll-to-roll method*
S. Murthy, H. Pranov, N. A. Feidenhans'l, **J. S. Madsen**, P. E. Hansen, H. C. Pedersen, and R. Taboryski
Nanoscale, vol. 9 (2017). (Manuscript not included in this thesis)

[V] *Thickness and refractive index analysis of ellipsometry data of ultra-thin semi-transparent films*
P. E. Hansen and **J. S. Madsen**
Optical Society of America, (2018). (Manuscript not included in this thesis)

[VI] *Scatterometry for optimization of injection molded nanostructures at the fabrication line*
J. S. Madsen, S. A. Jensen, L. Nakotte, A. Vogelsang, L. H. Thamdrup, I. Czolkos, A. Johansson, J. Garnæs, T. Nielsen, J. Nygård and P. E. Hansen
The International Journal of Advanced Manufacturing Technology, vol. 9-12 (2018). (Preprint on page 88)

[VII] *Replacing libraries in scatterometry*
J. S. M. Madsen, S. A. Jensen, Jesper Nygård and P. E. Hansen
Optics Express, vol. 26 (2018). (Preprint on page 17)

[VIII] *Enhanced measurement accuracy using Hybrid Metrology and new Mueller polarimetry calibration method*
P. E. Hansen, S. R. Johansen and **J. S. M. Madsen**
(Submitted to Optics Express- manuscript not included in this thesis).

[IX] *Survey on Models for Light Propagation in Translucent Materials*
J. R. Frisvad, S. A. Jensen, **J. S. M. Madsen**, L. Yang, A. Correia, Y. Meuret, and P.-E. Hansen
(Submitted to EUROGRAPHICS state of the art reports - manuscript not included in this thesis).

List of Figures

Abbreviations

1D	One Dimensional
2D	Two Dimensional
AFM	Atomic Force Microscopy
BPF	Band Pass Filter
CAD	Computer Assisted Drawing
CCD	Charge Coupled Device
CPU	Computer Processing Unit
DFM	Danish Fundamental Metrology A/S
Diff. Eff.	Diffraction Efficiency
EBL	Electron Beam Lithography
EMA	Effective Medium Approximation
EMPIR	European Metrology Program for Innovation and Research
FEG	Field Emission Gun
FDTD	Finite Different Time Domain
FEM	Finite Element Method
FF	Filling Factor
FWHM	Full Width at Half Maximum
GUI	Graphical User Interface
HF	Hydrofluoric acid
Im. Scat.	Imaging Scatterometry
InAs	Indium Arsenide
ISO	International Organization for Standardization
LDLS	Laser Driven Light Source
LED	Light Emitting Diode
LSQ	Least Square Optimization
MBE	Molecular Beam Epitaxy
MetHPM	Metrology for Highly Parallel Manufacturing
NA	Numerical Aperture
NBI	Niels Bohr Institute
NILT	Nano Imprint Lithography Technology
PMMA	Poly(methyl methacrylate)
PSA	Polarization State Analyzer
PSG	Polarization State Generator
QDev	Center for Quantum Devices
RCWA	Rigorous Coupled Wave Analysis
SEM	Scanning Electron Microscopy
SC	Semi Conductor
Scat.	Scatterometry
Si(100)	Silicon with the (100) plane orthogonal to the reciprocal lattice vector
SiO_2	Silicon dioxide or Quartz
SPIP	Metrology Software from Image Metrology A/S
TE	Transverse Electric
TM	Transverse Magnetic
UV	Ultra Violet - light with a wavelength below the visible range.

Acknowledgements

The work presented in this thesis is the fruit of a successful collaboration between several people.
Jesper Nygård, thank you for initially suggesting the collaboration with the university and DFM that got me here. Thank you for backing up the suggested Ph.D. project and seeing it through to this day.
I thank Morten Hannibal Madsen for initiating this project. I wish you the best of luck in your future career!
Thanks to Rene Hansen at Michael Lundbech for teaching me about grinding and polishing of optical surfaces and for letting me borrow the equipment at your workshop. I am sure that your help has saved me many days if not weeks.
Thanks to Thomas Nordqvist for introducing me to the cleanroom facilities at NBI and sparing with me on how to best implement scatterometry at NBI and to Miķelis Marnauza for providing some excellent nanowires and corresponding SEM images.
Thanks to Lasse Højlund Thamdrup for getting the collaboration with NILT of to a good start with your enthusiasm and friendly personality. To Ilja Czolkos for helping out with testing the compact scatterometer both at DFM, DTU, and China and to Alicia Johanson for managing the exciting projects and ensuring a smooth collaboration between DFM and NILT.
Thanks to Mikael Østergaard Lassen for your great taste in music and high spirits - your playlists have made some long lab hours less tedious. To Bo Brøndsted, I am very grateful for your help in the tool shop and your answers to various of my stupid questions. To Jørgen Garnæs for providing training in AFM and answering my various metrology questions on the fly. Thanks to Sabrina Rostgaard Johannsen. Your cheerful personality has turned my frown to a smile several times, even when my code would not compile. To Anders Brusch for taking the time to help me with my various questions. To Jan Hald for bossing me around in a fair manner, I promise not to tell people that you are actually a pretty nice guy. A shout-out to the young blood at DFM for invigorating the workplace
Thanks to Søren Alkærsig Jensen for taking over as a supervisor after Morten left. A lot of the success of this project should be credited to you!
A huge thanks Poul Erik Hansen for your patience during my endless barrage of questions and guidance throughout this project. Without the spontaneous sparing sessions with you, I might not have distinguished the good ideas from the bad in time!
Lastly, to Christine and Julie for giving me a reason to get my work done in time and get home early, without your support this would not have been possible.

Summary of Papers

This section summarizes the papers included in this thesis. The papers are numbered based on their time of publication. Paper 1 is included in Chapter 4, Paper 2 and Paper 3 in Chapter 6 and Paper 4 in Chapter 3.

Paper 1 compares the two scatterometry techniques imaging and conventional spectroscopic scatterometry with confocal microscopy and atomic force microscopy (AFM). This is done by comparing the measured height of a one-dimensional silicon micro grating. The numerical aperture of the scatterometer instruments is reduced in order to avoid picking up higher diffraction orders. This enables the characterization of micro pitch gratings. Furthermore, results from a unique Fourier lens scatterometry system are demonstrated. In the paper, a height offset of 10 nm between the scatterometry techniques and the AFM was found. This offset could be corrected, by incorporating a more complex grating model with rounded corners. In the end, it is concluded that the scatterometers gives accurate estimates of the structure height and can be used for fast characterization of nanostructures.

Paper 2 demonstrates a scatterometer build in a transmission configuration. The scatterometer is deployed at a production facility, where it is used to characterize injection-molded nanostructures as they are produced. The replication fidelity as a function of the temperature is mapped for two polymers (Topas-5013 and Topas-8007). Here it is observed that if the cavity temperature is above the glass-transition temperature of the polymer, a good replication is achieved. Reference measurements, performed using AFM and SEM, shows a good agreement with the scatterometer results. The paper concludes that the instrument is suitable for in-line characterization of injection molded parts based on the accuracy and speed.

Paper 3 builds upon the results from Paper 2. A revised scatterometer is deployed at another production facility. Here, the instrument is used to create an injection molding recipe from scratch. The replication fidelity as a function of pressure and sample position is investigated. It is demonstrated that a high pressure is needed for a good replication. The replication fidelity is found to be similar at different areas of the sample. Furthermore, an imaging scatterometer is demonstrated to be capable of measuring the entire part with a single measurement. It is concluded that both instruments can be used for both optimization and quality control in injection molding.

Paper 4 demonstrates how sample defects can be incorporated into scatterometry. Three classes of defects are investigated. The first two classes concerns defects in the grating-superstrate interface and the third class the grating-substrate interface. The first two classes are well classified by a semi-analytical model. This semi-analytical model only requires a single RCWA calculation and is much faster than a standard library generation. The paper demonstrates how the third class can be characterized by deploying a neural network build from noisy simulations mimicking experimental data. Inverse modeling using the neural network is found to be faster and more robust than inverse modeling using a traditional library approach.

Chapter 1

Introduction

One could argue that the ability to measure and quantify is a prerequisite for civilization. We measure practically everything from the weight of our food, the distance between our homes and working spaces to the temperature in our rooms. These measurements help us in making decisions and, as a consequence, inaccurate measurements may lead to bad decisions. Lord Kelvin's statement is often paraphrased as: "*If you can measure something, you can make it better*". Metrology is concerned with providing accurate measurements and reporting them according to a common standardized system, in our case the SI-system. The SI-system dates back to the metre convention, signed in 1875, and was recently redefined (2019-05-20). By using this unified system we gain a common perception of measurements, which is essential for our global society. The work presented here is carried out in collaboration with the Danish National Metrology Institute (DFM), and therefore this research emphasizes metrology.

The work presented here is based on the basic principle of diffraction. Diffraction occurs when light encounters an obstacle, and was described centuries ago by D. Rittenhouse based on F. Hopkinsons observations of light through a handkerchief [1]. From this, a wave theory of light was formulated by T. Young in the following years [2]. This diffraction from grating structures has later been used for several applications concerning dimensional metrology. The concept of using scattered light in sub-micron metrology was pioneered by C. J. Raymond and co-workers in the late '80s and was named "scatterometry" [3].
In scatterometry, the optical signal from a nanostructured surface is measured and used together with optical simulations to determine the dimensions of the nanostructures through inverse modeling [4]. The workflow of scatterometry is sketched in figure 4.1. Today scatterometry is mainly used by experts in the semiconductor industry. Here scatterometry provides an accurate characterization of computer processor components with high throughput [5–7]. Most of the industrial research is, however, kept confidential. Therefore, it can be discouraging for new companies to set up their own scatterometry systems. However, the concept of scatterometry is not limited to semiconductor structures, and as nanostructured surfaces become gradually more interesting in other industries, the field of scatterometry could naturally be expanded to solve the metrology needs of these emerging products. Specifically, two new areas are investigated in this thesis, namely: Cheap nanostructures in plastic mass-produced by injection molding and nanowires fabricated by state-of-

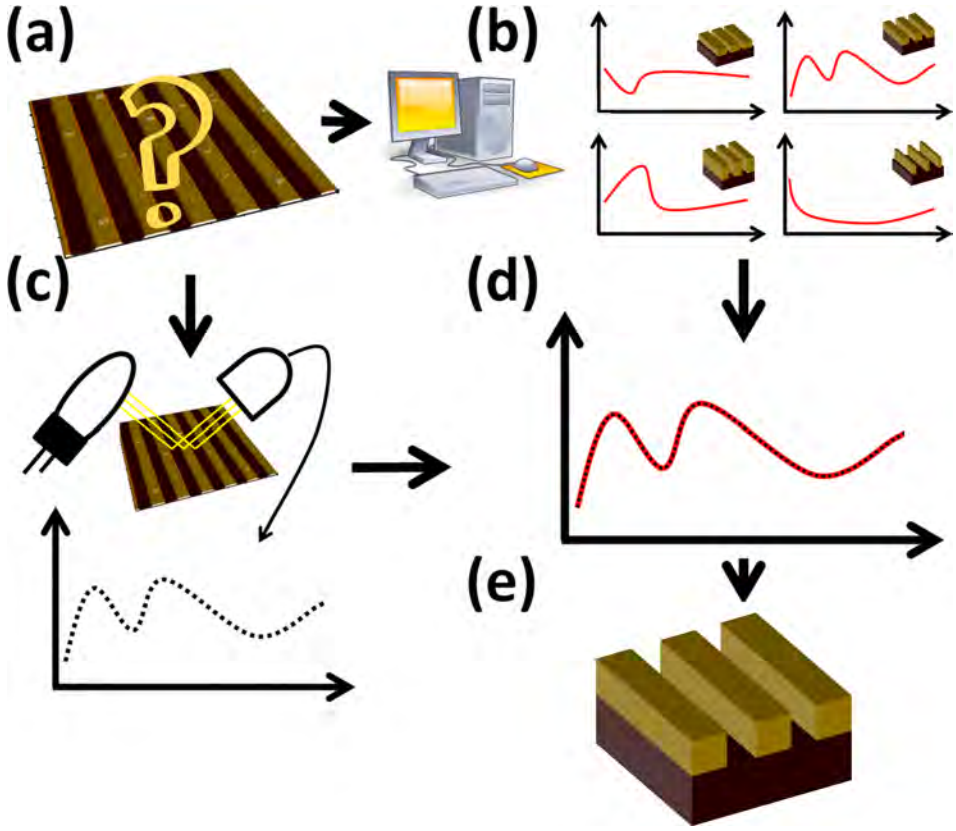

Figure 1.1: Schematic drawing of the working principle of scatterometry. (a)1D grating with an unknown structure. (b) An educated guess is used to model different grating structures, and their corresponding diffraction signals are simulated. Four examples are shown. The modeled grating structure is illustrated on the different diffraction signal graphs. (c) The sample is illuminated by a light source and the diffracted light is measured by a detector. This is used to find the experimental diffraction signal. (d) The experimentally measured diffracted signal is compared to all the simulated models and the best fitting model is found. (e) The structure of the best fitting model is extracted and assumed to describe the physical grating.

the-art molecular beam epitaxy. Scatterometry is fast, accurate and non-destructive but often does require the measured sample to be periodic. Even though un-periodic structures still have an optical diffraction signal, the requirement of periodicity rises from the numerical modeling of the surface. However, it is a common practice in the semiconductor industry to have dedicated test gratings on the produced sample, where scatterometry is performed for quality control, and thus this restriction is bypassed.

Gratings are on their own considered important optical elements in various industries (Optics [8], Diagnostics [9], Food science [10], Sensing [11] and Process Control [12]). Gratings have a few advantages over prisms: First, the grating dispersion depends on the period of the grating, which is easily manipulated, compared to the prism, where the dispersion depends on the material. Secondly, the prism is a bulk device, where the grating is a plane device. Lastly, the reflection grating can be used for wavelength below 200 nm, where glass stops being transparent.

The thesis is outlined in the following way:

- Chapter 1 (this chapter) introduces and motivates the work.
- Chapter 2 goes through the steps performed in scatterometry and gives a general introduction to the technique.
- Chapter 3 goes into a bit more detail with the simulation method used in this work and presents Paper 4.
- Chapter 4 explains the idea behind imaging scatterometry and moves on to present Paper 1.
- Chapter 5 introduces the theory behind the Lyot filter used in imaging scatterometry and demonstrates how a custom filter is produced to increase the measurement range of the system.
- Chapter 6 presents the work done on injection-molded nanostructures, including Paper 2 and Paper 3.
- Chapter 7 shows how uncertainties from scatterometry can be rigorously propagated to the evaluated model parameters using a general least square optimization and introduces Tinkhonov regularizations which are used in the following chapter.
- Chapter 8 reports a method to combine scatterometry with other characterization methods.
- Chapter 9 outlines the work on MBE fabrication steps and nanowires.
- Chapter 10 gives an outlook on future projects before the thesis is concluded.

Chapter 2

Scatterometry Method

When light impings on a periodic structure forming a diffraction grating, it causes a number of diffraction spots based on the ratio between the wavelength, λ, and the period of the structure, Δ, as described by the grating equation [13]:

$$n \cdot \lambda = \Delta\big(\sin(\theta_{in}) + \sin(\theta_{out})\big) \tag{2.1}$$

Here n is the order of the diffraction spot and θ_{in} and θ_{out} are the angle of incidence and the angle of the outgoing beam, both measured with respect to the sample normal. Furthermore, the magnitude of the different orders depends on the material and topography of the structure. This is the key principle in scatterometry: If we are able to simulate and measure the diffraction orders, we can reconstruct the physical structure through inverse modelling. In this chapter, the three main steps in scatterometry are explained: 1) Data acqusition, 2) Simulation and 3) Inverse modelling. Each step has a dedicated section. Section four briefly touches on direct optimization, and lastly the shortcomings of scatterometry are discussed.

2.1 Data Acquisition

To measure the diffraction efficiency at a given wavelength, $\eta(\lambda)$, one measures the ratio of the intensity of the diffracted light, I_j, compared to the intensity of the incoming light, I_I, [14]:

$$\eta_j(\lambda) = \frac{I_j}{I_I} \tag{2.2}$$

Where the index j indicates the diffraction order.
In most cases, we measure the undiffracted light ($j = 0$), when doing spectroscopic scatterometry. In this thesis $\eta(\lambda)$ is used as a shorthand notation for $\eta_0(\lambda)$. This light carries information similar to the other diffraction orders, but the direction of the diffracted light does not change with the period of the examined structure, making the instrumentation simpler. The measured light from the sample is referred to as a sample measurement, $I_{\text{Sample}}(\lambda)$, and the measurement of the incoming light is referred to as a reference measurement, $I_{\text{Ref}}(\lambda)$. In order to correct for stray light and dark counts in our system, a dark measurement, $I_{\text{Dark}}(\lambda)$, is performed as well.

Given these three measurements the diffraction efficiency can be calculated as:

$$\eta(\lambda) = \frac{I_{\text{Sample}}(\lambda) - I_{\text{Dark}}(\lambda)}{I_{\text{Ref}}(\lambda) - I_{\text{Dark}}(\lambda)} \tag{2.3}$$

if the reference measurement is performed by letting a detector directly measure the incoming beam, or:

$$\eta(\lambda) = \frac{I_{\text{Sample}}(\lambda) - I_{\text{Dark}}(\lambda)}{I_{\text{Ref}}(\lambda) - I_{\text{Dark}}(\lambda)} \cdot R(\lambda) \tag{2.4}$$

if the reference measurement is measured in reflectance mode on a reference material with known reflectance, $R(\lambda)$. An example of such intensity measurements can be seen in figure 2.1.

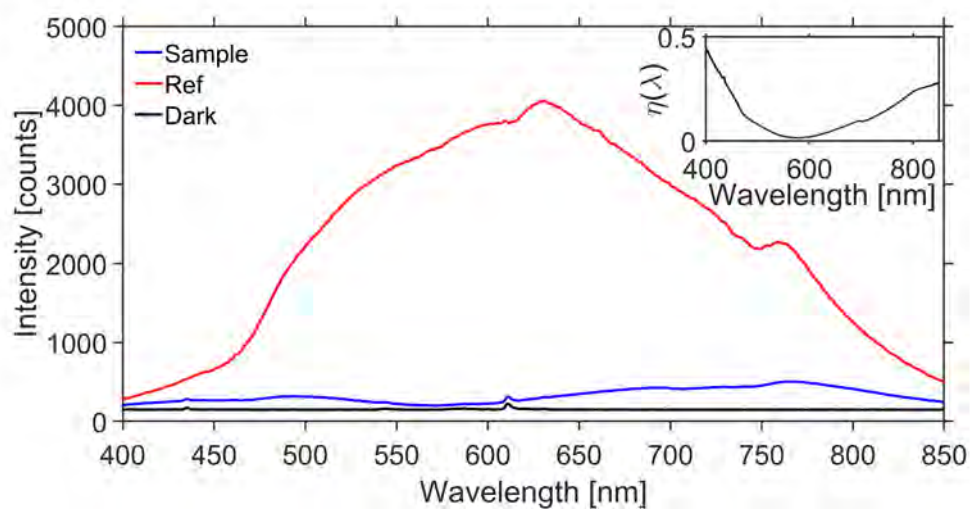

Figure 2.1: Intensity measurements performed on a 1D grating in plastic. Insert in the upper right shows the found diffraction efficiencies from the measurements.

In this thesis, these intensities are measured as a function of wavelength, by using either a spectrometer or a hyperspectral camera. This is referred to as spectroscopic scatterometry. The same could be done by measuring the intensities as a function of angles [15]. This is called angular resolved scatterometry. A similar approach could be used where $\eta(\lambda) \rightarrow \eta(\theta)$, here theta could refer to the incoming angle, the scattered angle or both (2-θ configuration).

2.2 Simulation

The first simulation step is to parametrize the sample under investigation. This is done by choosing a set of model parameters $\boldsymbol{\alpha}$. As an example, a rectangular grating described by a period, Δ, a height, h, and a width w is sketched in figure 2.2, hence $\boldsymbol{\alpha} = \boldsymbol{\alpha}(\Delta, h, w)$. Several different approaches exists to model the optical signal $f(\boldsymbol{\alpha})$ from a diffraction grating based on its structure, a selected few are discussed in this section. Typically, the calculated diffraction efficiencies, found

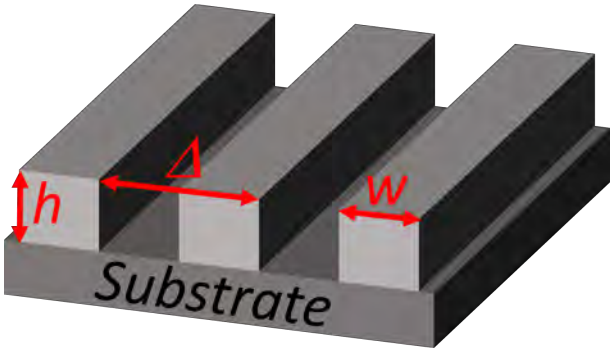

Figure 2.2: Sketch of a simple grating described by by a period, Δ, a height, h, and a width w.

from different permutations of model parameters, are stored in a database where they can be extracted later to be used in the inverse modeling. Some simulation methods are outlined in the following.

Scalar diffraction theory is a full analytical method to calculate the response from a grating [16]. It is, however, only valid for simple one dimensional structures (perfect rectangles and sinusoidals) where the grating period is similar or larger than the wavelength of the used light [17]. In the low period regime, Maxwells equations must be solved rigorously according to their full vector nature.

Rigorous coupled wave analysis (RCWA) is the approach used throughout this thesis. It provides a good trade-off between structure complexity, calculation speed and accuracy. The Method allows for calculations of the near field, which in some resonant cases can have effects propagating to the far field. The method has its own chapter (Chapter 3) and will not be further discussed here, but the interested reader is suggested to read refs [4, 18, 19].

In the cases where the wavelength of the light is much larger than the structures examined, the structures appear invisible to the light and analytical methods such as Effective Medium Approximations (EMA) can be used. This approach assumes an average refractive index in an area containing sub wavelength structures. [20, 21].

Finite difference time domain (FDTD) calculates the electric and magnetic fields at a given point, and advances them in small time and spatial steps according to Maxwells equations [22, 23]. It is most efficient when the examined structure geometries are similar to the wavelength of the use light [24]. This technique can handle multiple wavelengths simultaneously, but requires a very large grid if one wants to

calculate diffraction efficiencies in the far field, which in turn increases the computation time.

The Finite element method (FEM) [25] works by dividing the structure into a mesh of smalller structures such as triangles or other polynomial functions. This method allows for very complex geometries and some software packages allows for geometries to be defined by CAD files. The trade-off comes at a high computation time, and therefore other approaches are advised when generating large libraries.

Lastly, the emperical method is mentioned. This method entirely avoids any simulation, by comparing the optical response from a sample to a "golden reference" (typically a response from a sample which has been deemed acceptable based on specific tolerances). While this is not a "simulation" approach, it is still considered here since it is widely deployed in the industry due to its simplicity. This approach could further be developed by collecting signals from samples with know geometries and storing these in a database for later use. Ultimately, a neural network could be developed to characterize the samples as suggested in Paper 4.

In the presented work RCWA is used exclusively due to a good comprise of accuracy, speed and flexibility.

2.3 Inverse Modeling

Once we have our experimentally measured diffraction efficiencies and a library of different simulated diffraction efficiencies, the inverse modeling can be solved.
Inverse modelling uses an objective function, which is minimized, or maximized by adjusting the model function parameters. In the presented work, the measured diffraction efficiencies are compared to the simulated efficiencies using a chi-square optimization approach:

$$\chi^2 = \frac{1}{N}\sum_{i=1}^{N}\left(\frac{\eta(\lambda_i) - f(\mathbf{\Omega}_i, \boldsymbol{\alpha})}{\delta\eta(\lambda_i)}\right)^2 \tag{2.5}$$

Where N is the number of measurements, $\eta(\lambda_i)$ is the diffraction efficiency of the i'th measurement, $f(\mathbf{\Omega}_i, \boldsymbol{\alpha})$ is the simulated efficiency using the model parameters $\boldsymbol{\alpha}$ and the experimental condition of the i'th measurement, $\mathbf{\Omega_i}$. $\delta\eta_i$ is the uncertainty of the i'th measurement. $\delta\eta(\lambda_i)$ is found by using the law of combination of errors [26], based on estimated experimental errors from the sample, reference and dark measurements. The model parameters $\boldsymbol{\alpha}$ resulting in the lowest χ^2 is chosen as the parameters best describing the grating. An example of a reconstruction can be seen in figure 2.3. The user should be warned, that the method always finds a best fitting solution, no matter how physical that solution might be. It should also be stressed that it is essential that the "true" value of the examined structural parameters are within the ranges defined by the library. to estimate the precision of the reconstructed parameters, the 95% confidence interval is used [27]. This is done using chi-square boundaries $\Delta\chi^2 = \chi^2 - \chi^2_{\text{min}}$ for each fitted model. $\Delta\chi^2 < k^2$ should be fulfilled to obtain the confidence intervals of 68% ($k = 1$), 95% ($k = 2$), 99.7% ($k = 3$) and so forth, assuming a gaussian distribution. It is stressed that

these confidence intervals only gives an estimate of the parameters $\boldsymbol{\alpha}$. An example of how $\Delta\chi^2$ changes with different model parameters can be seen in the right part of figure 2.3.

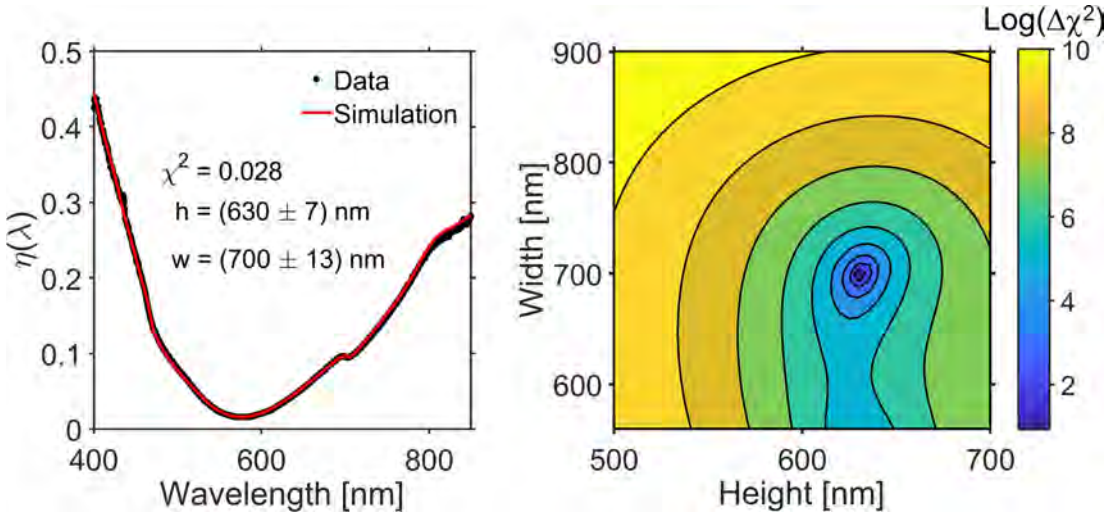

Figure 2.3: Reconstruction of the sample parameters from the data shown in figure 2.1. (Left) Measured diffraction efficiencies (black dots) and the best fitting simulated model (red line) a good agreement is seen. The χ^2, the height and the width are stated in the center. (Right) $\Delta\chi^2$ as a function of the simulated model parameters. It is observed that the agreement between model and data becomes gradually worse as model parameters changes from the found solution.

Uncertainties of the measurements also depend on other parameters such as detector noise, polarization of the light, incident angle. These parameters and their associated uncertainties are not commonly considered when performing scatterometry [4]. Unfortunately, it is not trivial to track how these experimental uncertainties affect the inverse modelling. Therefore, obtaining traceable uncertainties for the estimated topological parameters of the sample remains a problem in the world of scatterometry. The first steps towards a reference standard for scatterometry was recently presented [28]. An approach to include uncertainties in scatterometry measurements is described in Chapter 7. This method does, however, require that one knows the uncertainties of all relevant parameters.
The presented method works by direct optimization as described in the next section.

2.4 Direct Optimization

In the case of excessive computation power or loose restrictions on computation time, a direct optimization can be performed. This can especially be useful when using computational light simulations such as scalar diffraction. The direct optimization takes an initial guess of the sample parameters to be reconstructed and iteratively changes each parameter to see if another permutation of parameters gives a better solution to the inverse problem. Different methods to determine how the parameters are changed exist, a general least square method [29] is shown in Chapter 7, while a Levenberg Marquardt method [30, 31] is used in Chapter 9.
The Levenberg Marquardt algorithm is a combination of the gradient descend method and the Gauss Newton method as shown in the following. Optimization can always be rephrased as a minimization problem for a cost function $h(\alpha)$, depending on data and model parameters α. A standard gradient descent optimization method would change the value of α according to:

$$\alpha_{t+1} = \alpha_t - \frac{\partial h}{\partial \alpha} \tag{2.6}$$

where t is and iteration parameter. In the Gauss Newton method, the step size is scaled with respect to the second derivative in order to avoid overshooting:

$$\alpha_{t+1} = \alpha_t - \left(\frac{\partial^2 h}{\partial \alpha^2}\right)^{-1} \cdot \frac{\partial h}{\partial \alpha} \tag{2.7}$$

This makes intuitively sense, by considering that a larger second derivative would correspond to a fast changing function and therefore smaller steps would be ideal. The second order derivative is numerically estimate as the Hessian $\boldsymbol{J}^T\boldsymbol{J}$, where $\boldsymbol{J}$ is the Jacobian of the cost function:

$$\alpha_{t+1} = \alpha_t - \left(\boldsymbol{J}^T\boldsymbol{J}\right)^{-1} \cdot \frac{\partial h}{\partial \alpha} \tag{2.8}$$

This method is refereed to as the called Gauss-Newton method. The Levenberg Marquardt algorithm is skeptical with the regards to the stability of the Hessian and therefore adds a dampening term, λ:

$$\alpha_{t+1} = \alpha_t - \left(\boldsymbol{J}^T\boldsymbol{J} + \lambda \boldsymbol{I}\right)^{-1} \cdot \frac{\partial h}{\partial \alpha} \tag{2.9}$$

In the case, where λ is large, the method goes towards the gradient descent method and when λ is small it goes towards the Gauss Newton method. Typically a large initial value of λ is used. If a step t causes h to increase, λ is increased, otherwise λ is decreased to go towards the Gauss Newton method. For small diagonal($\boldsymbol{J}^T\boldsymbol{J}$) larger steps is preferred for speed so a final adjustment is made:

$$\alpha_{t+1} = \alpha_t - \left(\boldsymbol{J}^T\boldsymbol{J} + \lambda \cdot \mathrm{Diag}(\boldsymbol{J}^T\boldsymbol{J})\right)^{-1} \cdot \frac{\partial h}{\partial \alpha} \tag{2.10}$$

Arriving at the Levenberg Marquardt algorithm. Here Diag($\boldsymbol{J}^T\boldsymbol{J}$) is the diagonal elements of the Hessian. All in all the Levenberg Marquardt algorithm gives a good trade-off between the fast gradient descent method and a stable Gauss-Newton method.

The Levenberg Marquardt implementation changes the parameters in a bound interval defined by the user, while the general least square approach changes the parameters unbounded. It is shown that both methods converge towards a solution, given a good initial guess. A typical evolution of χ^2 from a direct optimization can be seen in figure 2.4.

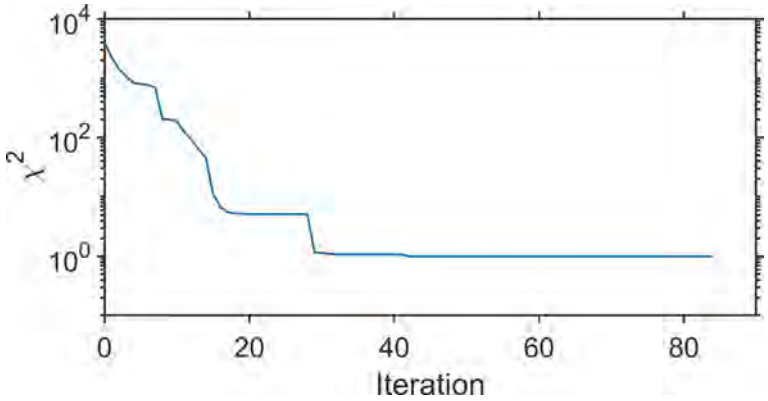

Figure 2.4: Evolution of χ^2 as a function of the iterations of direct optimization. Reconstructed sample consists of one dimensional lines in silicon.

2.5 Shortcomings

In order to determine if scatterometry is suitable for a given task, it is important to consider the shortcomings of scatterometry. Scatterometry is an indirect method, which relies on solving an inverse problem. This means that the solution depends on the chosen model (which should be the case for all sensible metrology!). For certain models, the solution may be ambiguous, with several different model parameters giving equally good fits for the measured data. A strong correlation between sidewall angle and height was reported in refs. [32]. This correlation between parameters was found to be the limiting factor for the accuracy of the reconstruction. In these cases it is necessary to do at least one of two things:

1) Reduce the amount variable model parameters, either by a priori knowledge or by other techniques. One could for example use AFM to lock the height or SEM to lock the pitch or width of the structure.
2) Increase the amount of independent data points, either by using an increased amount of wavelengths, or using data acquired from different angles of incidence and/or polarizations or data from different instruments.

Furthermore, scatterometry can only be used to measure periodic structures. This might seem like a big hurdle, but a common solution to this problem is to measure on designated test areas on the produced part, where grating structures is placed with parameters similar to the smallest produced features in the functional part. The basic assumption here is that the test areas are representative of the functional structures. This assumption is shown to be valid in the preprint of Paper 3, where it is seen that structures on different areas of the sample have the same degree of replication.

With the shrinkage of component sizes, it is desired to also reduce the test area. Using traditional scatterometry, the test area must be larger than the beam spot. This restriction can be overcome with the new imaging scatterometry technique seen in Paper 1 and Paper 3, at the cost of measuring speed.

Chapter 3

RCWA and Applications

As previously hinted, the heart of scatterometry is how the sample interacts with light. This can be simplified to how amplitudes of the incoming light are reflected and transmitted by the sample:

$$\begin{bmatrix} E_{\text{reflected},s} \\ E_{\text{reflected},p} \end{bmatrix} = \begin{bmatrix} r_{s\to s} & r_{p\to s} \\ r_{s\to p} & r_{p\to p} \end{bmatrix} \begin{bmatrix} E_{\text{in},s} \\ E_{\text{in},p} \end{bmatrix} \tag{3.1}$$

and

$$\begin{bmatrix} E_{\text{transmitted},s} \\ E_{\text{transmitted},p} \end{bmatrix} = \begin{bmatrix} t_{s\to s} & t_{p\to s} \\ t_{s\to p} & t_{p\to p} \end{bmatrix} \begin{bmatrix} E_{\text{in},s} \\ E_{\text{in},p} \end{bmatrix} \tag{3.2}$$

Where s and p denotes the polarization of the light (p for parallel and s for perpendicular with respect to the incidence plane). The subscript $i \to j$ refers to incident polarization i reflected or transmitted as polarization j. Typically in scatterometry, one measures the intensity reflection coefficient $R_{ss} = |r_{ss}|^2$ or $R_{pp} = |r_{pp}|^2$ in a reflection configuration or $T_{ss} = |t_{ss}|^2$ or $T_{pp} = |t_{pp}|^2$ in a transmission configuration. These quantities are then compared to simulations of the reflection or transmission. One way to perform these simulations is the Rigorous Coupled Wave Analysis (RCWA) method.
The first part of this chapter gives a short introduction RCWA and shows an example of the calculations of a simple grating. The second part is a preprint of Paper 4, where a method to handle defects using RCWA is shown.

3.1 Introduction

In RCWA, the simulated grating structures are approximated by a set of rectangular slabs [4]. A typical way to slice a trapezoidal grating is shown in figure 3.1. By using enough slabs strategically placed, any periodic surface can be created. However, increasing the amount of slabs used increases the amount calculations to be done, and therefore also the calculation time. As in most computational sciences, this ends up being a trade-off between accuracy and speed. It should be noted that the computation time does not increase drastically with the amount of slabs, so one should make sure to use enough. The simple rectangular form makes it simple to separate the spacial variables. By using Fourier expansions for the spacial periodic solution, we can transform the problem described by partial differential equations

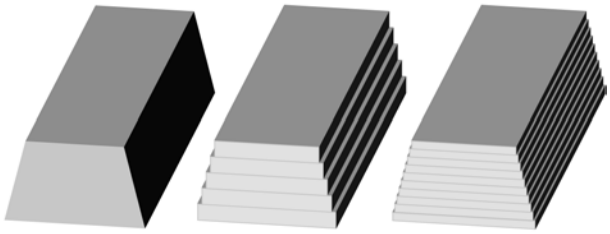

Figure 3.1: Trapezoidal grating (left) sliced into 5 (middel) and 10 (right) slabs.

into a set of ordinary differential equations for the Fourier amplitudes [19].
This gives an infinite continuous problem which must be discretized before it can be numerically solved. In RCWA, this is done by truncating the Fourier orders.

3.1.1 Example

Let us start at Maxwells equations:

$$\begin{aligned} \nabla \times \vec{E} &= -\mu \frac{\partial \vec{H}}{\partial t} & \nabla \cdot \vec{E} &= -\vec{E} \cdot \frac{\nabla \varepsilon}{\varepsilon} \\ \nabla \times \vec{H} &= \varepsilon \frac{\partial \vec{E}}{\partial t} + \sigma \vec{E} & \nabla \cdot \vec{H} &= 0 \end{aligned} \tag{3.3}$$

Here $\vec{E}$ and $\vec{H}$ are the electric and magnetic fields respectively, μ, is magnetic permeability, ε, is the electric permittivity and σ is the conductivity. Taking the curl of the two equations to the left, and using the following equations from vector calculus:

$$\begin{aligned} \nabla \times (\nabla \times \vec{A}) &= \nabla(\nabla \cdot \vec{A}) - \nabla^2 \vec{A} \\ \nabla \times (\phi \vec{A}) &= \phi(\nabla \times \vec{A}) + \nabla \phi \times \vec{A} \end{aligned} \tag{3.4}$$

We arrive at two equations:

$$\begin{aligned} \nabla^2 \vec{E} &= \varepsilon\mu \frac{\partial^2 \vec{E}}{\partial^2 t} + \sigma\mu \frac{\partial \vec{E}}{\partial t} - \nabla(\vec{E} \cdot \frac{\nabla \varepsilon}{\varepsilon}) \\ \nabla^2 \vec{H} &= \varepsilon\mu \frac{\partial^2 \vec{H}}{\partial^2 t} + \sigma\mu \frac{\partial \vec{H}}{\partial t} - \nabla\varepsilon \times \frac{\partial \vec{E}}{\partial t} - \nabla\sigma \times \vec{E} \end{aligned} \tag{3.5}$$

Next, we assume that the fields are time harmonic, meaning that they can be decomposed into spacial and time dependent parts:

$$\vec{A}(r,t) = A(r) \cdot e^{-i\omega t} \tag{3.6}$$

Here ω is the angular frequency of the field. For simplicity, let us assume that we have a non-conducting material such that $\sigma = 0$. Equations (3.5) now simplify to:

$$\begin{aligned} \nabla^2 \vec{E} &= -\varepsilon\mu\omega^2 \vec{E} - \nabla(\vec{E} \cdot \frac{\nabla \varepsilon}{\varepsilon}) \\ \nabla^2 \vec{H} &= -\varepsilon\mu\omega^2 \vec{H} - \frac{1}{\varepsilon} \nabla\varepsilon \times (\nabla \times \vec{H}) \end{aligned} \tag{3.7}$$

An example is given for the simple grating sketched in figure 3.2. Equations (3.7) are to be solved separately for each domain, and the integration constants will be determined by applying the condition that region I and region II should have the same solution at z=0 and region II and region III should have the same solution at z=h.

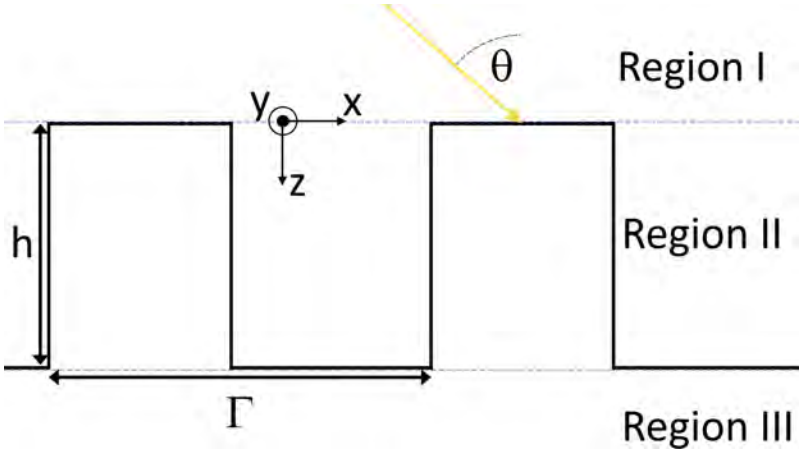

Figure 3.2: Sketch of simple rectangular grating.

Taking the light to be polarized in the transverse electric polarization $\vec{E} = (0, E_y, 0)$, the equation for the electric field reduces to the Helmholtz equation:

$$\nabla^2 E_y = -\varepsilon\mu\omega^2 E_y \tag{3.8}$$

Here ε is constant in region I and III and a step function in x for region II. For the remainder of this chapter, μ is assumed to be μ_0 so: $\nabla^2 E_y = -(n\frac{2\pi}{\lambda})^2 E_y$, Where n is the refractive index of the material of propagation.
When the light travels in the direction shown by the yellow arrow in figure 3.2, it picks up a phase: $E_y(x,z) = E_0 \cdot e^{i\frac{2\pi}{\lambda}n\left(x\sin(\theta)+z\cos(\theta)\right)}$
Since the grating is periodic in x, we have that $E_y(x+\Gamma,z) = E_y(x,z)\cdot e^{i\frac{2\pi}{\lambda}n\Gamma\sin(\theta)}$ in all regions. We can then separate the spatial variables using the Fourier expansion:

$$E_y(x,z) = \sum_{m=-\infty}^{\infty} f_m(z) e^{i\frac{2\pi}{\lambda}(n\sin(\theta)+m\frac{\lambda}{\Gamma})x} = \sum_{m=-\infty}^{\infty} f_m(z) e^{ik_{xm}\cdot x} \tag{3.9}$$

Notice that the Fourier coefficient $f_m(z)$ does not depend on x. The Fourier series is truncated by limiting m to run between $\pm M$, where M is the number of diffraction orders retained in the calculation.
Here we come to the second trade-off. Selecting a high M gives a high accuracy, but increases the computation time. A demonstration for the zeroth order reflection from a 1D silicon line grating is shown in figure 3.3, where the relative errors and calculation times are plotted as a function of the number of orders retained in the calculations.
By inserting equation (3.9) into (3.8) and assuming constant ε. We arrive at the equation:

$$\left[\frac{\partial^2}{\partial z^2} + k_{l,zm}^2\right] f_m(z)^l = 0 \tag{3.10}$$

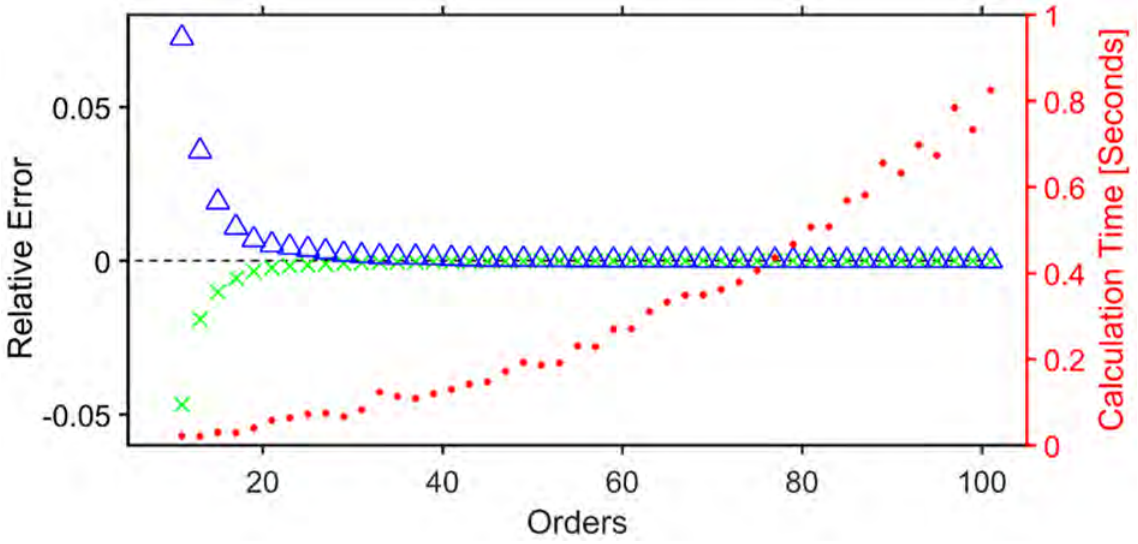

Figure 3.3: Relative error of the TE field (Green Cross), TM field (Blue Triangles) and calculation times (Red Dots) for the zeroth order reflection from a one dimensional silicon grating.

where l is an index defining the region (I, II or III for the Superstrate- , the Grating- and the Substrate region respectively). Since the wavenumber of the reflected field is preserved, we must have:

$$k_l^2 = k_{xm}^2 + k_{l,zm}^2 \tag{3.11}$$

where k_l^2 is the wavenumber of the incoming beam in the l-region. The general solution for equation (3.10) can be written as:

$$f_m(z)^l = A_m e^{-ik_{l,zm}^2} + B_m e^{ik_{l,zm}^2} \tag{3.12}$$

We denote the y-component of electric field E_y^{I}, E_y^{II} and E_y^{III} for the Superstrate-, the Grating- and the Substrate region respectively.
If we assume that the superstrate is lossless, we must have a positive and real refractive index, which enables us to write: $k_{l,zm} = \sqrt{k_l^2 - k_{xm}^2}$. Hence, $k_{l,zm}$ must be purely real for $k_l \geq k_{xm}$ or purely imaginary for $k_l < k_{xm}$. If $k_{l,zm}$ is purely imaginary, we have no propagating waves and only evanescent modes, which are not seen in the far field. On the other hand, if $k_{l,zm}$ is purely real, the first term corresponds to a wave traveling away from the grating. This is the reflected field were A_m is the reflection coefficient of order m (R_m). The second term corresponds to a wave traveling through the grating and to the substrate.
The field in the superstrate region is the incoming field plus the reflected field, thus:

$$E_y^{\mathrm{I}} = e^{ik_{\mathrm{I}}\left(x\sin(\theta)+z\cos(\theta)\right)} + \sum_{m=-M}^{M} e^{ik_{xm}x} \cdot R_m e^{-ik_{\mathrm{I},zm}z} \tag{3.13}$$

The field in the substrate is the transmitted field:

$$E_y^{\mathrm{III}} = \sum_{s=-M}^{M} e^{ik_{xm}x} \cdot T_m e^{ik_{\mathrm{III},zm}z} \tag{3.14}$$

In the grating region, ε is no longer constant, but a function of x. Therefore equation (3.8) changes to:

$$\nabla^2 E_y^{\mathrm{II}} = -\varepsilon(x)\left(\frac{2\pi}{\lambda}\right)^2 E_y^{\mathrm{II}} = -k_0^2 \varepsilon_r(x) E_y^{\mathrm{II}} \tag{3.15}$$

It is therefore necessary to look at the product $\varepsilon_r(x)E_y^{\mathrm{II}}$. The periodicity of $\varepsilon_r(x)$ allows it to be described by the truncated Fourier series:

$$\varepsilon_r(x) = \sum_{h=-M}^{M} a_h e^{ih\frac{2\pi}{\Gamma}x} \tag{3.16}$$

Hence the product we look at is:

$$\varepsilon_r(x)E_y^{\mathrm{II}} = \sum_{h=-M}^{M} a_h e^{ih\frac{2\pi}{\Gamma}x} \sum_{m=-M}^{M} f_m(z) e^{im\frac{2\pi}{\Gamma}x} e^{i\frac{2\pi}{\lambda}nsin(\theta)x} \tag{3.17}$$

Introducing the variable $j = h + m$:

$$\varepsilon_r(x)E_y^{\mathrm{II}} = \sum_{j=-M}^{M} \Big(\sum_{m=-M}^{M} a_{j-s} f_m(z) \Big) e^{2\pi i \left(\frac{j}{\Gamma} + \frac{n}{\lambda} sin(\theta)\right) x} \tag{3.18}$$

Now when the field has been defined for the three different regions, the reflection, R_m, and the transmission, T_m, can be found by requiring that:

$$\begin{aligned} E_y^{\mathrm{II}}(z=0) &= E_y^{\mathrm{I}}(z=0) \\ E_y^{\mathrm{II}}(z=h) &= E_y^{\mathrm{III}}(z=h) \end{aligned} \tag{3.19}$$

Which must hold for all values of m. No interesting physics is involved in solving these equations, so this is omitted in this thesis. After solving (3.19), one ends up with the reflection and transmission coefficients for all the orders retained in the calculation. These can be stored in databases to be accessed later for a scatterometry analysis or be calculated on the fly for a direct optimization.

In the following paper, it is shown how RCWA can be used to model imperfections in the grating. This is done by creating a so-called super cell where the defects are assumed to be periodic on a scale much larger than the wavelength of the light impinging on the sample. One of the defect types was previously reported in [33]. The paper demonstrates a semi-analytical approach for introducing defects on a perfect grating using only a single RCWA calculation. By using this semi-analytical model calculation times are vastly improved by reducing the number of free parameters and therefore the number of parameter permutations. Furthermore, we show how the simulations can be used to generate a neural network. This network can be used in place of a library. The network is found to be more robust to noise and has static computation times compared to the library search, which has a computation time scaling with the number of data entries. Given enough scatterometric data, a network as the demonstrated could use measured data instead of simulated signals.

Preprint of paper 4

Title:

Replacing Libraries in Scatterometry

Journal:

Optics Express, vol. 26 (2018)

Authors:

J. S. Madsen, S. A. Jensen, J. Nygård and P. E. Hansen

DOI of published paper:

10.1364/OE.26.034622

Replacing Libraries in Scatterometry

Abstract

Diffraction gratings have a wide array of applications in optics, diagnostics, food science, sensing and process inspection. Scattering effects from defects can severely degrade the performance of such gratings. In this paper, we consider three classes of defects: Two classes introduced at the grating/air interface, as a change in line heights, and one class introduced as a sinusoidal variation of the grating/substrate interface. The scattering properties of the gratings are modelled using rigorous coupled wave analysis, and defects are approximated with a new semi-analytical model and a neural network. The new methods make it possible to avoid the time consuming library generation/search strategy commonly used in scatterometry. The method does not introduce new numerical parameters, and therefore no new parameter correlations. This work enables improved grating reconstruction, especially of non-diffracting short pitch gratings. It is found that two of the defect classes can be adequately described by the semi-analytical model, while the third defect is accurately reconstructed by a neural network. The network is demonstrated to be faster than a library search and more versatile for related structures.

1. Introduction

Periodic nanostructures can be used to enhance or add desired functions [1,2]. In fabrication of these nanostructures, product defects of a few nanometers are hard to avoid. As the sizes of the produced nanostructures shrink, the relative sizes of these defects increase. For NIL on hard surfaces linewidth and height defects of tens of nanometers have been reported [3].
Furthermore, defects are likely to be even more prominent when fabrication moves out of the laboratory and into the mass-production industry [4]. These defects can affect the functionality of the nanostructures, for example in their interaction with light [5].

Scatterometry is an optical technique already utilized in the semiconductor industry, where a diffraction grating is reconstructed from an optical signal by inverse modelling[6]. Rigorous coupled wave analysis (RCWA)[7] is the common workhorse for scatterometry modelling due to its speed, convergence and relatively simple implementation. In RCWA, the diffraction grating is approximated by rectangular slabs, and Maxwell's equations are solved by coupling the boundary conditions between the slabs [8].

Conventionally, angular resolved scatterometry has been deployed in the semiconductor industry [9]. Moving to wavelength-resolved scatterometry, one can reduce the complexity of the measurement hardware by removing the need for goniometric detector setups, since all information

can be collected at a single point. Furthermore, as the period of the functional nanostructures decreases, the number of observable (non-evanescent) diffraction orders decreases as well. When all the optical information is extracted from the zeroth order (specular reflection), the reconstruction of complex structures such as multiple trapezes, additional material layers and rounded corners, tend to become ambiguous due to correlations between the added parameters. In the worst cases, one could end up reconstructing a structure different from the physical sample without knowing it. It is therefore relevant to investigate how the zeroth diffraction order from a complex structure can be approximated by simpler models without the dreaded ambiguity.

In this paper, RCWA is used for forward calculation of the diffraction orders from a grating. However, when describing complex structures such as roughness and defects, a large amount of parameters is needed to describe the grating. Since the RCWA solver is called once for each permutation of parameters, this ends up being very time-consuming [10]. Furthermore, one could end up with a strong correlation between the parameters, making the reconstruction unstable [11]. Based on this, it is desirable to retain a low number of parameters in the modelling without losing too much information.

In the presented work we, show how scatterometric data can be used to detect different classes of defects. We simulate the multi-spectral zeroth order diffraction from three classes of defects, described in the next section, with varying magnitudes of the introduced defect. This is done by describing the grating by a unit cell containing multiple grating lines, called a supercell. We then investigate how these defects can be characterized without using a conventional library search. We present a semi-analytical method based on the total integrated scatter model [12] to incorporate the effect of scattering from defects into the scatterometric reconstruction. This method requires only a single numerical calculation describing the perfect grating. The total integrated scatter model is combined with the simplest structure form of RCWA, a rectangular grating described by a period, height and width, to make a semi-analytical model. We show that this model accurately predicts the scatterometric signature of the defects on the sample. The model can be used to reduce the dimensionality of the scatterometry library, and thus simplify the analysis process. It is stressed that the semi-analytical model suggested could just as well be used for an angle resolved spectrum.

Furthermore, we shown how a neural network can be developed and used to analyze defects in place of a library search strategy. Neural networks have previously been deployed to select a library for scatterometry [13,14] or replace the library[15,16]. These works aimed to characterize gratings created from simple unit cells, where all grating lines are assumed identical. We demonstrate that we can use the neural network to characterize defects from the most complex supercell and achieve good performances on similar defects.

2. Simulations

The diffraction efficiency, η, is defined as the zeroth diffracted order with respect to the incoming light [8]. Numerically calculated diffraction efficiencies, η_{Num}, for the structures with different defects are found using RCWA. All structures modelled in the examples shown here are constructed by imposing the defects on perfect line gratings in silicon. The perfect line gratings are described by their period, Δ, height, h, their width, w. The simulated gratings have the following parameters: Δ = 2 μm, h = 0.7 μm and w = 1 μm. In addition, periodic defects are added to theses gratings by describing the grating as a super cell consisting of ten unit cells of the perfect grating, this super cell then has a period of Γ = 20 μm.

Three classes of defects are examined by incorporating them into the structure of the supercell:

1) A simple defect where the first of the ten grating lines are higher than the others, see Fig. 1(a).
This was observed in our previous work with injection molded nanostructures, where some grating lines had additional material on top [17].
2) A sinusoidal defect in the height over the grating, see Fig. 1(b). This defect can occur in bottom-up fabrication [18].
3) A perfect grating on a sinus shaped substrate, see Fig. 1(c). This defects could arise from a grinding step in the substrate preparation, or could be purposely introduced as in ref. [19].
The magnitude of the defects is described by the parameter d shown in Fig. 1. Simulations are performed using incoming light polarized along the grating lines (TE), with an incident angle θ_I of 70 degrees with respect to the grating normal, and a wavelength, λ, ranging from 250 nm to 850 nm. In order for the numerical supercell calculations to converge, a large number of diffraction orders, defining the truncation of the Fourier series in the RCWA calculations [19], needs to be retained in the calculations, which in turn makes the calculations very time-consuming. In the presented work, over 400 orders are reatined in the RCWA calculations.

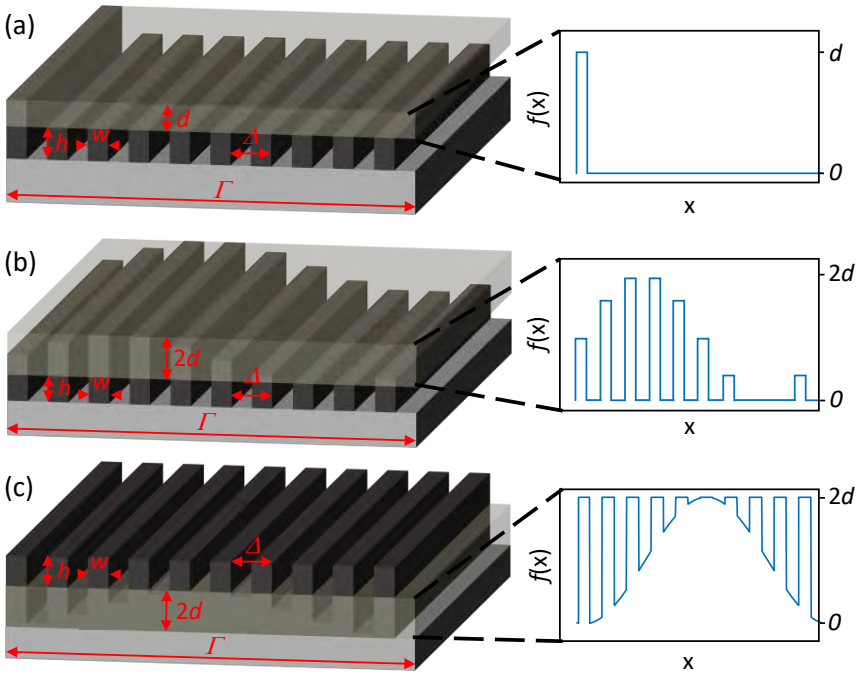

Fig. 1. Sketches of the different grating imperfections examined. The denoted parameters are the height of the perfect grating, *h*, the width of the grating, *w*, and the size of the imperfection, *d*, the period of the simple grating, Δ, and the period of the supercell, Γ. The marked volume shows where the defect is introduced and the plot to the left shows the profile of the defect used in the semi-analytical model. (a) Simple grating defect. (b) Sinusoidal grating defect. (c) A perfect grating on a sinusoidal substrate. All imperfections have been exaggerated for clarity.

3. Semi-analytical model

The Total Integrated Scatter (TIS) originates from scalar diffraction theory [20]. The model describes what fraction of the reflected light is scattered from a rough surface. It is conventionally described as [12]:

$$TIS = \frac{R_T - R_S}{R_T} = 1 - \exp\left(-\left(4\pi \frac{\sigma \cdot \cos(\theta_I)}{\lambda}\right)^2\right) \qquad (1)$$

Here, R_T, is the total reflectance, R_S, is specular reflected light, σ is the Root Mean Square roughness of the surface, also commonly known as R_q [21].

The roughness, σ, used in the TIS calculation is found as:

$$\sigma = \sqrt{\frac{1}{\Gamma}\int_0^{\Gamma} f(x)^2 \, dx} \qquad (2)$$

Where the height function *f(x)* describes the part of the grating with the introduced defect (see profile in Fig. 1). The magnitude of the defect *d* can be moved out of the integral, making it possible to solve

the integral and scale with *d*, for an analytical mapping between *σ* and *d*. It is important to note that in the general case, *σ* should be the appropriately bandwidth limited surface roughness, since spatial frequencies larger than $\frac{1}{\lambda}$ produce evanescent waves and are irrelevant with regards to scattering [12]. In this paper, the variations have a low frequency, and eq. (2) can safely be used.

Our semi-analytical model assumes that the introduced defect can be treated as a perturbation to the perfect grating described by the TIS model, and that the scattering caused by the defect and the perfect grating are uncoupled so that the defect can be treated as a perturbation. The diffraction efficiency found from the semi-analytical model, η_{SA}, is given by:

$$\eta_{SA} = \frac{I_S}{I_I} = \eta_{Grat} \cdot (1 - TIS) \qquad (3)$$

Where η_{Grat} is the diffraction efficiency from the rectangular grating with no defects, I_S and I_I are the intensities of the scattered and incoming light respectively. This enables us to use a single numerical calculation for the simple rectangular grating when characterizing a grating with defects. It should be noted that other computational methods than RCWA, such as finite difference time domain [22] or finite element method [23], can be used to find η_{Grat} as well.

4. Results

In order to compare the agreement between the diffraction efficiency, η_{Num}, calculated using RCWA on the supercell, and the diffraction efficiency η_{SA} from the semi-analytical model, we look at the difference between the samples with introduced defects and perfect samples.

In Fig. 2 we show:

$\delta\eta_{Num} = \eta_{Num} - \eta_{Grat}$ (solid line) and $\delta\eta_{SA} = \eta_{SA} - \eta_{Grat}$ (crosses)

as a function of the wavelength for the three defect classes at different magnitudes. We see that the semi-analytical model works well for the first class and exceptionally well for the second class.

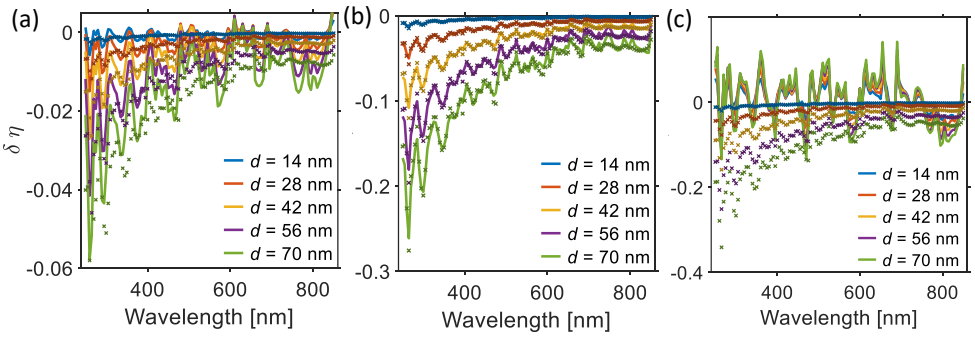

Fig. 2. Defect class 1 (top), class 2 (middle) and class 3 (bottom). Fully drawn lines show the $\delta\eta_{Num}$ while the slightly darker crosses show $\delta\eta_{SA}$. *d* is illustrated in Fig. 1. Note the different y-axes.

However, the third class is not described well by the semi-analytical model. Intuitively, this breakdown of the model can be understood by looking at how the defect is introduced on the structure: For the first two classes, the defect is placed on top, but for the third, the defect is embedded into the perfect structure. The poor result in Fig. 2(c) suggests that the signals from the two areas cannot be decoupled, and therefore cannot be approximated by the semi-analytical model. This suggests that the defects above the grating, and defects inside the grating must be treated differently.

4.1 Defect above grating

Going back to the first two classes, we see that we have a good agreement between the RCWA and the semi-analytical model, which becomes gradually worse as the magnitude of the defect increases. This would suggest that the Semi-analytical model is valid for "moderately" rough surfaces. This is a property inherited from the TIS model. It is noted that type 1 has a lesser impact on the optical signal (notice the different y-axis), which is to be expected since the defect class 1 has a lower change in the volume of the material.

Since the total integrated scatter based model describes the second type of grating well, it can be used to find the defect magnitude *d* from an intensity signal using a library search approach traditional employed in scatterometry. To demonstrate this, the correct signal is taken to be the RCWA signal with- and without applied white Gaussian noise with a standard deviation of 0.5%, and the semi-analytical model is fitted by minimizing the mean square error, *MSE,* described below using nearly continuous values for the magnitude of the defect, *d*. These continuous values of *d* are denoted δ.

$$MSE(\delta, d) = \frac{1}{N}\sum_{i=1}^{N}\left(\eta_{SA}(\lambda_i, \delta) - \eta_{Num}(\lambda_i, d)\right)^2 \qquad (4)$$

Where *N* (121 in this case) is the number of wavelengths used, and $\eta_{Num}(\lambda, d)$ is the numerical diffraction efficiency with *d* locked at several values from 2% to 10% of the total grating height. $MSE(\delta, d)$ can be seen for the different defect *d* values in Fig. 3 We see that the best fitting solution finds the defect size from the RCWA simulations with- or without added noise. This demonstrates that for this case, the simple semi-analytical model can be used to describe the defect. Furthermore, for the noiseless RCWA, we see that the *MSE* "dip" becomes wider as the defect magnitude increases, and therefore the best solution becomes less well defined. This result shows that the semi-analytical model works best for small defect values, a property inherited from the TIS model. In the presence of noise, we see that the best fitting solution becomes worse due to the MSE reaching the

noise floor. This shows, that the signal-to-noise ratio acts as a lower boundary condition for the model. If one wants to look at very small perturbations to the perfect grating, one needs a good signal to noise ratio.

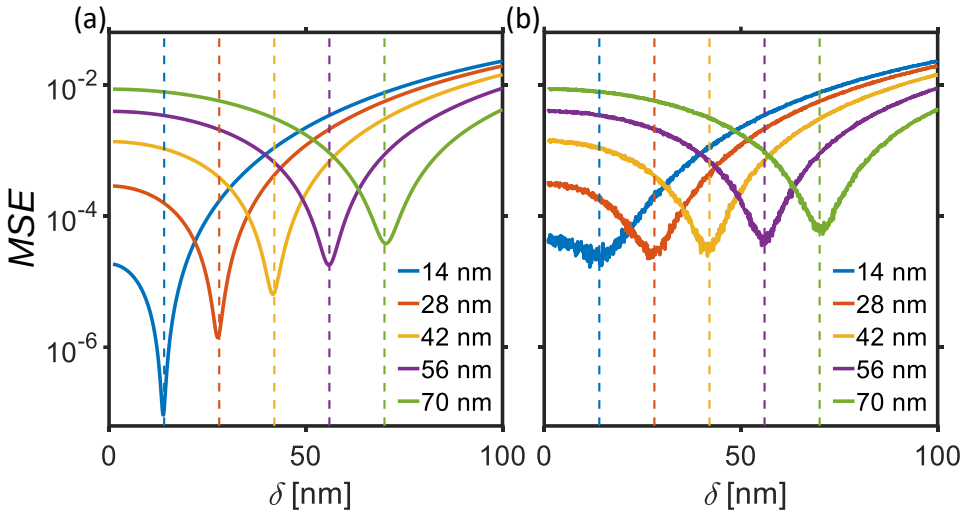

Fig. 3. Mean square error as a function of defect size used in the semi-analytical model for defect class 2 using pure RCWA (a) and RCWA with added white Gaussian noise (b). The legends and the dashed lines indicate the defect size *d* used in the RCWA calculations, while the fully drawn lines indicate the defect sizes used in the semi-analytical model.

Since the semi-analytical model is based on the simplest form of RCWA (a rectangle described by a single slab), it could also be used in combination with conventional library search scatterometry aimed at determining the parameters of the perfect grating. Here one could use the model to add a defect or roughness parameter to a pre-generated database without having to re-calculate a library with a higher dimensionality. In the simplest case one would only need to simulate a single structure numerically and account for other variations analytically, which is computationally much more efficient.

It would also be possible to completely avoid a library search by first assuming that the measured signal is described by η_{SA}. Then the ratio $\frac{\eta_{SA}}{\eta_{Grat}}$ could be used to analytically calculate σ from eq. (3) and (1). Since there is a linear mapping from σ to d for each class, this could be used to analytically characterize the defect magnitude.

Before the time of computers, where exponential functions should be avoided, eq. (1) was approximated by a firs order Taylor expansion:

$$TIS = \frac{R_T - R_S}{R_T} = 1 - \exp\left(-\left(4\pi\frac{\sigma\cdot\cos(\theta_I)}{\lambda}\right)^2\right) \approx \left(4\pi\frac{\sigma\cdot\cos(\theta_I)}{\lambda}\right)^2 \qquad (5)$$

The approximated TIS expression is assumed to be valid for optically smooth surfaces, commonly described by the g-factor[24]:

$$g = 4\pi \frac{\sigma \cdot \cos(\theta_i)}{\lambda} << 1 \qquad (6)$$

If g is small enough, higher order terms from the Taylor series can be safely discarded. This is thoroughly discussed in refs. [25–27].

Since the approximation of the TIS model is still seeing industrial use [9], it is interesting to investigate how well the semi-analytical model fares using the first order Taylor approximation for the total integrated scatter model.

Fig. 4 shows the *MSE* minimization using the approximation of eq. (5) in the semi-analytical model. In this case we see that the semi-analytical model finds smaller defects than the numerical approach. This "deficit" seems to increase with the magnitude of the defect, corresponding to the approximation becoming worse as g gets larger. The limit where the approximation stops working could be interpreted as the point where the optically smooth criterion is no longer valid. For class 2 with d = 30 nm, we obtain a roughness parameter g of 0.365 and 0.107 for the lowest and highest wavelengths respectively. Again, we see the trend that the RCWA with noise finds the same solution as the noiseless RCWA.

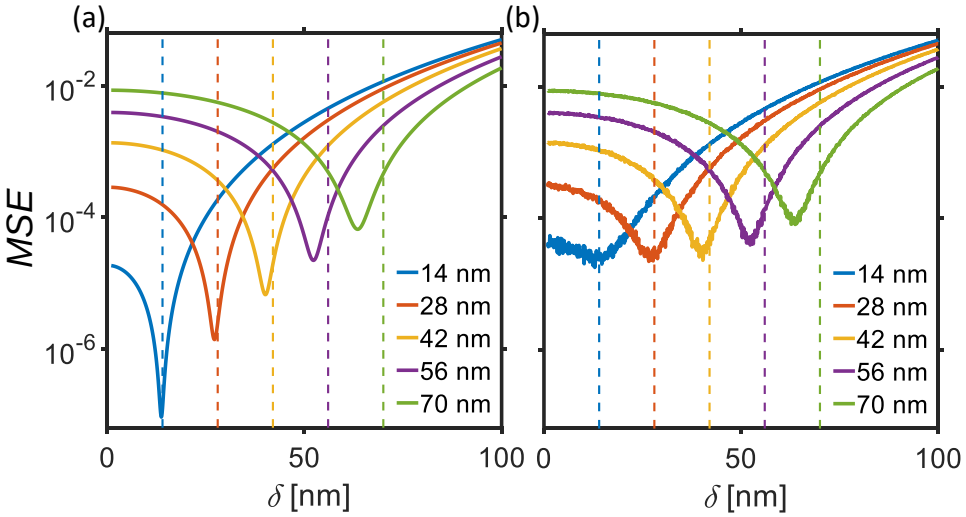

Fig. 4. Same approach as Fig. 3 but using the simplified (first order Taylor) TIS model for defect class 2. The legends and the dashed lines indicate the defect size d used in the RCWA calculations, while the fully drawn lines indicate the defect sizes used in the semi-analytical model. We see that this model already falls off for defect values above 28 nm (corresponding to 4% of the grating height).

Previous work on injection molded nanostructures [17,28] has shown that one often ends up with very little characteristic features in the wavelength resolved spectrum. In those cases, it is necessary

to restrict the reconstruction to a few model parameters. The presented method can be used as a perturbation for the simpler structures and gives an idea of whether or not these defects are within a safe limit or if they might be detrimental to the desired functionality. The easy implementation would make the method much more attractive to use with existing libraries rather than recalculating a new library with a higher dimension to account for the defects.

4.2 Defect in the grating area

As we saw in the previous section, class three defects could not be well described by the semi-analytical model. The simulations do, however, clearly show that we can easily distinguish a grating on a periodic grinded (sinusoidal) surface from a grating on a plain surface, since the signal change is much larger than typical measurement uncertainties associated with scatterometry [8]. This result was also experimentally reported in ref [19]. Furthermore, it is observed that the signal changes very little with the magnitude of the defect. Looking at the solid line data in Fig. 2 (c), it is clear that any model describing the effect of the third defect class would be complex. Therefore, it is decided to attempt a solution using machine learning.

A neural network has been developed using RCWA simulated data sets, as a placeholder for experimental data, with *d* varying from 1 to 100 nm in steps of 1 nm. Physical measurements have been simulated by adding white Gaussian noise [29] to the simulated spectra. A thousand sets of noisy data are made from each simulation, resulting in 100.000 datasets used for the network.

The network type is a multilayer perceptron[30]. Here the input data points are passed through an input layer with a node for each wavelength, 121 in total, a hidden layer with 10 nodes, and then converted to output data at the end by an output layer with a single node finding the defect magnitude *d*. All neurons from the hidden layer are interconnected to all nodes in input layer and the output layer through weighted transfer functions. The network is sketched in Fig. 5. When training the network, the weights of the transfer functions are adjusted in order to map a desired output from the input by minimizing a mean squared error function. The network described here is trained using a Levenberg-Marquardt algorithm [31–33]. The input layer uses a tan-sigmoid transfer function (Tansig), and the output layer uses a linear transfer function (Purelin) [34,35].

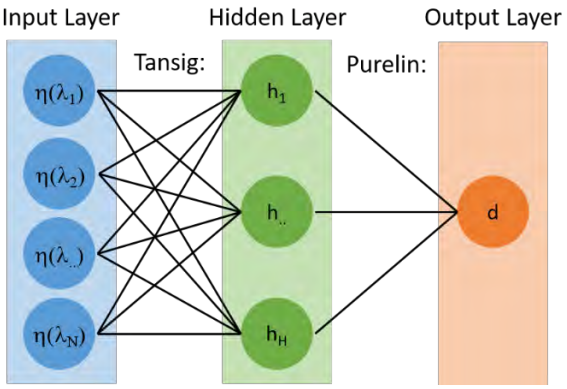

Fig. 5. Sketch of the neural network. The input layer has a node for each wavelength simulated (121). The hidden layer has a total of 10 nodes, and the output layer has a single node finding the defect magnitude *d*. The nodes from the input layer are connected to the hidden layer through a weighted Tansig transfer function. In the same manner, all nodes in the hidden layer are connected to the output node through a Purelin transfer function.

Once the network is trained, it can be used to predict outputs from new unseen data. In order to evaluate the networks ability to determine defects from a scatterometry measurement, a new set of measurement signals are simulated. These signals are then passed through the network, and the estimated defect is extracted. The targeted defect value, d_T, is the value of *d* used in the RCWA code to generate the true signal, and the found defect value, d_F, is the value of *d* predicted by the network. The results can be seen in Fig. 6. We see that we have an overall good agreement with a seemingly randomly distributed deviation from the targeted value. This is expected, since the signal changes very little with a change in the defect magnitude, as seen in Fig. 2(c). The found magnitudes are fitted as a linear function of the targeted magnitudes, and the correlation:

$$d_F = 0.9959 \cdot d_T \qquad (7)$$

is found.

Since we have a good fit and no major outliers, it is concluded that this neural network can be used to reliably characterize class three defects. Since the prediction does not repeat calculation steps, it can be done very fast. The prediction time does not scale with the size of the data used to generate the network as opposed to a standard library approach, where the search time is directly proportional to the library size. This would make a neural network approach even more suited for inline characterization, if computation time starts to present a bottle-neck. For a quick comparison, the neural network finds the defect magnitude in 0.46 ms, while a library approach as used in ref. [36] uses roughly 0.01 ms for each generated RCWA structure (typically tens of thousands, but could easily be larger for complex structures). Both calculations were performed on a standard laptop.

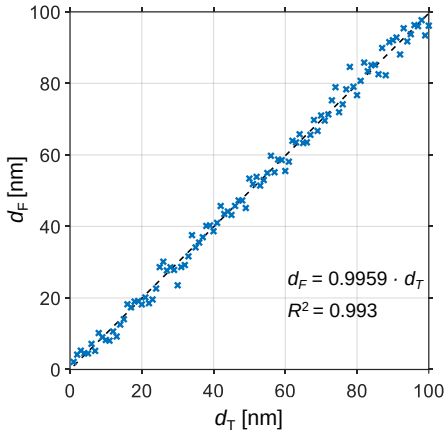

Fig. 6. Performance of the Neural network. The defect found by the neural network, d_F, is plotted vs the targeted defect, d_T, from the simulated models with added noise. The black dashed line shows the best linear fit to the data.

Defects, by definition, are not perfect. It is therefore interesting to see how the same network performs on similar, but different substrate structures. To test the developed network, we look at how well it predicts the defect magnitude from a substrate described by a bottom cut sinusoidal. Data was simulated for cuts of 12.5 %, 25 %, 37.5 % and 50 % of the total height as sketched in the upper insert of Fig. 7. This was done without any retraining of the network.

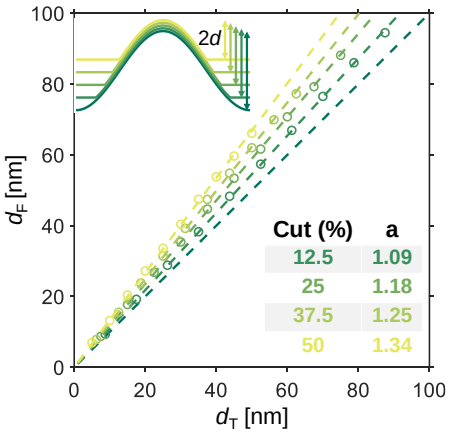

Fig. 7. Evaluation of the developed network using different substrate defects. Circles shows the magnitude found by the network, and the dashed lines show the best linear fit. The diagonal line shows the fit obtained from the uncut sinusoidal in Fig. 6 to guide the eye. Upper insert shows the simulated structures from uncut to 50% cut. The curves have been displaced for clarity. The grating lines on top of the substrate has been omitted in the illustration. The Arrows mark 2*d* for the different cut values, where d is the target value for the given structure. Lower insert: table showing the linear coefficient for the fit: $d_F = a \cdot d_T$.

The performance of the network can be seen in Fig. 7. The parameters for the best fitting line can be seen in the inserted table. The network clearly recognizes features from the perfect sine

substrates, seen by the linearity between d_T and d_F. Good linear fits are seen for all cut values. As a trend, the neural network over-predicts the amplitude, by a larger ratio for the larger cut values. This is likely caused by the network only being trained on perfect sine structures. This means that the network will match the signal to the best fitting perfect structure, which by nature has a larger d value than the corresponding cut structure. This suggests that even if we do not have a perfect sinusoidal structure, we can still estimate a substrate defect and compare the relative substrate roughness between two samples. It has thus been demonstrated that the neural network can be used to predict a defect size for similar, but not identical, substrates. This method is believed to be more stable, than a library of RCWA signals simulated from perfect sinusoidal.

Future work will emphasize using the semi-analytical model in combination with inline characterization and further development of the neural network by adding new defect types. Here defects as line edge roughness will be of certain interest.

5. Conclusion

We have examined three different classes of defects introduced on perfect rectangular silicon gratings. The defects were introduced above the grating area and in the grating area for the two first classes and the last class respectively. A semi-analytical model has been suggested to determine the magnitude of the grating defect. For the first two classes, the defect is in agreement with a semi-analytical model based on TIS and RCWA. The third class cannot be described by the semi analytical model. This model enables defect characterization of low period non-diffracting structures. A neural network has been developed to characterize these defects. The network can accurately determine the magnitude of the defect. Both methods can be used to create simple models describing the defects without the need of additional RCWA computations, and in some cases make it possible to entirely omit a library generation and search. Future work will emphasize using the semi-analytical model in combination with inline characterization and further development of the neural network by adding new defect types. Here defects such as line edge roughness will be considered.

Funding

The work presented has received funding from The Danish Agency for Institutions and Educational Grants, the Quantum Innovation Center, the Eurostars project E11002-OptoRough.

References

[1] C. Pan, Z. Liu, Y. Pang, X. Zheng, H. Cai, Y. Zhang, Z. Huang, Design of a high-performance in-coupling grating using differential evolution algorithm for waveguide display, Optics Express. 26 (2018) 26646–26662. doi:10.1364/OE.26.026646.

[2] W. Lee, S.-J. Park, Porous Anodic Aluminum Oxide: Anodization and Templated Synthesis of Functional Nanostructures, Chemical Reviews. 114 (2014) 7487–7556. doi:10.1021/cr500002z.

[3] 13th International Conference on Metrology and Properties of Engineering Surfaces 2011: Twickenham, United Kingdom, 12 - 15 April 2011, Curran, Red Hook, NY, 2011.

[4] M.G.S. Bernd, S.R. Bragança, N. Heck, L.C.P. da S. Filho, Synthesis of carbon nanostructures by the pyrolysis of wood sawdust in a tubular reactor, Journal of Materials Research and Technology. 6 (2017) 171–177. doi:10.1016/j.jmrt.2016.11.003.

[5] V.K. Tewary, ed., Modeling, characterization, and production of nanomaterials, Elsevier, Amsterdam, 2015.

[6] C. Raymond, Overview Of Scatterometry Applications In High Volume Silicon Manufacturing, in: AIP, 2005: pp. 394–402. doi:10.1063/1.2062993.

[7] M.G. Moharam, T.K. Gaylord, Rigorous coupled-wave analysis of planar-grating diffraction, Journal of the Optical Society of America. 71 (1981) 811–818. doi:10.1364/JOSA.71.000811.

[8] M.H. Madsen, P.-E. Hansen, Scatterometry—fast and robust measurements of nano-textured surfaces, Surface Topography: Metrology and Properties. 4 (2016) 023003–023028. doi:10.1088/2051-672X/4/2/023003.

[9] J.C. Stover, Optical scattering: measurement and analysis., Spie Press, Place of publication not identified, 2016.

[10] S. Schröder, A. Duparré, L. Coriand, A. Tünnermann, D.H. Penalver, J.E. Harvey, Modeling of light scattering in different regimes of surface roughness, Optics Express. 19 (2011) 9820–9835. doi:10.1364/OE.19.009820.

[11] S. Rizvi, ed., Handbook of photomask manufacturing technology, Taylor & Francis, Boca Raton [Fla.], 2005.

[12] J.E. Harvey, Total integrated scatter from surfaces with arbitrary roughness, correlation widths, and incident angles, Optical Engineering. 51 (2012) 013402–013413. doi:10.1117/1.OE.51.1.013402.

[13] I. Gereige, S. Robert, S. Thiria, F. Badran, G. Granet, J.J. Rousseau, Recognition of diffraction-grating profile using a neural network classifier in optical scatterometry, Journal of the Optical Society of America A. 25 (2008) 1661–1667. doi:10.1364/JOSAA.25.001661.

[14] I. Kallioniemi, J. Saarinen, E. Oja, Characterization of diffraction gratings in a rigorous domain with optical scatterometry: hierarchical neural-network model, Applied Optics. 38 (1999) 5920–5930. doi:10.1364/AO.38.005920.

[15] S. Wei, L. Li, Measurement of photoresist grating profiles based on multiwavelength scatterometry and artificial neural network, Applied Optics. 47 (2008) 2524–2532. doi:10.1364/AO.47.002524.

[16] S. Robert, A. Mure-Ravaud, D. Lacour, Characterization of optical diffraction gratings by use of a neural method, Journal of the Optical Society of America A. 19 (2002) 24–32. doi:10.1364/JOSAA.19.000024.

[17] J.S. Madsen, L.H. Thamdrup, I. Czolkos, P.-E. Hansen, A. Johansson, J. Garnaes, J. Nygard, M.H. Madsen, In-line Characterization of Nanostructured Mass-produced Polymer Components Using Scatterometry, Journal of Micromechanics and Microengineering. 27 (2017) 085004–085010. doi:10.1088/1361-6439/aa7a3a.

[18] B.D. Gates, Q. Xu, M. Stewart, D. Ryan, C.G. Willson, G.M. Whitesides, New Approaches to Nanofabrication: Molding, Printing, and Other Techniques, Chemical Reviews. 105 (2005) 1171–1196. doi:10.1021/cr030076o.

[19] P.-E. Hansen, M.H. Madsen, J. Lehtolahti, L. Nielsen, Traceable Mueller polarimetry and scatterometry for shape reconstruction of grating structures, Applied Surface Science. 421 (2017) 471–479. doi:10.1016/j.apsusc.2017.02.091.

[20] P. Beckmann, The scattering of electromagnetic waves from rough surfaces, Macmillan Company, New York, 1963.

[21] D.J. Whitehouse, Surfaces and their measurement, Kogan Page Science, London, 2004.

[22] Kane Yee, Numerical solution of initial boundary value problems involving maxwell's equations in isotropic media, IEEE Transactions on Antennas and Propagation. 14 (1966) 302–307. doi:10.1109/TAP.1966.1138693.

[23] T. Delort, D. Maystre, Finite-element method for gratings, Journal of the Optical Society of America A. 10 (1993) 2592–2601. doi:10.1364/JOSAA.10.002592.

[24] J.E. Harvey, N. Choi, A. Krywonos, Scattering from moderately rough interfaces between two arbitrary media, in: S.A. Straka, N. Carosso (Eds.), San Diego, California, United States, 2010: pp. 77940–77950. doi:10.1117/12.863995.

[25] H. Davies, The reflection of electromagnetic waves from a rough surface, Proceedings of the IEE - Part IV: Institution Monographs. 101 (1954) 209–214. doi:10.1049/pi-4.1954.0025.

[26] H.E. Bennett, J.O. Porteus, Relation Between Surface Roughness and Specular Reflectance at Normal Incidence, Journal of the Optical Society of America. 51 (1961) 123–138. doi:10.1364/JOSA.51.000123.

[27] J.C. Stover, S.A. Serati, C.H. Gillespie, Calculation Of Surface Statistics From Light Scatter, Optical Engineering. 23 (1984). doi:10.1117/12.7973309.

[28] J.S. Madsen, S.A. Jensen, L. Nakotte, A. Vogelsang, L.H. Thamdrup, I. Czolkos, A. Johansson, J. Garnæs, T. Nielsen, J. Nygård, P.E. Hansen, Scatterometry for optimization of injection molded nanostructures at the fabrication line, The International Journal of Advanced Manufacturing Technology. 99 (2018) 2669–2676. doi:10.1007/s00170-018-2665-7.

[29] V. Mathuranathan, Digital modulations using Matlab: build simulation models from scratch, 2017.

[30] M.. Gardner, S.. Dorling, Artificial neural networks (the multilayer perceptron)—a review of applications in the atmospheric sciences, Atmospheric Environment. 32 (1998) 2627–2636. doi:10.1016/S1352-2310(97)00447-0.

[31] K. Levenberg, A method for the solution of certain non-linear problems in least squares, Quarterly of Applied Mathematics. 2 (1944) 164–168. doi:10.1090/qam/10666.

[32] D.W. Marquardt, An Algorithm for Least-Squares Estimation of Nonlinear Parameters, Journal of the Society for Industrial and Applied Mathematics. 11 (1963) 431–441. doi:10.1137/0111030.

[33] B.G. Kermani, S.S. Schiffman, H.T. Nagle, Performance of the Levenberg–Marquardt neural network training method in electronic nose applications, Sensors and Actuators B: Chemical. 110 (2005) 13–22. doi:10.1016/j.snb.2005.01.008.

[34] D. Ramakrishnan, T.N. Singh, N. Purwar, K.S. Barde, A. Gulati, S. Gupta, Artificial neural network and liquefaction susceptibility assessment: a case study using the 2001 Bhuj earthquake data, Gujarat, India, Computational Geosciences. 12 (2008) 491–501. doi:10.1007/s10596-008-9088-8.

[35] R. Hmamouchi, M. Larif, S. Chtita, A. Adad, M. Bouachrine, T. Lakhlifi, Predictive modelling of the LD_{50} activities of coumarin derivatives using neural statistical approaches: Electronic descriptor-based DFT, Journal of Taibah University for Science. 10 (2016) 451–461. doi:10.1016/j.jtusci.2015.06.013.

[36] J.S. Madsen, P.E. Hansen, P. Boher, D. Dwarakanath, J.F. Jørgensen, B. Bilenberg, J. Nygård, M.H. Madsen, Study on Microgratings Using Imaging, Spectroscopic, and Fourier Lens Scatterometry, Journal of Micro and Nano-Manufacturing. 5 (2017) 031005–031011. doi:10.1115/1.4036889.

Chapter 4

Imaging Scatterometry

In the world of metrology, a vast amount of characterization methods already exist. Scatterometry will only be accepted if the results are in agreement with other well-established measurement techniques. This chapter explains the concept of imaging scatterometry. Paper 1, reproduced at the end of the chapter, compares imaging and spectral scatterometry with AFM and confocal microscopy. This was done by measuring 1D line gratings in silicon with different heights. In addition, results from a Fourier Lens scatterometer [34, 35] developed during the InFoScat project are reported. We found a good agreement between conventional and imaging scatterometry, with a small offset with respect to the AFM. It should be noted that the height estimated by the confocal microscope has a larger uncertainty than the other two techniques. Large offsets were found by the confocal microscope when measuring the samples with a nominal height of 300 nm. For this sample, it was found that the confocal microscope overestimated the height when using a 150x objective, while a 50x objective underestimated the height. In the end, it is concluded that both the imaging and the spectroscopic scatterometer are able to reliably measure the heights of the sample based on their agreement with the metrology AFM at DFM.

4.1 Concept

The imaging scatterometry technique developed at DFM offers the unique opportunity to characterize multiple nanostructures with a single measurement [14]. This is done by segmenting the intensity measurements into the pixels of a camera. In practice, this is done by taking multiple pictures of the sample illuminated at different wavelengths and stacking them together in the analysis. The process is sketched in figure 4.1. This technique is very user-friendly compared to other scatterometry techniques since the operator can easily detect misalignments or displacement of the sample and correct for those in the inverse modeling. Furthermore, macroscopic defects can be found, and the homogeneity of an area can be evaluated. In the case of an automated measurement where there is no operator to select an area of interest, the images can still be saved, and be used later when determining if a part failing the initial test should be scrapped or not. Alternatively, advanced imaging recognition techniques can be utilized in automation both with respect to

alignment and area of interest. In the paper presented at the end of this chapter, a

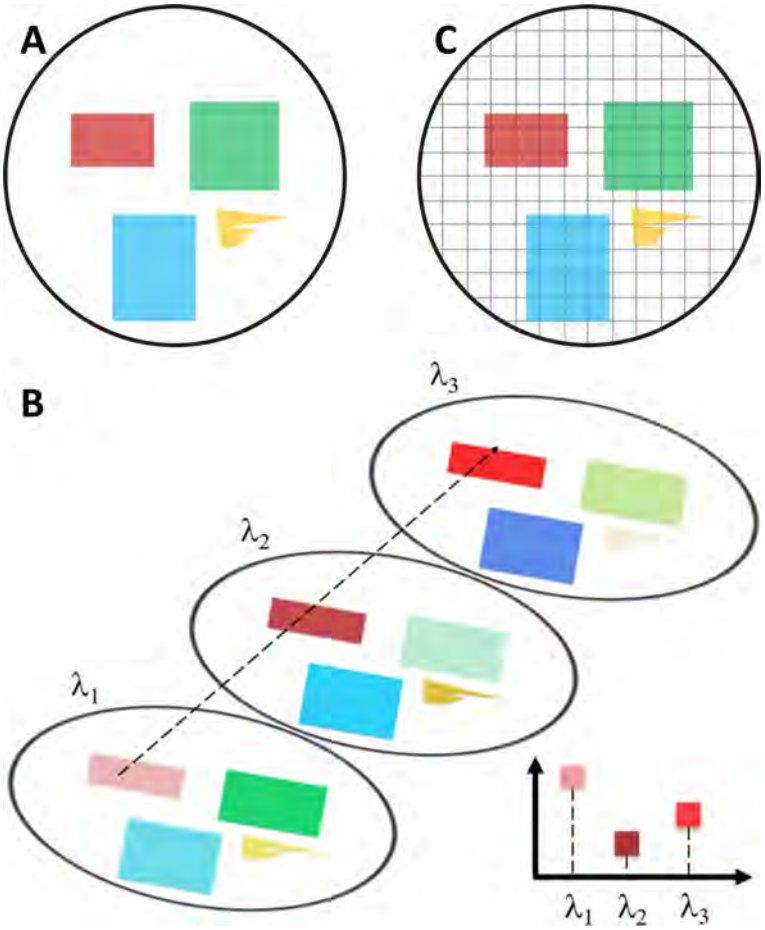

Figure 4.1: Sketch of the idea behind imaging scatterometry. (A) Image of a sample with multiple different structures within the beam spot. (B) The sample is illuminated by light with different wavelengths. (C) Same image as in (A), but now segmented into pixels. The user can detect macroscopic defects by eye and decide where to perform the analysis in the post-processing based on this image.

CCD camera (Pixelink, PL-B957) has been used. However, recently a new camera (The imaging source, DMK 23UX174) has been acquired and is used for the work on injection molded nanostructures in Chapter 6 and nanowires in Chapter 9. The advantages of this camera are a higher span of exposure times and a factor of two in the total amount of pixels, as well as the possibility of collecting 12-bit data for a higher dynamic range. To acquire images of different wavelengths, a tune-able Lyot filter is used (Perkin Elmer, Varispec VIS-07-20). The filter defines the spectral range of the system (450nm to 690 nm). This filter is further discussed in Chapter 5. The imaging scatterometer uses a variable exposure time for each acquired image to utilize the full dynamic range of the system. A flowchart showing how the measurements are performed can be seen in figure 4.2. Typically, the reference measurements are acquired first. This is done because they typically have a higher intensity and are therefore ideal for finding the optimal exposure, defined as the highest possible integration time without saturating the camera. Once started, the program sets up the illumination wavelengths and an initial guess of the exposure times, T_0 to be used for the images. A targeted maximum intensity, I_{Target}, and

a tolerance, I_{Tol}, for this value are specified by the user. Then the filter is moved to the first illumination wavelength. The first image is acquired and passed to a check function. The check function asserts, if the maximum intensity, I_{Meas}, from the recorded image is within the interval $I_{\text{Target}} \pm I_{\text{Tol}}$. If the check is failed, the current exposure time, T_i, is changed to T_{i+1} according to the equation:

$$T_{i+1} = T_i \cdot (1 + \frac{I_{\text{Target}} - I_{\text{Meas}}}{I_{\text{Meas}}}) \tag{4.1}$$

And another image is acquired using the new exposure time. If the check passes, the image is saved, and the program checks if it should move to the next illumination wavelength or stop. Since the camera saves images in 8-bit format, the intensities in the camera can range from 0 to 255. Typical values of I_{Target} and I_{Tol} are 240 and 2 respectively, in order to avoid saturation. Once the reference measurement is done, the sample and dark measurements are performed using the, now static, exposure times used for reference measurements.

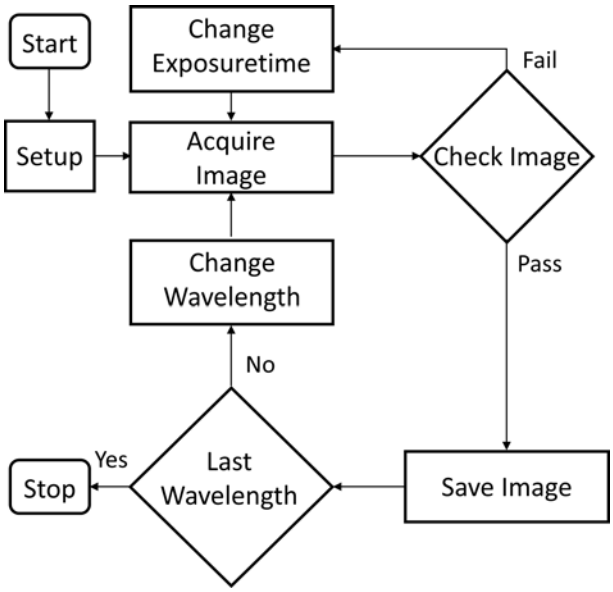

Figure 4.2: Flow chart showing how the imaging scatterometer reference measurements are performed using an dynamic exposure time. During the sample and dark measurements, the "Check Image" block will always pass.

The method to adjust the exposure time is based on the assumption that the response is linear with respect to exposure time, which was tested. The results can be seen for different wavelengths in figure 4.3. We can see that the signal increases linearly as a function of the exposure time until the camera is saturated. Furthermore, it can be seen that different wavelengths saturate at different exposure times, highlighting the benefit of the dynamic exposure time.
Examples of the analysis from a measurement set can be seen on figure 4.4. Here the measured sample is a silicon wafer with fields cover with nano-sized holes. This shows how the imaging scatterometer can be used to measure sub-beam-spot-area fields and how it can be used for a fast screening of macroscopic defects and homogeneity of nanostructures. A simple method to automate this is demonstrated in the following section.

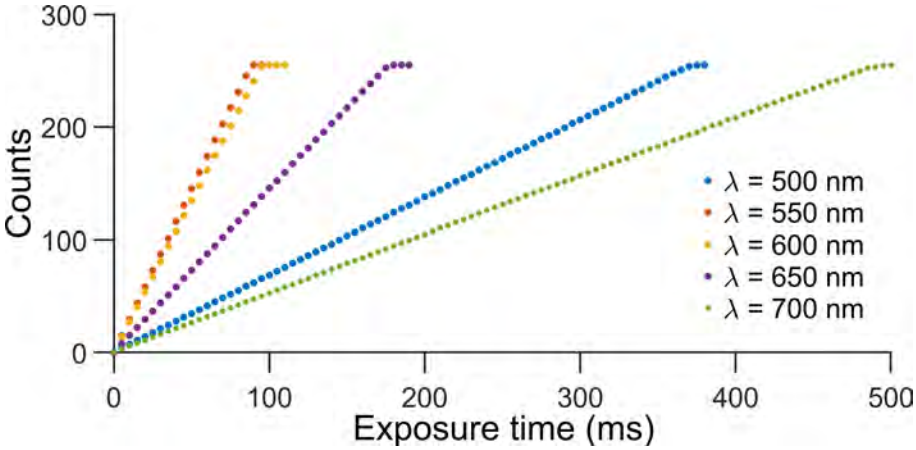

Figure 4.3: Maximum recorded intensity at different wavelengths using the first iteration on the imaging system on a plain Si100 wafer. The signal is seen to linearly increase with the exposure time until the camera is saturated.

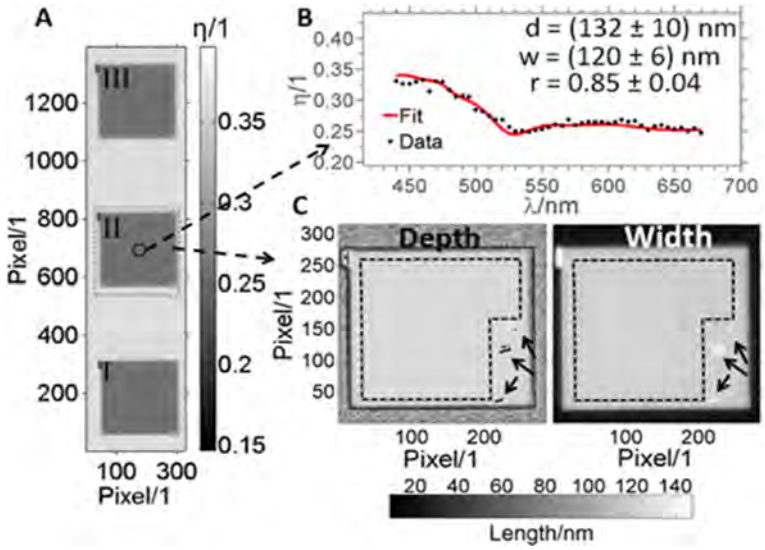

Figure 4.4: Application of the imaging scatterometry analysis. (A) measured image of the sample containing three nanostructured fields with areas of 250 x 250 μm^2. From here the user can select a pixel or an area. The first option (B), analyzing a single pixel, is similar to traditional scatterometry, with the advantage that the user can easily see what area of the sample is reconstructed and measure areas smaller than the spot size. The second option (C) gives a fast screening method of a large area. Here defects are evident and highlighted by arrows. The average depth and width of the area marked by dashed lines are found to be 128 ± 3 nm and 122 ± 4 nm respectively. Figure modified from refs. [36].

4.2 Automated Defect Detection

The screening of defects on the sample can become valueable if this process can be automated. A simple implementation of automation is described in the following: First the diffraction efficiency is calculated from a sample, reference and dark image acquired at a single wavelength. Next we find the nano-textured area. We find an expected signal from the structure at this specific wavelength using RCWA simulations and set a tolerance. All pixel values with a signal value within the tolerance is regarded as potential structured- area. Then a binary image is made, setting all potential structure pixels to one and all other pixels to zero. The center of gravity of the structured area is found using:

$$x_{center} = \frac{\sum x_i \cdot I_i}{\sum I_i} \quad \text{and} \quad y_{center} = \frac{\sum y_i \cdot I_i}{\sum I_i} \tag{4.2}$$

Where I_i is the value of the i'th pixel in the binary image. Based on information from the macroscopic sample geometry (a square in this case), a number of borders is placed around the center. The borders are expanded from the center, by cycling through the borders. In a cycle the borders are moved, one border at a time, by one pixel. If a move results in adding more unstructured pixels than structured pixels to the square, the border is moved back before going to the next border in the cycle. Once a cycle, where none of the borders have moved, is been completed, the structured area is defined. Once the structured area is found, defects are highlighted inside this area by taking the pixels not within the tolerance and reported as sample defects. Different steps are demonstrated in figure 4.5. Based on the size of the detected area, the number- and sizes of defects, making an automatic pass/fail check for the system would be simple. For the example shown in figure 4.5, 74 defects with a size of 10 or more pixels were found.

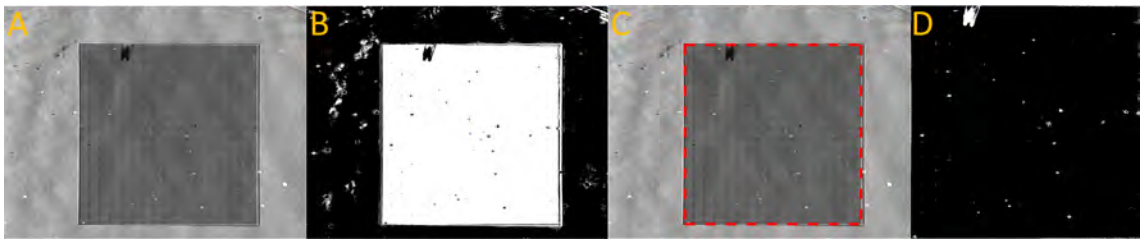

Figure 4.5: Simple implementation of automated defect detection. (A) Diffraction efficiency calculated at a wavelength of 630 nm. (B) Binary image based of the measured values in (A). (C) Estimate of the sample area marked by a red box. (D) Defects found within the marked area of (C).

4.3 Corner Rounding

In the paper below, it was found that the gratings were not sufficiently described by rectangles, and therefore, the rounding of the top corners was added as a model parameter. First the radius, r, of the circle describing the corner rounding is defined. Then the center of the circle is found as:

$$x_{center} = \frac{w}{2} - r \quad \text{and} \quad y_{center} = h - r \tag{4.3}$$

It is decided how many slabs are needed to describe the corner rounding, in the following paper 10 slabs were used. Since scatterometry is a volume sensitive technique, it is essential that the slabs represent the correct volume. A corner rounding formed by four slabs is sketched on figure 4.6, here the filled green regions show the over-representation of material and the orange regions show the under-representation of material. The height and the width of the slabs are adjusted so the area of the green regions is equal to the area of the orange regions. Once the more complex model

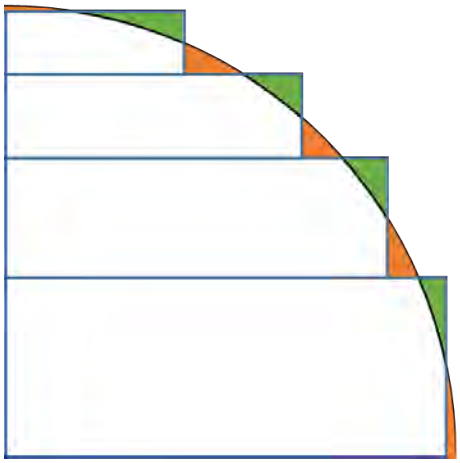

Figure 4.6: Illustration of a corner rounding described by four slabs. The green and orange regions shows the over and under representation of material respectively.

including corner roundings was used, the offset found with respect to the AFM was reduced. Based on the results, it is suggested to use AFM and scatterometry in combination, when possible. By doing this, one could use the AFM to lock the pitch and height of the structure in the inverse modeling, while the other parameters, not visible to the AFM, are found from scatterometry. This would work under the assumption that the sample has a homogeneous height and period distribution. This work was suggested in the EMPIR project: 3D-Nano and the results are reported in Chapter 8.

Preprint of paper 1

Title:

Study on Micro Gratings Using Imaging, Spectroscopic and Fourier Lens Scatterometry

Journal:

Journal of Micro- and Nano-Manufacturing, vol. 5 (2017)

Authors:

J. S. Madsen, P. E. Hansen, P. Boher, D. Dwarakanath, J. F. Jørgensen, B. Bilenberg, J. Nygård and M. H. Madsen

DOI of published paper:

10.1115/1.4036889

Study on micro-gratings using imaging, spectroscopic and Fourier Lens scatterometry

Abstract

With new fabrication methods for mass production of nano-textured samples there is an increasing demand for new characterization methods. Conventional microscopes are either too slow and/or too sensitive to vibrations. Scatterometry is a good candidate for in-line measuring in an industrial environment as it is insensitive to vibrations and very fast. However, as common scatterometry techniques are non-imaging, it can be challenging for the operator to find the area-of-interest on a sample and to detect defects. We have therefore developed the technique imaging scatterometry, in which the user first has to select the area of interest after the data has been acquired. In addition, one is no longer limited to analyze areas equal to the spot size, and areas down to 3 µm × 3 µm can be analyzed. The special method Fourier Lens scatterometry is capable of performing measurements on misaligned samples and is therefore suitable in a production line. We demonstrate characterization of 1D and 2D gratings from a single measurement using a Fourier Lens scatterometer. In this paper we present a comparison between spectroscopic scatterometry, the newly developed imaging scatterometry and some state-of-art conventional characterization techniques, atomic force microscopy and confocal microscopy.

1. Introduction

With modern technology it is possible to reproduce fascinating structures from nature [1]. As an example grating structures can be used for decorating surfaces with structural colors [2, 3], i.e. surfaces where diffraction is used to give them an iridescence look. Some of the advantages of structural colors are that they can be fabricated without a paint step [4] and that they are non-degradable [1, 5]. Nano-textures have also been used to make super-hydrophobic surfaces inspired by the lotus leaf [6] and hydrophilic surfaces known from the carnivorous pitcher plant [7].

New methods for highly parallel manufacturing, such as injection molding or roll-to-roll (R2R), are becoming available for fabrication of nano-textured samples [8, 9]. The dramatically decreased production time allow new products to enter the consumer market. However, the quality control systems are not improving at the same pace as the fabrication techniques and therefore new characterization techniques are highly needed [10].

Scatterometry is a promising method for in-line characterization as it is fast and robust technique. Basically scatterometry is an optical method where measured diffraction intensities from nano-textured surfaces are compared to modelled data [11–14]. Often an inverse modelling approach is used, in which the data are related to a set of model parameters. For further reduction in computation time, especially suited for in-line characterization, one can use a library search strategy [11,15]. Here *a priori* information is used to generate a database with diffraction efficiencies for expected structures. The best match to the experimental data can then be found using a simple database lookup.

The first scatterometers used a monochromatic laser and different angles of incidence [16], and are referred to as angular scatterometers. Typically an angular scatterometer has a laser on a goniometric stage and a goniometric detector system. The sample is illuminated by the laser and the detector system is moved to measure the different diffraction orders. This is a high resolution but time consuming measuring configuration. Instead one can use a Fourier Lens system [17] for scatterometry analysis, where Fourier optics is used to simultaneously measure all diffraction orders from a grating at a single wavelength. This makes it possible to perform angular scatterometry without any mechanical movements. Furthermore, no alignment is necessary, as the orientation of the sample can be found in the data analysis [13].

Imaging scatterometry is a new and versatile technique for characterization of nano-textured areas [18]. It is capable of analyzing areas down to a few μm^2 with nanometer accuracy. Furthermore the technique makes it easy for the user to find a specific area, as the area-of-interest first has to be selected after the measurements have been obtained. It is insensitive to small vibrations where the displacement of the sample during the measurement is less than the size of a homogeneous area analysed. However, until now the imaging scattering technique has only been used to analyze grating structures with a pitch similar or smaller than the wavelength of visible light. In this paper we present a method to perform measurements on gratings with a pitch over 3 µm by effectively reducing the numerical aperture of the objective.

Common techniques for characterization of the height of grating structures include atomic force microscopy (AFM) and confocal microscopy [19], see Fig. 1. Measurements using these techniques have been obtained in this study to compare the different techniques. However, both these techniques are very sensitive to vibrations and are therefore challenging to integrate in a production line.

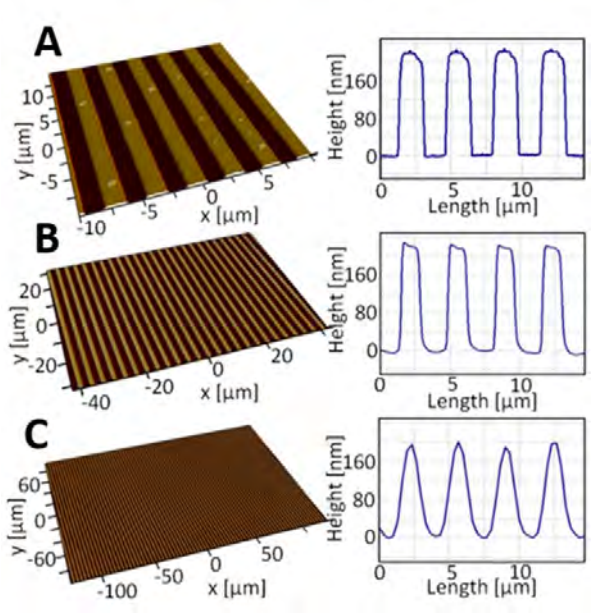

Fig 1. 3D microscope images with corresponding profiles for a segment in the center of each image, for 3.3 µm 1D silicon grating. (A) AFM, (B) confocal microscope, 150× objective, and (C) confocal microscope, 50× objective.

2. Method

In scatterometry measurements of diffraction efficiencies are compared to model generated data as shown in Fig. 2. The experimental wavelength dependent diffraction efficiencies, η(λ), are calculated as the ratio of the diffracted light with respect to the incoming light. To do that, three sets of wavelength dependent, λ, light intensity measurements are necessary: A sample set, I_{sample}, a reference sample set, I_{ref}, and a dark signal set, I_{dark}. The diffraction efficiency is then found using [11],

$$\eta(\lambda) = \frac{I_{\text{sample}}(\lambda) - I_{\text{dark}}(\lambda)}{I_{\text{ref}}(\lambda) - I_{\text{dark}}(\lambda)} R(\lambda) \quad (1)$$

where R(λ) is the wavelength dependent reflection coefficient of the material used for the reference measurement; in our case, Si(100) was used. The background, which comes from detector noise and light reflected by the objective and iris, is taken into account from the dark measurement.

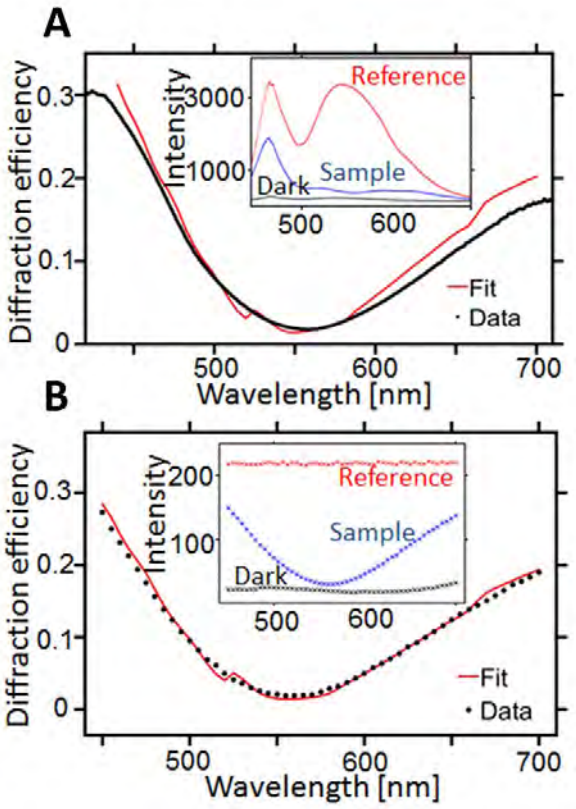

Fig. 2. Experimental data and best fit for scatterometry data for a 1D grating with a pitch of 3.3 µm. (A) Spectrometer based scatterometry. Best reconstruction for a height of (422 ± 4) nm and a width of (1230 ± 30) nm. (B) Imaging scatterometry. Best reconstruction for a height of (426 ± 6) nm and a width of (1240 ± 30) nm.

An inverse modelling approach is used for reconstruction of grating shape parameters from the found diffraction efficiencies. A set of model parameters, $\boldsymbol{\alpha}$, describing the sample, and $\boldsymbol{\Omega}_i$, describing the measuring conditions, are used to simulate the diffraction efficiencies, $f(\boldsymbol{\Omega}_i, \boldsymbol{\alpha})$. The simulations are based on rigorous coupled wave analysis, RCWA, where the grating is divided into rectangular slabs [11].

The software package InfoScat [20] has been used for simulation of diffraction efficiencies based on RCWA. In the software the user specify grating parameters $\boldsymbol{\alpha}$, typically period, height and width, and illumination conditions $\boldsymbol{\Omega}$, typically wavelength, angle of incidence and polarization. In this specific study, the period of the gratings is considered known. The angle of incidence is zero and the polarization of the light is transverse electric with respect to the grating lines. Thus only the height and width are varied for each wavelength. The gratings are assumed to be homogeneous.

The simulation time for diffraction on a simple 1D grating for a single wavelength is around 40 ms on a standard computer (e.g. Intel i5 processer). In this study wavelengths of 400 nm to 700 nm are simulated in steps of 5 nm resulting in a in a computation time of 2-3 seconds for each structure. All the simulated structures and their diffraction efficiencies are stored in a database. With a typical database size of 10000 grating shapes, it takes a few hours to compute the database. However, this computation only has to be done once. Using a faster computer can drastically reduce the computation time.

Each simulated structure is then compared to the experimental data using a χ^2-minimization given by,

$$\chi^2 = \frac{1}{N}\sum_{i=1}^{N}\left(\frac{\eta_i - f\left(\mathbf{\Omega}_i, \boldsymbol{\alpha}\right)}{\delta\eta_i}\right)^2, \qquad (2)$$

where η_i is the *i*'th measured diffraction efficiency, $\delta\eta_i$ is the error on the *i*'th measured diffraction efficiency and *N* is the number of measured diffraction efficiencies. The simulated structure with the lowest χ^2-value is selected as the best description of the grating structure. The confidence limits for the fitting parameters are found using constant chi-square boundaries [11, 16].

3. Experimental setup

Five different characterisation techniques are used in this study: Spectroscopic scatterometry, imaging scatterometry, Fourier lens scatterometry, atomic force microscopy and confocal microscopy. An introduction of the instruments is given in this section.

3.1. Scatterometer

The scatterometer is a custom built system based on a Navitar optical microscope (12× zoom) equipped with a fiber coupled cold white LED light source (Qioptiq, CLS-LED USB). The setup is sketched in Fig. 3. The light passes through a diffuser, to prevent imaging of light source, before it is collimated and polarized using Glan-Laser linear polarizer crystal and coupled into the microscope with a beam splitter. The microscope is equipped with an infinity-corrected objective with a magnification of 4× (Olympus, RMS4X-PF, NA = 0.13). The resolution of the microscope is limited by the numerical aperture of the objective to around 3 µm. An iris is placed in front of the objective, and when closed (Ø = 0.5 mm), it is used to avoid first and higher order reflections from a diffraction grating entering the objective.

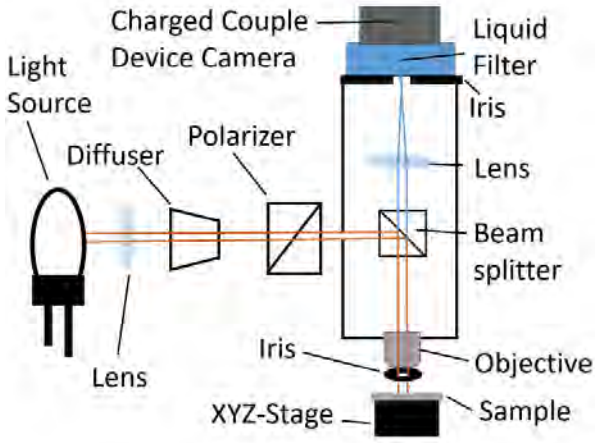

Fig. 3. Experimental data and best fit for scatterometry data for a 1D grating with a pitch of 3.3 µm. (A) Spectrometer based scatterometry. Best reconstruction for a height of (422 ± 4) nm and a width of (1230 ± 30) nm. (B) Imaging scatterometry. Best reconstruction for a height of (426 ± 6) nm and a width of (1240 ± 30) nm.

With the iris installed it is possible to analyze structures with a period up to several µm without collecting the signal from the diffraction orders.

In the image plane a monochrome 1.3 megapixel CCD camera (Pixelink, PL-B957) is interchangeable with a lens system and a spectrometer (Ocean Optics, USB-2000) as described in [21]. The spectrometer was calibrated using a low pressure krypton calibration light source with traceable spectral lines. To reduce the effective spot size on the sample a second iris was

installed in front of the camera/spectrometer. The iris was not touched when switching the detectors. Data was analyzed using the InFoScat software package [20].

3.2. Imaging scatterometer

The imaging scatterometer setup is a modified version of the scatterometer described above. A tunable band pass filter (Perkin Elmer, Varispec VIS-07-20) is mounted in front of the camera instead of switching to the spectrometer as described in [18]. The filter has a bandwidth of around 10 nm in the range from 400 nm to 700 nm and images were obtained in the wavelength range from 450 nm to 700 nm in steps of 5 nm. The reduced wavelength range was due to the low intensity from the light source in these areas and a limited transmission of the filter. During the reference measurement, I_{ref}, an algorithm was run to maximize the signal for each wavelength while avoiding saturation of the camera. This is seen as a constant reference intensity in the insert of Fig. 2(B) in contrast to the spectroscopic scatterometer, Fig. 2(A), where the reference intensity reflects the intensity of the light source. This enables the user to utilize the full dynamical range of the system. The images were stacked to form a multi-spectral image. An area of interest is selected from the multi-spectral image and analyzed using Eqs. (1) and (2) in Matlab.

3.3. Fourier Lens scatterometer

A Fourier lens system collects light from one spot on the sample surface and projects light emitted in one direction to a single point in the Fourier plane [22]. The light guidance is achieved from the design of the lens system and has thus no moving components. We have used an EZContrast system (ELDIM, France) with a maximum collection angle up to 88° for the scatterometry measurements. One should carefully note the difference to Fourier scatterometers, which are typically based on an interferometric setup with normal objectives [19, 20, 21]. Light scattered from the sample are distributed throughout a semi-sphere over the sample according to a bidirectional reflection distribution function (BRDF) [26]. Measurements of the BRDF are reported as the light reflected from the sample with respect to the incoming light. The system can measure in the luminance range from $10^{-3}\,\frac{\mathrm{cd}}{\mathrm{m}^2}$ to $10^{3}\,\frac{\mathrm{cd}}{\mathrm{m}^2}$.

A narrow band width of wavelengths (typically around 8 nm) can be selected using optical filters mounted on a motorized stage. A total of 31 filters are available in the visible and we have chosen to use a wavelength centered at 550 nm for the scatterometry measurements. The filters are placed in front of the CCD sensor placed in the Fourier plane. The samples are illuminated using a 300 µm fiber and a white light fiber based light source is used for illumination. A beam splitter is used to couple the light into the beam path.

The measurements are made with double or triple exposure at each wavelength to enhance the dynamic range of the measurement. Each measurement has been calibrated using the integrated intensity on a white reference measured in the same illumination conditions. The measurements are also corrected from the distortion of the Fourier plane (real BRDF values). These corrections are performed on all the individual measurements. When performing scatterometry this means the corrections applies to the dark, reference and sample measurements. In this case we have used a Si(100) substrate as the scatterometry reference.

Data have been extracted using the EZcom software and the data analysis performed in Matlab. Typical data sets are shown in Fig. 4.

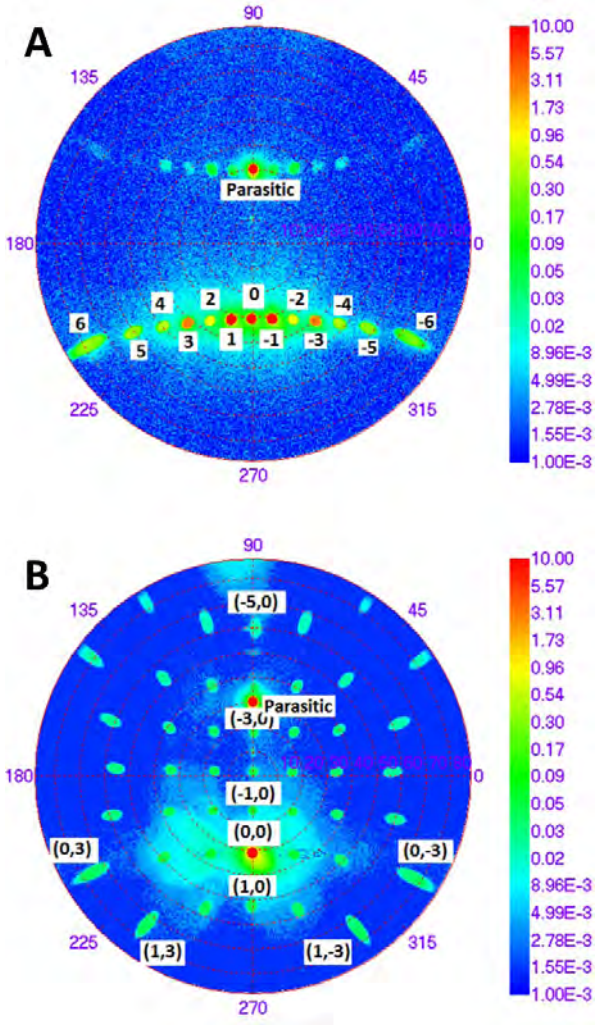

Fig. 4. BRDF measurements obtained with the Fourier Lens system at a wavelength of 550 nm. (A) 1D grating with a pitch of 4 µm and a height of around 500 nm. (B) quadratic 2D grating with a pitch of 2 µm. The different diffraction orders are indicated. The parasitic light arises from multiple reflections in the optics and is avoided in the data analysis.

It should be emphasized that when first the data have been obtained and retrieved from the images, the data analysis is identical to analysis of data obtained using an angular scatterometer [11]. The difference is therefore only that all data are collected in a single measurement, and that no alignment of the sample is necessary [17].

For labelling of diffraction from 2D gratings we use the Miller indices notation [17] as known from X-ray scattering [27] and electron beam microscopes [28]. This gives a unique identifier to all the diffraction spots, such that the simulated and measured diffraction efficiencies can be matched.

3.4. Atomic force microscope

For the AFM measurements of the heights of the gratings we used a metrology AFM (Park Systems, NX20) in tapping mode equipped with PointProbe Plus probes (Nanosensors), with a specified apex radius <10 nm. The AFM has an *xy*-stage equipped with optical distance sensors and a *z*-flexure stage equipped with strain gauge distance sensors. The microscope was calibrated in the *z*-direction using a step height standard as described in [29]. Images of an area of at least 20 µm x 5 µm of the 1D gratings were obtained for each sample with the fast scan axis perpendicular to the ridges. The images were analyzed using the step height module in SPIP (ver. 6.5.1, Image Metrology) and following the ISO 5436 standard for measuring step heights. A profile for each line scan was extracted and the height is the mean of all ridges in all scan lines. At least 50 height measurements were obtained for each sample. A typical image is shown in Fig. 1(A).

3.5. Confocal microscope

Confocal measurements were obtained using a Plu Neox (Sensofar) microscope equipped with a 50× and a 150× objective with a numerical aperture (NA) of 0.80 and 0.95, respectively. The field of view for the 50× and 150× objective is 254.6 µm × 190.9 µm and 84.9 µm × 63.6 µm, respectively. The microscope has been calibrated using 2D transfer standards with a checkerboard pattern.

See typical images in Fig. 1(B,C). All gratings were aligned with ridges perpendicular to the long image axis. The confocal microscopy images were also analyzed in SPIP but using a histogram based approach. The images were levelled, and then the center parts selected using area-of-interests to minimize the effects of aberrations, which are most pronounced at the edge of the objective lens. A histogram was made from this area-of-interest and the distance between the centers of the two main peaks, was used as the estimate of the height of the ridges.

4. Results and discussions

A series of 1D gratings etched with a pitch of 3.3 µm was used to compare the above mentioned characterization methods. A total of ten silicon wafers with heights in the range from 100 nm to 500 nm have been examined in this study. All wafers have been characterized using the methods described above, with the exception of the Fourier lens scatterometer. It is assumed that the optical properties of the silicon are identical to bulk silicon. From simulations it has been found that adding a native oxide layer with a thickness up to 10 nm has a negligible influence on the reconstruction. Examples of measurements for the characterization techniques are shown in Figs. 1 and 3 and all data in Tab. 1.

Sample	Scat.[a] [nm]	Imaging scat.[a] [nm]	AFM[b] [nm]	Confocal 150× [a] [nm]	Confocal 50× [a] [nm]
1	105 ± 4	105 ± 8	109 ± 4	119 ± 14	102 ± 20
2	100 ± 2	101 ± 6	114 ± 4	113 ± 14	98 ± 20
3	200 ± 6	216 ± 10	224 ± 6	224 ± 19	201 ± 27
4	209 ± 8	215 ± 10	224 ± 9	251 ± 19	194 ± 27
5	338 ± 4	332 ± 6	334 ± 6	343 ± 24	289 ± 35
6	335 ± 4	333 ± 8	331 ± 6	369 ± 24	289 ± 35
7	422 ± 4	426 ± 6	436 ± 8	423 ± 30	419 ± 44
8	422 ± 4	428 ± 6	438 ± 8	447 ± 30	415 ± 44
9	530 ± 10	534 ± 8	547 ± 11	537 ± 35	508 ± 53
10	535 ± 8	541 ± 10	555 ± 14	556 ± 35	538 ± 53

[a]The ± indicates the 95 % confidence interval (see text)
[b]The ± indicates the expanded uncertainty (k=2)

Tab. 1. Heights of a series of 1D gratings etched in silicon measured using scatterometry, imaging scatterometry, atomic force microscopy, and confocal microscopy with two different objectives.

The AFM measurements are considered to be the most trustable measurements as we have been able to follow a standardized method using a calibrated and traceable instrument. For the AFM measurements we have indicated the expanded uncertainty (k=2). The other methods either relies on a parameterized model or a non-standardized (the histogram approach) method for analysis of the data. For these data we have indicated a 95 % confidence interval under the assumption that the model is correct. It is stressed that this interval is not equivalent to an uncertainty, since experimental uncertainties are not propagated throughout the inverse modelling. The uncertainty is higher than the given confidence interval and will require a calibration of the instrument and uncertainties on all parameters in the model. The first steps towards a reference standard for scatterometry has recently been presented [30].

For specular reflection scatterometry systems one should be careful not to collect higher order diffraction. From Bragg's law it is known that the distance between the diffraction orders is inversely proportional to the grating pitch, Γ. In other words Γ should not exceed [21]:

$$\Gamma < \frac{\lambda_{min}}{2\sin(2\theta_{\mathrm{NA}})} \qquad (3)$$

where λ_{min} is the minimum wavelength measured by the spectrometer and θ_{NA} is the collection angle for an objective with numerical aperture NA = sin(θ_{NA}) in air. The $2\theta_{\mathrm{NA}}$ term arises as the angle of both the incoming and outgoing light is taken into account. For this study we have demonstrated that by installing an iris in front of the objective, the NA can effectively be reduced, and we can measure on gratings with a much larger pitch. It is preferential to adjust the iris to let as much light as possible through and still shielding for the first order reflections to obtain a good signal to noise ratio. However, a smaller numerical aperture reduces the lateral resolution [31], this effect is observed when comparing Fig. 1(B) and Fig. 1(C).

The different characterization methods, except the Fourier Lens scatterometry, are compared against each other in Fig. 5(A). Ideally the measured height should be the same independent of the used technique, as indicated with a solid line in all the graphs. The deviation between the different instruments and the AFM is reported in Fig. 5(B). As a general trend the heights measured with scatterometry and imaging scatterometry are closely related. This shows that the newly developed imaging scatterometry technique is very comparable to scatterometry and a validation of one technique, is expected to also apply for the other. However, as the reconstruction of the data sets from both scatterometry and imaging scatterometry are based on the same database of simulated diffraction efficiencies, there might be an offset with respect to the other techniques.

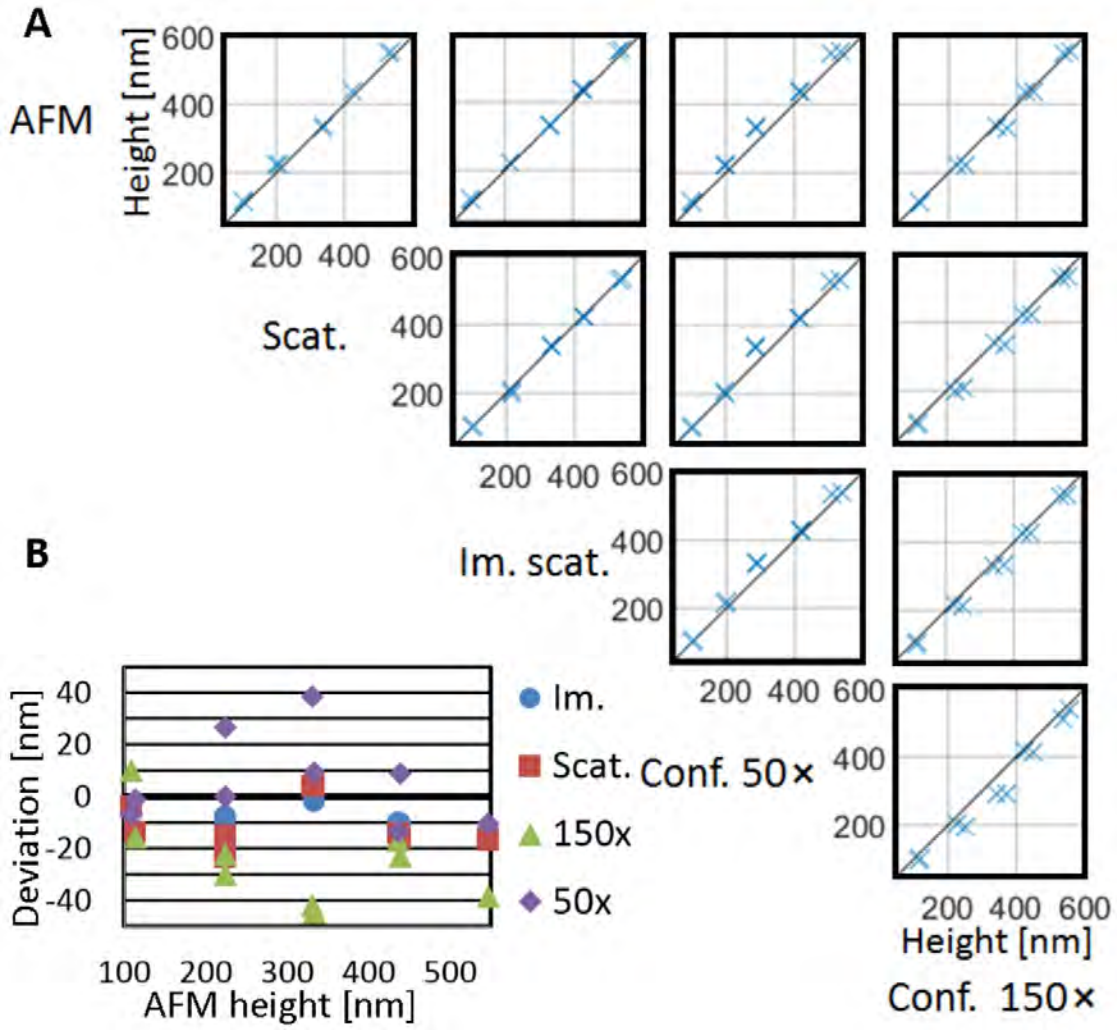

Fig. 5. Comparison of measurements results for ten 1D gratings of different heights. (A) Direct comparison of all the techniques compared individually. The name of the characterization method applies to graphs both horizontally and vertically. As a guide to the eye a solid line is plotted to indicate when the two methods give the same result. Further away from this line indicates a deviation between the techniques. (B) Deviation of all measurements with respect to the imaging scatterometry measurements plotted as a function of the heights found using imaging scatterometry.

The confocal microscope measurements generally have the largest deviation from the AFM. It is seen that the 150x objective tends to overestimate the height compared to the AFM, while the 50x objective underestimates the height compared to the AFM. As seen from Fig. 1 the confocal microscope does not resolve the sharp corners of the grating structure due to the knife-edge effect [32].

The difference between the found height value using AFM and imaging scatterometry is seen in Fig. 6. It is observed that the height measured by AFM is systematically higher than by imaging scatterometry. We attribute this height offset to the simplified model used in the scatterometry reconstruction, where the shape of the grating is assumed to be perfect boxes. Since scatterometry is very sensitive to the volume of the grating, a non-rectangular grating model can change the best fitting height. We have therefore investigated the influence of adding additional fitting parameters, like rounding of the bottom corners, top corners or a sidewall angle.

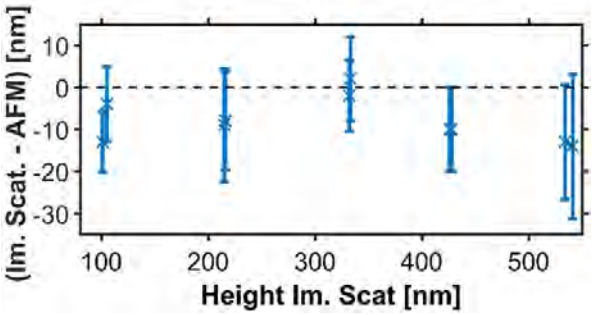

Fig. 6. Difference between the heights estimated by the imaging scatterometer and by the AFM. The errorbars indicate a combination of the 95% confidence interval limits for the imaging scatterometer and the k=2 uncertainties of the AFM measurements found by treating the 95% confidence interval as an uncertainty and performing standard error propagation. The dashed line is plotted through zero to guide the eye. A clear offset is observed.

It is challenging to fabricate sharp corners in the manufacturing of samples. We have therefore included rounding of the top corners to the model as sketched in Fig. 7(A). To include the rounding of the top corner, a circle with a radius, *r*, is placed near the grating corner such that the center of the circle has the distance *r* from the sidewall and the top of the grating. The area outside this circle is cut off by approximating the top of the grating with 10 slabs of varying heights and widths. The radius *r* is varied during simulations and is reported as the rounding of the top corner.

The analysis presented in Fig. 3, is repeated with a new simulated model with top corner rounding added as a parameter. The measured diffraction efficiency from the spectroscopic scatterometer and the best fitting model can be seen in Fig. 7(B). Using this new model best the fit is now found for a height of (435 ± 8) nm and a top corner rounding radius of (200 ± 20) nm. This height is in agreement with the height found by the AFM. For the new model the found chi-square is: χ^2 = 0.20 compared to χ^2 = 0.55 for the rectangular model. The height and the top rounding radius found by the imaging scatterometer using this new model is (434 ± 10) nm and (220 ± 30) nm respectively.

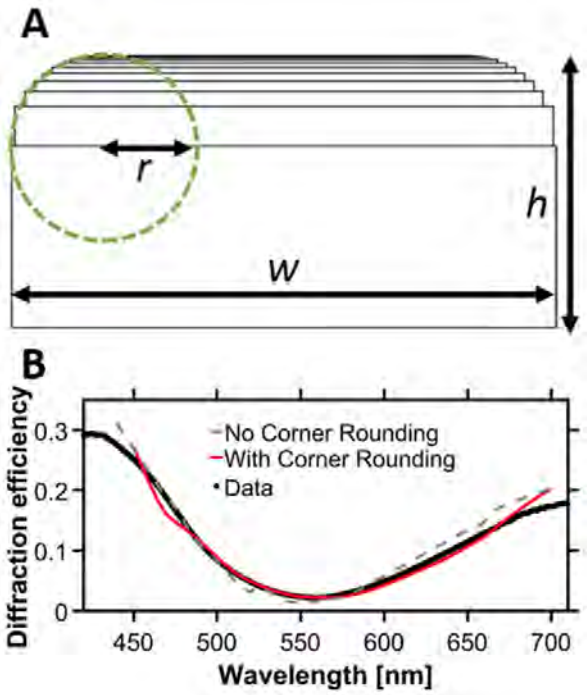

Fig. 7. Experimental data and best fit for scatterometry data for a 1D grating with a pitch of 3.3 µm using a model with rounded top corners. (A) Sketch of the new model with rounded top corners. The rounding, *r*, is defined as the radius of the green dashed circle while the height, *h*, and the width, *w*, are the same as in the rectangular model. (B) Spectrometer based scatterometry, using a model with rounded corners. Best reconstruction is found for a height of (435 ± 4) nm and a rounding of (200 ± 20) nm. The chi-square found using rounded corners is: $\chi^2 = 0.20$, compared to $\chi^2 = 0.55$ for a rectangular model.

For reference measurements of the top corner rounding radius a tilted AFM setup similar approach to the method described in [21] has been used. The sample was positioned at an angle of 12° under the AFM. The top rounding radius is found to (220 ± 40) nm, by fitting a circle to the corner points. A profile from 250 averaged lines can be seen on Fig. 8. This result should be used as a crude estimate, since it does not follow a standardized method. The top rounding estimated by the AFM and the scatterometers are in agreement, suggesting that this is a physical feature of the sample that should be included in the model in order to achieve a higher accuracy of the reconstruction.

Different grating models or additional model parameters could be included to optimize the reconstruction, however this should be done carefully to avoid over fitting. An example could be the bumps, most likely dust particles, observed on the AFM images in Fig. 1. The material ratio of these bumps to the grating volume is much less than one percent, and hence their contribution to the diffraction efficiencies is negligible. We stress, that if additional parameters are added, one should consider how physical those parameters are. Therefore scatterometry is most useful when a priori information of the sample is available.

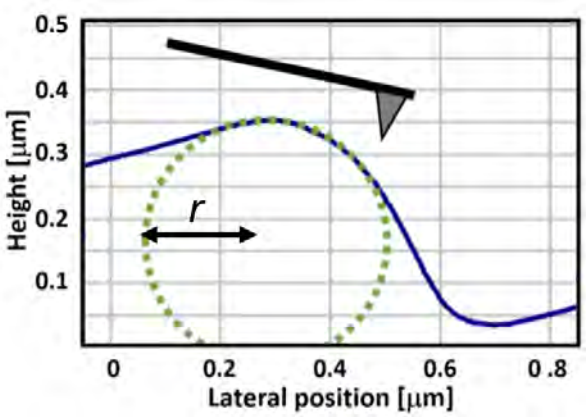

Fig. 8. AFM Profile averaged from 250 lines. A rounding of the corner is observed and highlighted by the dashed line.

For validation of the Fourier Lens scatterometer we used a Si(100) sample with both 1D and 2D grating structures. The 1D grating consisted of lines with a pitch of 4 µm and a height of (525 ± 15) nm measured using a metrology AFM, where ± denotes the expanded uncertainty. The 2D gratings consist of holes in a quadratic array with equal pitches of 2 µm. The width of the holes is 300 nm and due to the high aspect ratio, it was not possible to measure the height with AFM. The width of the holes is estimated to (330 ± 40) nm with AFM. It is challenging to measure the diameter of holes with an AFM as the size of the tip influences the measurements. We have corrected for the tip shape in the analysis [33].

Experimental data for the Fourier Lens scatterometer is shown in Fig. 9. The data have been normalized to the zeroth order diffraction, which is therefore exact 1. For the 2D grating the diffraction efficiency of the zeroth order is much higher than all the other peaks. The figure is therefore zoomed in on the other diffraction orders and the zeroth order is outside the range.

For the 1D grating the height is estimated to be 530 nm, which is inside the uncertainty range of the reference AFM measurements. The 2D grating is more challenging to characterize as the material ratio (holes to total volume) is less than 2 %. In general, the strongest diffraction is obtained when the material ratio is close to 50 %, as is the case for the 1D grating. From the data in Fig. 9(B) there does not exist a unique solution for the height. However, all found solution have the same hole diameter estimated to be (320 ± 20) nm, where the ± indicates the 95 % confidence interval. The same solution is found for analysis of data obtained at a wavelength of 451 nm and it is also within the measured value by AFM.

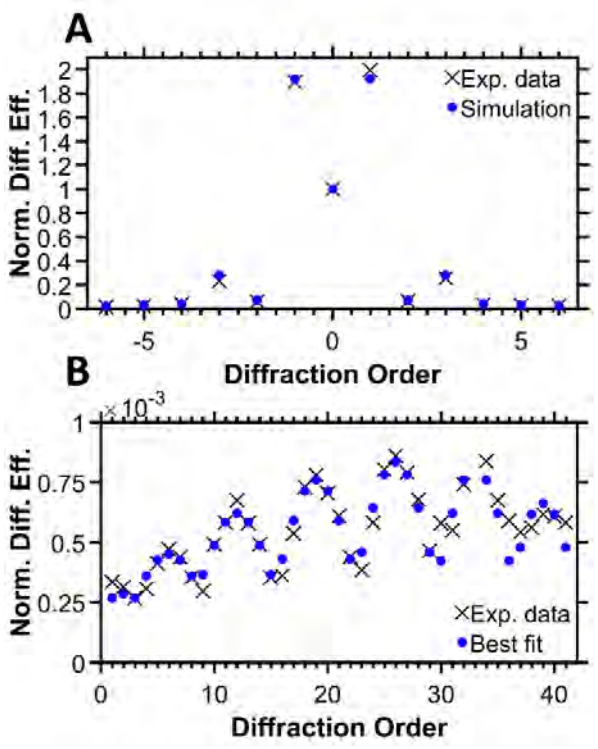

Fig. 9. Experimental data obtaining using the Fourier Lens scatterometer using a wavelength of 550 nm and best fitting models. Diffraction efficiencies are normalized with respect to the zeroth-order. (A) Measurements on a 1D grating. (B) Measurements on a 2D grating.

5. Conclusions

We have compared four different characterization techniques for measurements on 1D gratings with a pitch of 3.3 µm and different heights. The new technique imaging scatterometry has been validated with respect to spectroscopic scatterometry, AFM and confocal microscopy. The study suggests that scatterometry can be a solution to the current challenges in highly parallel manufacturing. We have demonstrated that by effectively reducing the numerical aperture of an objective, gratings with a pitch much longer than the used wavelengths can be characterized with a scatterometer built into a microscope and by imaging scatterometry. This result makes it possible to characterize embedded microstructures using visible light, with state of the art accuracy. By combining imaging scatterometry and the software package InFoScat, one can get a very user friendly scatterometry technique.

We have presented measurements of 1D and 2D gratings using a Fourier Lens scatterometer. The system is able to measure both the height and the width of 1D gratings and the width of 2D gratings consisting of holes. The Fourier Lens scatterometer allows for alignment free characterization of gratings, making it suitable for in-line characterization.

A height offset of ~10 nm is found between AFM measurements and scatterometry measurements. We have shown that this offset can be reduced with a more complex model of the

grating shape by including round top corners in the simulations. This fine-tuning of the model increases the accuracy of scatterometry, provided that pre-knowledge of the sample can justify additional model parameters

Funding

This work has received financial funding from the EMPIR programme co-financed by the Participating States and from the European Union's Horizon 2020 research and innovation programme through the
project 14IND09 MetHPM, the Eurostars project E8875 - InFoScat, Qubiz of the Innovation Fund Denmark and The Danish Agency for Science, Technology and Innovation.

REFERENCES

[1] A. Saito, 2011, "Material design and structural color inspired by biomimetic approach", Sci. Technol. Adv. Mater. 12 064709. doi:10.1088/1468-6996/12/6/064709.
[2] S. Kinoshita, S. Yoshioka, J. Miyazaki, 2008, "Physics of structural colors", Rep. Prog. Phys. 71 076401. doi:10.1088/0034-4885/71/7/076401.
[3] H. Fudouzi, 2011, "Tunable structural color in organisms and photonic materials for design of bioinspired materials", Sci. Technol. Adv. Mater. 12 064704. doi:10.1088/1468-6996/12/6/064704.
[4] K. Kumar, H. Duan, R.S. Hegde, S.C.W. Koh, J.N. Wei, J.K.W. Yang, 2012, "Printing colour at the optical diffraction limit", Nat. Nanotechnol. 7 557–561. doi:10.1038/nnano.2012.128.
[5] F. Cheng, J. Gao, T.S. Luk, X. Yang, 2015,"Structural color printing based on plasmonic metasurfaces of perfect light absorption", Sci. Rep. 5 11045. doi:10.1038/srep11045.
[6] Z. Guo, W. Liu, 2007,"Biomimic from the superhydrophobic plant leaves in nature: Binary structure and unitary structure", Plant Sci. 172 1103–1112. doi:10.1016/j.plantsci.2007.03.005.
[7] K. Koch, W. Barthlott, 2009,"Superhydrophobic and superhydrophilic plant surfaces: an inspiration for biomimetic materials", Philos. Trans. R. Soc. Math. Phys. Eng. Sci. 367 1487–1509. doi:10.1098/rsta.2009.0022.
[8] M. Zalkovskij, L.H. Thamdrup, K. Smistrup, T. Andén, A.C. Johansson, N.J. Mikkelsen, M.H. Madsen, J. Garnæs, T.T. Kristiansen, M. Diemer, M. Døssing, D. Minzari, P.T. Tang, A. Kristensen, R. Taboryski, S. Essendrop, T. Nielsen, B. Bilenberg, 2015, "Smart plastic functionalization by nanoimprint and injection molding", in: D.J. Resnick, C. Bencher (Eds.), p. 94230T. doi:10.1117/12.2085766.
[9] M. Calaon, M.H. Madsen, J. Weirich, H.N. Hansen, G. Tosello, P.E. Hansen, J. Garnaes, P.T. Tang, 2015, "Replication fidelity assessment of large area sub- μm structured polymer surfaces using scatterometry", Surf. Topogr. Metrol. Prop. 3 045005. doi:10.1088/2051-672X/3/4/045005.
[10] J.A. Slotwinski, E.J. Garboczi, 2015, "Metrology Needs for Metal Additive Manufacturing Powders", JOM. 67 538–543. doi:10.1007/s11837-014-1290-7.
[11] M.H. Madsen, P.-E. Hansen, 2016, "Scatterometry—fast and robust measurements of nano-textured surfaces", Surf. Topogr. Metrol. Prop. 4 023003. doi:10.1088/2051-672X/4/2/023003.
[12] P. Petrik, N. Kumar, G. Juhasz, C. Major, B. Fodor, E. Agocs, T. Lohner, S.F. Pereira, H.P. Urbach, M. Fried, 2014, "Optical characterization of macro-, micro- and nanostructures using polarized light", J. Phys. Conf. Ser. 558 012008. doi:10.1088/1742-6596/558/1/012008.
[13] C. Raymond, 2005, "Overview Of Scatterometry Applications In High Volume Silicon Manufacturing", in: AI. pp. 394–402. doi:10.1063/1.2062993.
[14] D.G. Seiler, National Institute of Standards and Technology (U.S.), eds., 2003, "Characterization and metrology for ULSI technology: 2003 International Conference on Characterization and Metrology for ULSI Technology", Austin, Texas, 24-28 March, American Institute of Physics, Melville, N.Y, 2003.
[15] R. Koops, P. Sonin, M. van Veghel, O. El Gawhary, 2014, "A compact new-concept ellipsometer for accurate large scale thin film measurements", J. Opt. 16 065701. doi:10.1088/2040-8978/16/6/065701.
[16] C.J. Raymond, "Metrology of subwavelength photoresist gratings using optical scatterometry", 1995, J. Vac. Sci. Technol. B Microelectron. Nanometer Struct. 13 1484. doi:10.1116/1.588176.

[17] M.H. Madsen, P. Boher, P.-E. Hansen, J.F. Jørgensen, 2016, "Alignment-free characterization of 2D gratings", Appl. Opt. 55 317. doi:10.1364/AO.55.000317.
[18] M.H. Madsen, P.-E. Hansen, 2016, "Imaging scatterometry for flexible measurements of patterned areas", Opt. Express. 24 1109. doi:10.1364/OE.24.001109.
[19] R.K. Leach, 2014, "Fundamental principles of engineering nanometrology", Second edition, Elsevier, William Andrew, Amsterdam.
[20] Home - InfoScat, (n.d.). http://www.infoscat.com/ (accessed December 14, 2016).
[21] M.H. Madsen, P.-E. Hansen, M. Zalkovskij, M. Karamehmedović, J. Garnæs, 2015, "Fast characterization of moving samples with nano-textured surfaces", Optica. 2 301. doi:10.1364/OPTICA.2.000301.
[22] T. Leroux, 1993, "Fast contrast vs. viewing angle measurements for LCDs", in: Proc. 13th Int Disp. Res. Conf. Eurodisplay 93.
[23] S. Roy, N. Kumar, S.F. Pereira, H.P. Urbach, 2013, "Interferometric coherent Fourier scatterometry: a method for obtaining high sensitivity in the optical inverse-grating problem", J. Opt. 15 075707. doi:10.1088/2040-8978/15/7/075707.
[24] V. Ferreras Paz, S. Peterhänsel, K. Frenner, W. Osten, A. Ovsianikov, K. Obata, B. Chichkov, 2011, "Depth sensitive Fourier-Scatterometry for the characterization of sub-100 nm periodic structures", in: B. Bodermann (Ed.): p. 80830M. doi:10.1117/12.889439.
[25] O. El Gawhary, N. Kumar, S.F. Pereira, W.M.J. Coene, H.P. Urbach, 2011, "Performance analysis of coherent optical scatterometry", Appl. Phys. B. 105 775–781. doi:10.1007/s00340-011-4794-7.
[26] J.C. Stover, Society of Photo-optical Instrumentation Engineers, "Optical scattering: measurement and analysis", SPIE Optical Engineering Press, Bellingham, Wash., USA, 1995. http://public.eblib.com/choice/publicfullrecord.aspx?p=728552 (accessed February 6, 2017).
[27] J. Als-Nielsen, D. McMorrow, 2011, "Elements of modern X-ray physics", 2nd ed, Wiley, Hoboken.
[28] D.B. Williams, C.B. Carter, "Transmission Electron Microscopy", Springer US, Boston, MA, 2009. http://link.springer.com/10.1007/978-0-387-76501-3 (accessed December 14, 2016).
[29] J. Garnaes, N. Kofod, A. Kühle, C. Nielsen, K. Dirscherl, L. Blunt, 2003, "Calibration of step heights and roughness measurements with atomic force microscopes", Precis. Eng. 27 91–98. doi:10.1016/S0141-6359(02)00184-8.
[30] E. Agocs, B. Bodermann, S. Burger, G. Dai, J. Endres, P.-E. Hansen, L. Nielson, M.H. Madsen, S. Heidenreich, M. Krumrey, B. Loechel, J. Probst, F. Scholze, V. Soltwisch, M. Wurm, 2015, "Scatterometry reference standards to improve tool matching and traceability in lithographical nanomanufacturing", in: E.M. Campo, E.A. Dobisz, L.A. Eldada (Eds.) pp. 955610. doi:10.1117/12.2190409.
[31] E. Abbe, 1873, "Beiträge zur Theorie des Mikroskops und der mikroskopischen Wahrnehmung", Arch. Für Mikrosk. Anat. 9 413–418.
[32] R. Luebbers, 1984, "Finite conductivity uniform GTD versus knife edge diffraction in prediction of propagation path loss", IEEE Trans. Antennas Propag. 32 70–76. doi:10.1109/TAP.1984.1143189.
[33] J. Garnaes, P.-E. Hansen, N. Agersnap, J. Holm, F. Borsetto, A. Kühle, 2006, "Profiles of a high-aspect-ratio grating determined by spectroscopic scatterometry and atomic-force microscopy", Appl. Opt. 45 3201. doi:10.1364/AO.45.003201.

Chapter 5

Lyot Filter - Extending the spectral range

The most essential part of the imaging scatterometer is the ability to acquire images at different wavelengths. In the presented work, this is done using Lyot filters either before the sample or before the camera. This chapter is divided into two sections. The first section clarifies the theory behind the Lyot filter. The second describes how a custom Lyot filter was fabricated to extend the spectral range of the system.

5.1 Introduction

Birefringent materials are defined as having a varying refractive index depending on the polarization of the light [13]. This means that different polarization states travel through the material at different velocities. The refractive indices is commonly divided into a refractive index for the fast axis, n_{fast}, and a refractive index for the slow axis, n_{slow}. This difference results in a phase change in the two polarizations of the light given by:

$$\delta\phi = \frac{2\pi}{\lambda} \cdot \delta n \cdot d \tag{5.1}$$

where $\delta n = n_{\text{fast}} - n_{\text{slow}}$ and d is the thickness of the material.
It was suggested by Bernard Lyot in 1933 [37] to position a series of linear polarizers and birefringent plates (wave plates) in order to create a frequency filter, later known as a Lyot filter, as shown in figure 5.1.
Using Jones calculus [38], each waveplate and polarizer is considered an optical element so that all polarizers are described by the matrix:

$$P = \begin{bmatrix} 1 & 0 \\ 0 & 0 \end{bmatrix}$$

and the k'th waveplate is described by the matrix L_k:

$$L_k = \begin{bmatrix} \cos(\theta) & \sin(\theta) \\ -\sin(\theta) & \cos(\theta) \end{bmatrix} \begin{bmatrix} e^{i\delta\phi_k} & 0 \\ 0 & 1 \end{bmatrix} \begin{bmatrix} \cos(\theta) & -\sin(\theta) \\ \sin(\theta) & \cos(\theta) \end{bmatrix} =$$

$$\begin{bmatrix} \cos(\theta)^2 e^{i\delta\phi_k} + \sin(\theta)^2 & (1 - e^{i\delta\phi_k})\cos(\theta) \cdot \sin(\theta) \\ (1 - e^{i\delta\phi_k})\cos(\theta) \cdot \sin(\theta) & \cos(\theta)^2 + \sin(\theta)^2 e^{i\delta\phi_k} \end{bmatrix}$$

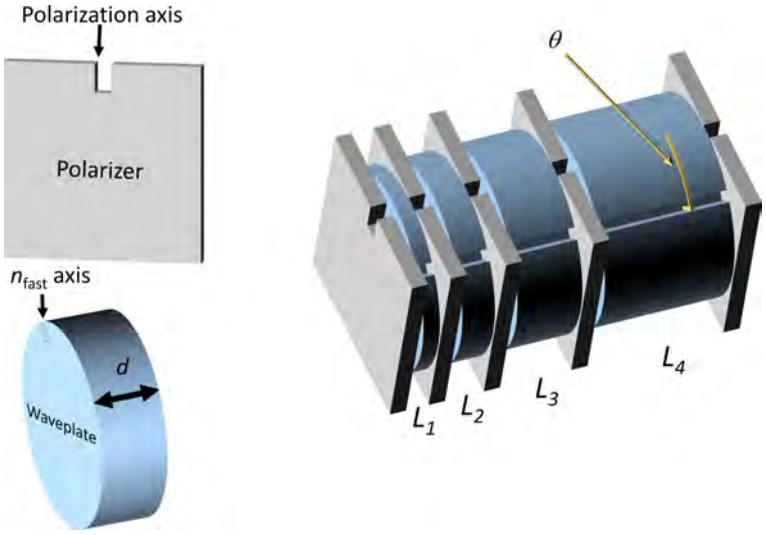

Figure 5.1: (left) Components in the Lyot filter. (Right) A sketch of a Lyot filter constructed from four birefringent plates defining the angle between fast axis and polarization axis.

for an angle of $\theta = \frac{\pi}{2}$, with respect to the polarizers as shown in figure 5.1, L_k simplifies to:

$$L_k = \frac{1}{2}\begin{bmatrix} 1+e^{i\delta\phi_k} & 1-e^{i\delta\phi_k} \\ 1-e^{i\delta\phi_k} & 1+e^{i\delta\phi_k} \end{bmatrix}$$

In a Lyot filter, the thickness of each plate is double that of the previous, so:

$$\delta\phi_k = \frac{2\pi}{\lambda}\cdot\delta n\cdot d_k = \delta\phi_1\cdot 2^{k-1}$$

The series of N plates sandwiched between polarizers is then described as a single optical element given by the matrix:

$$M = PL_1PL_2\ldots PL_{\mathrm{N}}P = \frac{1}{2^{\mathrm{N}}}\begin{bmatrix} (1+e^{i\delta\phi_1})(1+e^{2i\delta\phi_1})\ldots(1+e^{2^{\mathrm{N}-1}i\delta\phi_1}) & 0 \\ 0 & 0 \end{bmatrix}$$

With some algebra, it can be show, that:

$$M_{11} = \frac{e^{\frac{i\delta \mathrm{N}}{2}}}{2^{\mathrm{N}}}\cdot\frac{\sin(2^{\mathrm{N}}\frac{\delta}{2})}{\sin(\frac{\delta}{2})} \tag{5.2}$$

Where, δ is used as shorthand for δ_{ϕ_1} The resulting transmission for the filter is then found as: $T = |M_{11}|^2 = \frac{1}{4^{\mathrm{N}}}\frac{\sin^2(2^{\mathrm{N}}\frac{\delta}{2})}{\sin^2(\frac{\delta}{2})}$ This transmission is plotted in figure 5.2 for a Lyot filter constructed from five SiO_2 birefringent plates of sizes, 1 mm, 2 mm, 4 mm, 8 mm and 16 mm respectively. In theory, this approach should be able to produce bandpass filters with a full width half maximum, FWHM, value smaller than one nanometer.

In the commercial Lyot filter, Varispec CRI-VIS, a liquid cell is inserted as retarder after each plate. This way, δn can be changed by applying a voltage over these cells,

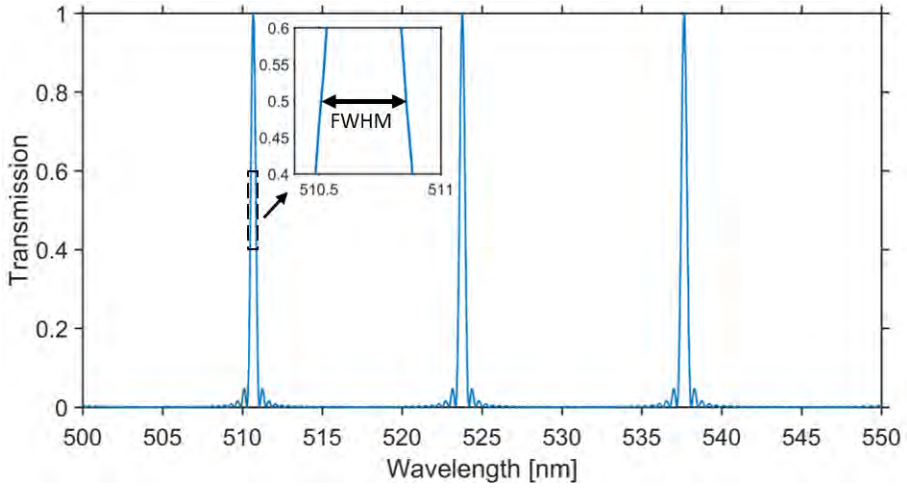

Figure 5.2: Calculated transmission for a Lyot filter with five SiO_2 plates. The first plate have a thickness of 1 mm. Insert shows the FWHM of the first peak.

resulting in a tuneable bandpass filter [39]. This filter is used in the imaging setup. Unfortunately, this filter is shown to have a low transmission outside the wavelength range 450 nm to 690 nm, and a FWHM of slightly above 10 nm [40]. This means that only samples with characteristic diffraction signals in the visible spectrum, would be reliably characterized by the imaging scatterometer. In order to surpass this limit, it is attempted to construct a custom lyot filter as described in the following section.

5.2 Custom Lyot filter

Based on simulations, it was decided to use three birefringent SiO_2 plates with thicknesses 2500 μm , 5000 μm and 10000 μm. However, suppliers were unable to deliver plates with a thickness tolerance below 50 μm. Since this tolerance is large compared to the wavelength of visible light, the thickness of each plate were measured using a confocal microscope (Point thickness mode). The results are tabulated in table 5.1.

Nominal Thickness / μm	**Measured Thickness / μm**	**Ratio**
2500	2522 ± 2	1
5000	5023 ± 2	1.9917
10000	10052 ± 3	3.9857

Table 5.1: Measured thicknesses of the three birefringent plates. The ratio denoted is the ratio between the measured thickness of the given plate and the measured thickness of plate 1.

The plates where ground down in order to achieve an optimal ratio between the plate thicknesses. This was done using a Kemet lapping machine in two steps. The machinery used is sketched in figure 5.3.

First, a suspension containing diamond particles with an average size of 6 μm was poured onto a grinding cloth attached to the rotating lapping steel, spinning at 600

RPM. The sample was attached to the bottom of the weight using double sided foam tape. The weight was gently spun around a displaced axis by hand. After a few minutes, the sample was removed from the lapping steel and cleaned. The thickness was measured using a micrometer screw at four positions along the edges and at the center of the plate. This was repeated until the thickness was near the desired value.

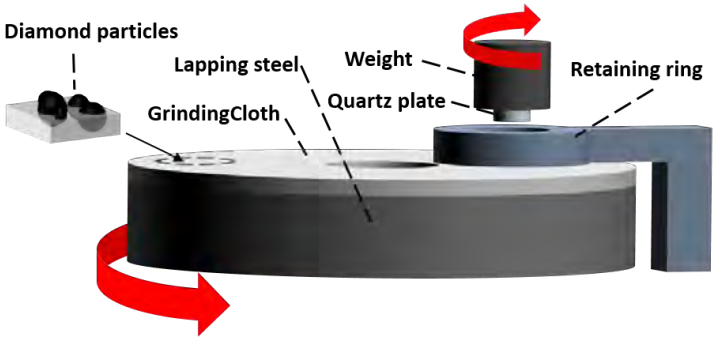

Figure 5.3: Sketch of the setup used for the initial grinding of the waveplates. The lapping steel and the weight are rotated around displaced and in opposite directions to avoid systematic grinding traces.

Secondly, the above steps where repeated using a suspension containing diamond particles with an average size of 3 μm. This way the plates achieved the following thicknesses:
2501 ± 3 μm, 5000 ± 3 μm, 10000 ± 6 μm.
This grinding did, however, end up introducing scratches on the plates. In an attempt to remove these scratches, the samples were polished using a cerium oxide suspension. This was done at DFM using a spin coater in place of the lapping machinery.

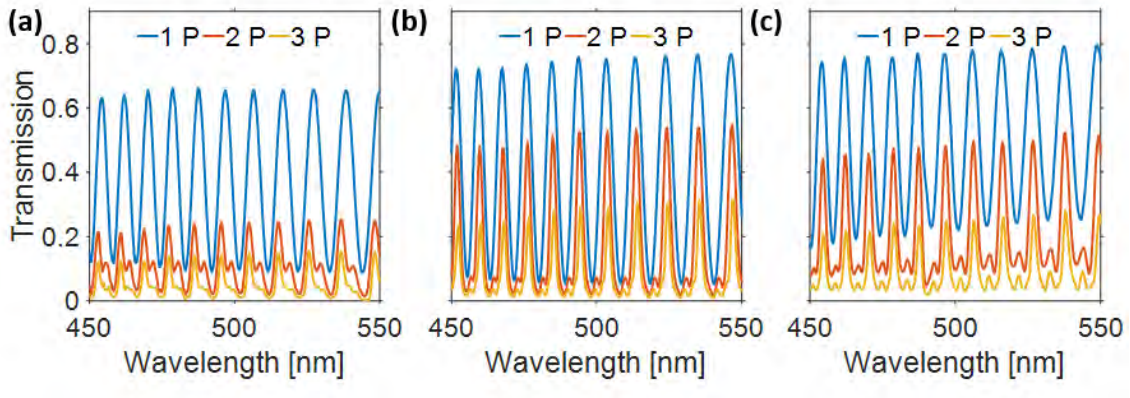

Figure 5.4: Transmission of the custom lyot filter from 450 to 550 nm for a configuration with 1 plate (blue line), 2 plates (red line) and 3 plates (yellow line). (a) before grinding of the plates, (b) after grinding of the plates and (c) after grinding and polishing.

Plots of the measured transmission for different filter configurations, at different processing steps, can be seen in figure 5.4. We see a clear improvement of the transmission when the filters are ground. Comparing figure 5.4-(b) and 5.4-(c), we

see that we get a slightly lower transmission after the polishing step. This hints that this step might induce more surface damage than it repairs, and was therefore stopped. In the end it was decided to use a filter build from the two smallest plates. The plates and polarizers are mounted in an optical cage system, forming a Lyot filter. A photo of the Lyot filter can be seen in figure 5.5.

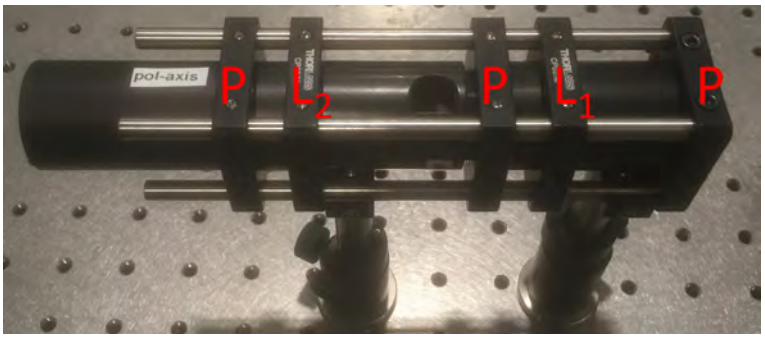

Figure 5.5: Photo of the custom Lyot filter, showing the birefringent plates, L_1 and L_2 and the polarizers , P.

The Lyot filter is then combined with regular color filters in order to select different peaks. The transmission spectrum of the color filters can be seen in figure 5.6(a) and the combined transmission can be seen in figure 5.6(b). Peaks with a FWHM of a few nanometers (ranging from 2 nm to 8 nm for the different peaks) are obtained, and thereby we extend the measurement range from 450 nm - 690 nm, to 422 nm - 920 nm (not counting the last peak at 950 nm). Furthermore, we see that the transmission from most peaks exceed the 4-9% obtained from the tuneable filter. The produced filter is tested in the following section and used to perform measurements on nanowires, as demonstrated in Chapter 9.

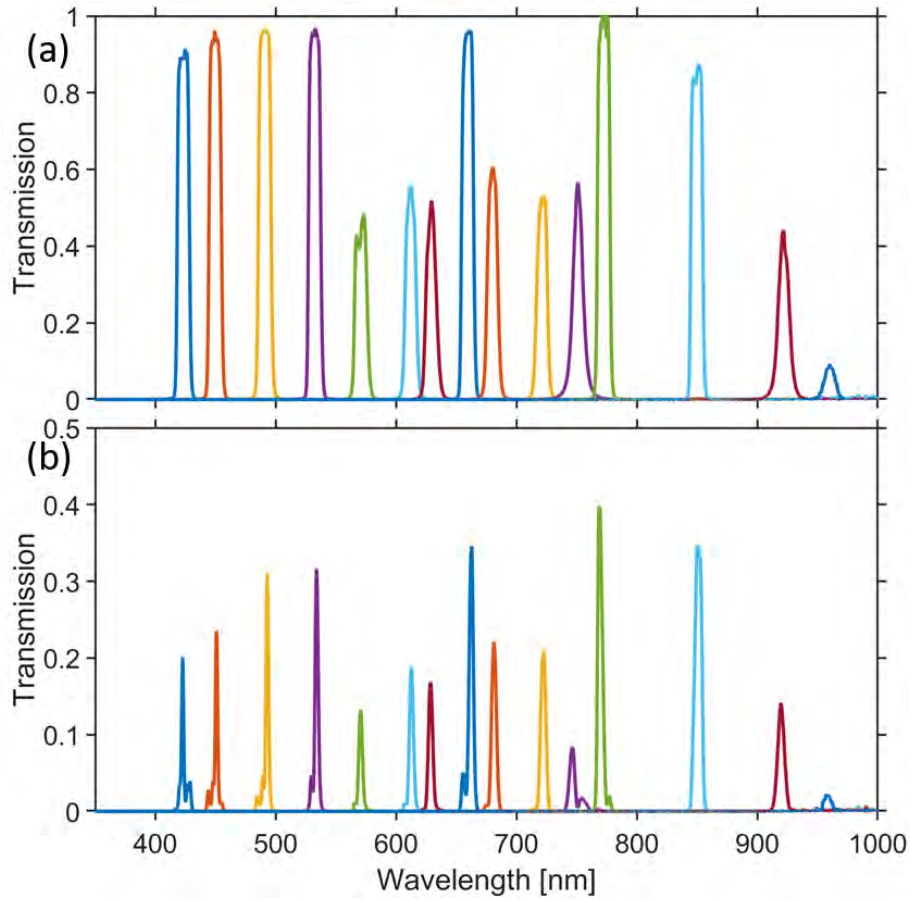

Figure 5.6: Transmission spectra of (a) color filters used to select lyot peaks, and (b) combinations of lyot and color filters.

5.2.1 Testing of Lyot filter

First, the optical profile of the filter is measured. Due to imperfections in the Lyot filter, the transmitted light is not perfectly monochromatic, but has some "bumps" in the optical profile, as seen in figure 5.7.
To take this into account in the simulations, the optical profile of each of the filters in the filterwheel is measured together with the Lyot filter and fitted with a sum of three Gaussian functions. An example of such a fit is seen in figure 5.8. The center peak and volume of each Gaussian is used to calculate the diffraction efficiency, $\eta^C(\lambda)$.

$$\eta^C(\lambda) = \frac{\eta^C(\lambda_1) \cdot V_1 + \eta^C(\lambda_2) \cdot V_2 + \eta^C(\lambda_3) \cdot V_3}{V_1 + V_2 + V_3} \tag{5.3}$$

where λ_i and V_i are the center wavelength and the volume of the i'th Gaussian, respectively.

To test the system, a scatterometry measurement was performed on a well known sample, also measured in ref. [41]. The targeted grating, etched on a Si100 substrate, has a period of 1000 nm and is measured at an angle of incidence of 50 degrees. The

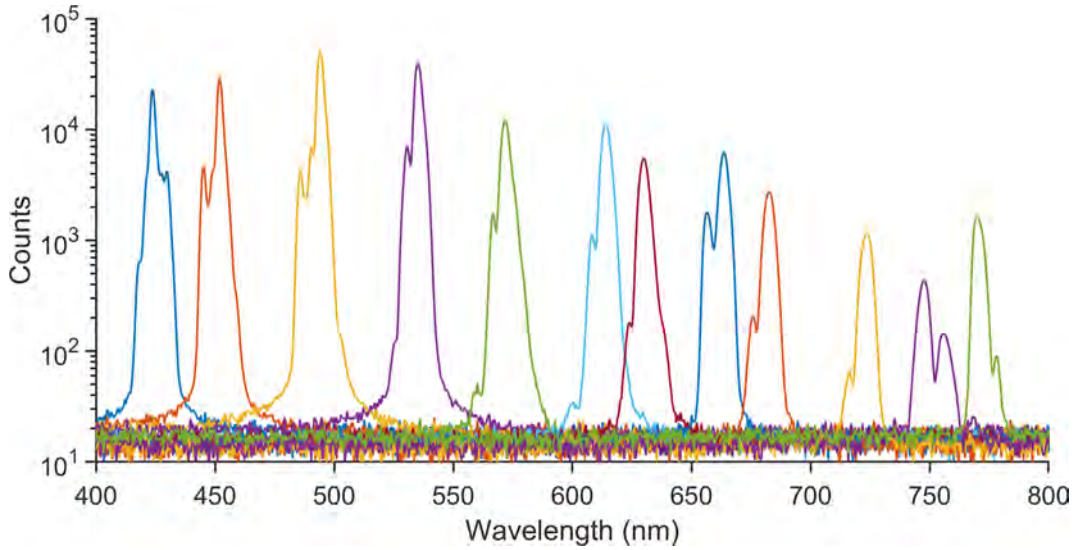

Figure 5.7: Optical profiles of the light after the Lyot filter used in combination with different bandpass filters. None of the profiles are well described by a single Gaussian.

measured data and the best fitting model can be seen in figure 5.9. The sidewall angle has been neglected based on the results in the literature [41]. The reconstructed parameters are in excellent agreement with the reported values in literature [41]. Based on this, it is concluded that the filter works as intended. The filter will be revisited in Chapter 9, where the filter will be used to perform imaging scatterometry on nanowires.

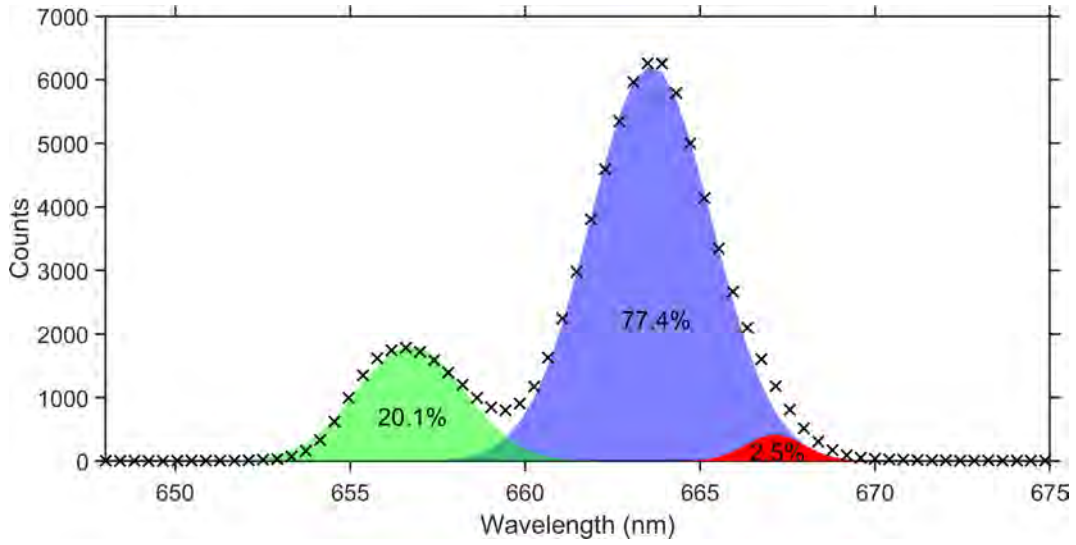

Figure 5.8: Profile of the transmitted light for one of the band pass filters and Lyot filter. Black crosses show a straight through measurement with a dark measurement subtracted. The colored areas show the gaussians used to fit the profile, and the numbers inside the gaussians represent their volume relative to the sum of all volumes.

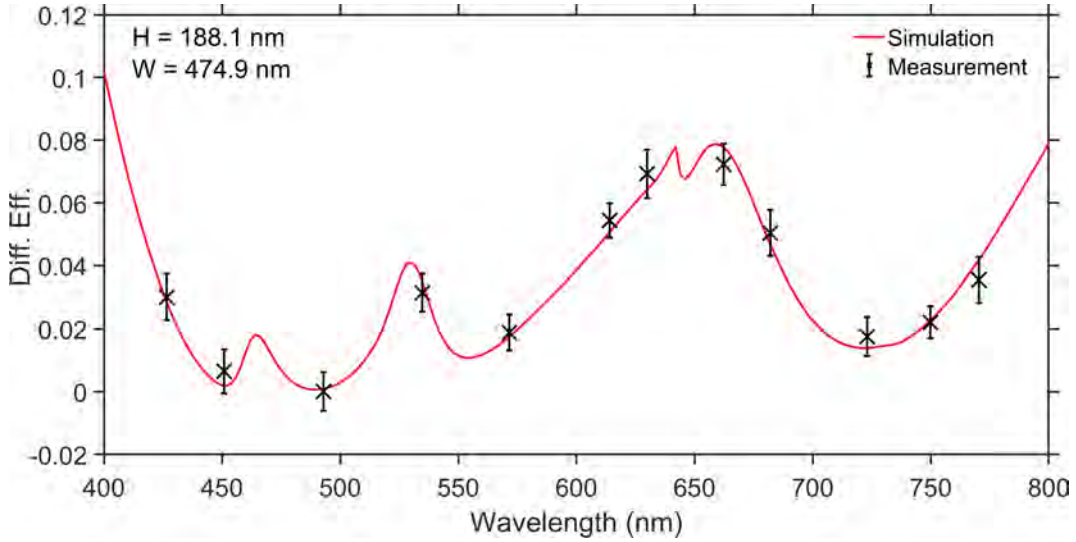

Figure 5.9: Scattermetry measurement on 1D lines in Si100. Measured diffraction efficiencies (black crosses) and simulated diffraction efficiencies (red line). The model parameters for the best fitting model can be seen in the upper left corner.

Chapter 6

Injection Molding

Various products with functionalities obtained from embedded nanostructures are becoming increasingly available in the semiconductor industry. It has been suggested to adopt these functionalities in the plastic industry [42, 43]. Even though high-end manufactures have achieved good results producing the needed nanostructures, fast and reliable metrology for the characterization of structures is still a challenge.
One of the most common fabrication techniques in the plastic industry is injection molding [44].

This chapter introduces the injection molding technique and discusses common defects on injection molded nanostructures. The chapter continues to describe the compact scatterometer developed to characterize the injection molded nanostructures at the fabrication line. Preprints of Paper 2 and Paper 3 are attached at the end of this chapter.

6.1 Injection Molding

In injection molding a master sample is used to mass-produce replicas. The master is called a shim and usually consists of nickel, steel or silicon. While the replicated part is produced in a softer material i.e. plastic.

An injection molding machine consists of three main parts: An injection unit, a mold cavity and a clamping unit [45]. The process is sketched on figure 6.1. Polymer pellets are feed into a hopper, and a screw is used to move the pellets through the injection unit. The polymer is melted by heating bands surrounding the screw and by the time the polymer reaches the end of the screw, it is entirely molten. Once enough plastic is in front of the screw, the screw acts like a plunger of a syringe and injects a fixed volume of plastic into the mold cavity. Inside the mold cavity, the plastic cools down and solidifies, thus replicating the surface structure of the insert. When the part is perfectly solidified the cavity opens, the part is ejected from the cavity, and the cycle starts over.

If the injection molding process is successful, the produced part should correspond to the inverse structure of the shim. This is however not always the case. A couple of scenarios for different insert temperatures are shown in figure 6.2. Here we clearly see a large temperature dependence of the final part. The defect types seen in

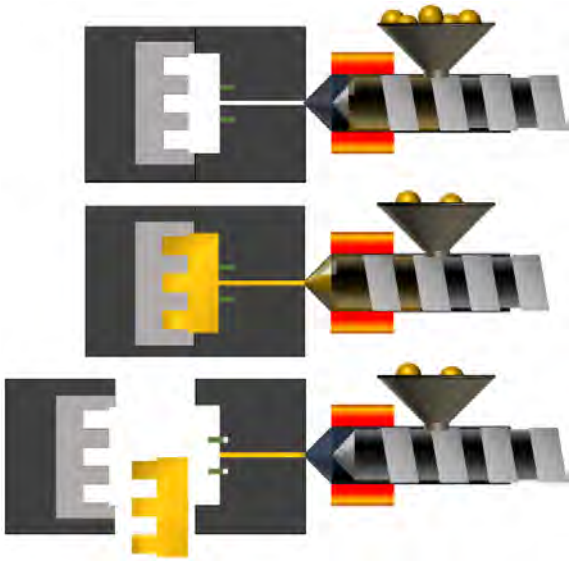

Figure 6.1: Sketch of the injection molding process. (top) Polymer pellets are feed to a hopper and melted while transported through the injection unit by a screw. (middle) Once enough molten polymer is in front of the screw, the screw plunges forward and forces the plastic into the cavity. In the cavity, the polymer hardens and replicates the structures on the insert in the cavity. (bottom) After a part has been formed, the cavity opens and the part is ejected.

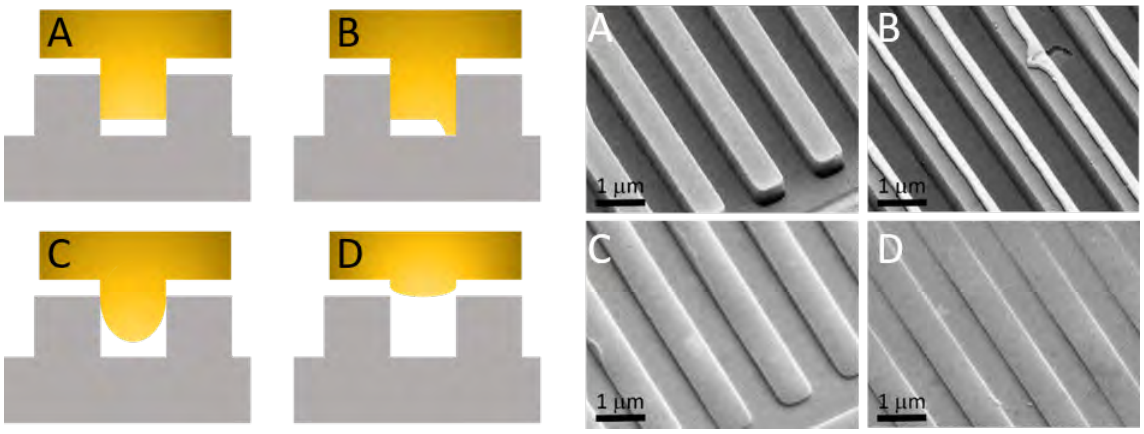

Figure 6.2: (left) side view sketch of the plastic part (gold) and the shim (grey) for different defect types as the cavity opens and (right) corresponding SEM images. The samples were molded at different cavity temperatures, while other fabrication parameters were kept identical. (A) Example of a good replication. (B) Here the part is pulled out before the polymer is fully solidified and one ends sticks to the shim. (C) The polymer solidifies too fast, and the corners of the trenches are not filled. This results in rounding of the sharp corners. (D) A more extreme case of (C) where the polymer barely enters the trenches and, as a consequence, a lower height is replicated. The tilt angle is 30° for all SEM images.

figure 6.2(C) and (D) can be approximated by adding a corner rounding in the simulated structure as previously discussed. The defect type seen in figure 6.2(B) can be hard to optically distinguish from a rectangular structure, since the volume of the excess material is typically low compared to the grating material. It is however attempted to approximate the line as another grating on top of the intentionally fabricated grating, as illustrated in figure 6.3. When attempting to characterize the

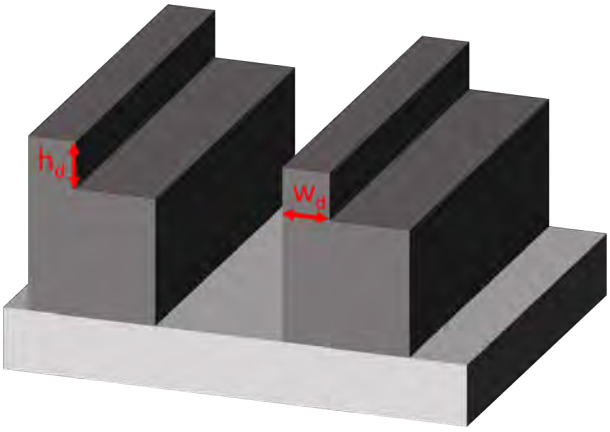

Figure 6.3: Illustration of how the defect is approximated as a slab in the RCWA simulations. Only the height and width of the defect, h_d and w_d, are varied in the simulations.

upper lines, we lock the parameters of the bottom lines to the parameters for a perfect replication ($h = 630$ nm and $w = 700$ nm). The goodness of the fit as a function of the parameters describing the line can be seen in figure 6.4. We see that we actually find a better solution by adding the line on top. The best solution have a height between 10 nm and 20 nm and a width between 170 and 300 nm, however a defect line with a width of 700 nm and a low height, would fit almost equally well. The later corresponds to the simple model, with a few nanometers added to the height. Hence this effect would be hard to find without already knowing the parameters of the perfect grating.

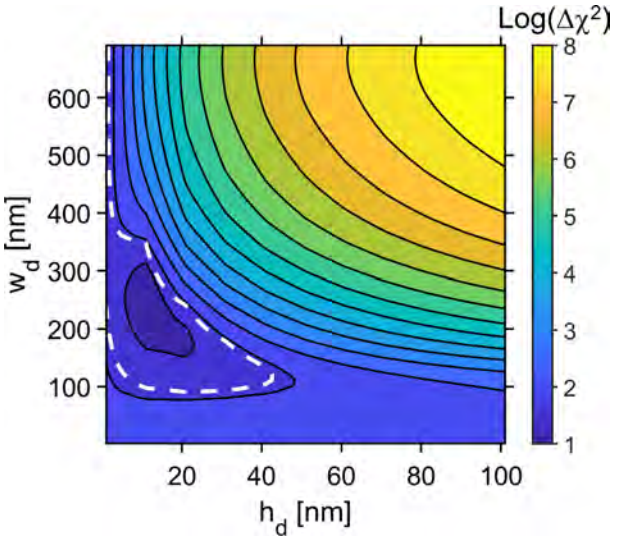

Figure 6.4: Goodness of fit as a function of the height and width of the defect introduced. The best fitting model has a defect line with a width around 200 nm and a height below 20 nm.

The same analysis is performed on a sample without the mentioned defect, and the result can be seen in figure 6.5. We can see that the preferred model is one with a low volume of the added line. This result suggests that we can distinguish samples with a top defect and no defect, assuming that the underlying grating is well replicated. Based on this, it is obvious to see if the semi analytical model introduced in Paper 4

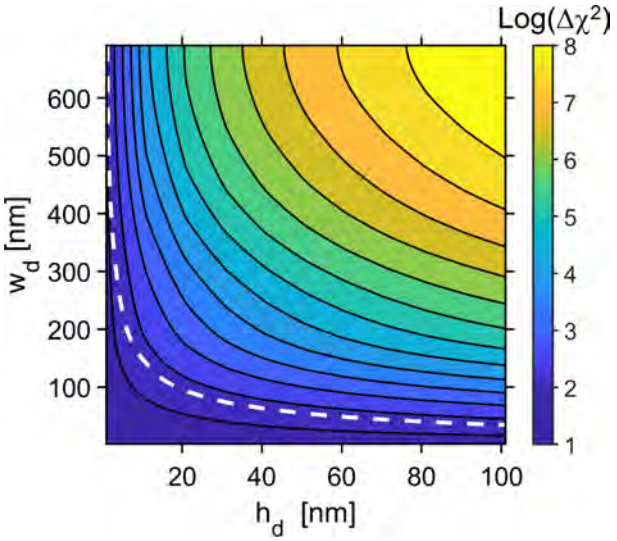

Figure 6.5: Goodness of fit as a function of the height and width of the defect introduced using a sample with no defect. The best fitting model has no defects goodness of fit decrease as the volume of the defect line increases.

can be used to characterize this defect. To investigate this, the data from the sample with an edge defect, previously investigated, is used with the semi-analytical model:

$$\eta^c_{SA}(\lambda,\sigma) = \eta^c_{Grat}(\lambda)\cdot\exp\Big(-\big(4\pi\frac{\cos(\theta_i)\cdot\sigma}{\lambda}\big)^2\Big)$$

Where the super-script c denotes calculated values and σ denotes the Root-Mean-Sqaure value of the defect profile over a period, Δ as:

$$\sigma = \sqrt{\frac{1}{\Delta}\int_0^\Delta f(x)^2 dx}$$

A σ-value is found by optimizing:

$$\chi^2 = \frac{1}{N}\sum_{i=1}^{N}\Big(\frac{\eta(\lambda_i)-\eta^c_{SA}(\lambda_i,\sigma)}{\delta\eta(\lambda_i)}\Big)^2$$

Here $\eta^c_{Grat}(\lambda)$ is kept constant, while σ is varied. In the left part of figure 6.6. We can see, that the semi-analytical model finds a best solution at $\sigma = 12$ nm. Since an analytical expression for σ can be written as:

$$\sigma = \sqrt{\frac{\mathrm{h_d^2}\cdot\mathrm{w_d}}{\Delta}}.$$

This value of 12 nm corresponds to several permutations of $\mathrm{h_d}$ and $\mathrm{w_d}$ as shown in the right part of figure 6.6. We cannot directly characterize the geometry of the defect, but it is evident that it is present. The found possible parameters of the defect are not too far from the ones found in figure 6.4 using RCWA and thus showing the strength of the semi-analytical model.
In Paper 2 and Paper 3 it is shown that the other defect types (Resulting in a lower height and rounded corners) can easily be identified from the optical signal.

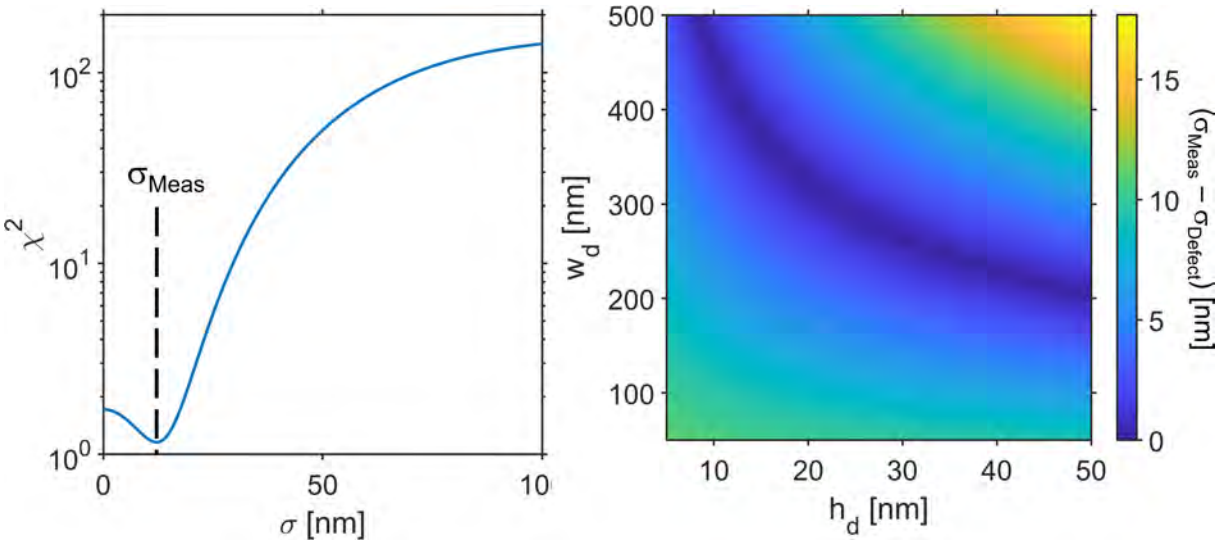

Figure 6.6: (left) χ^2 as a function of σ used in the semi-analytical model. (right) Difference between measured σ and σ introduced by the defect as a function of the defect parameters.

6.2 Compact Scatterometer

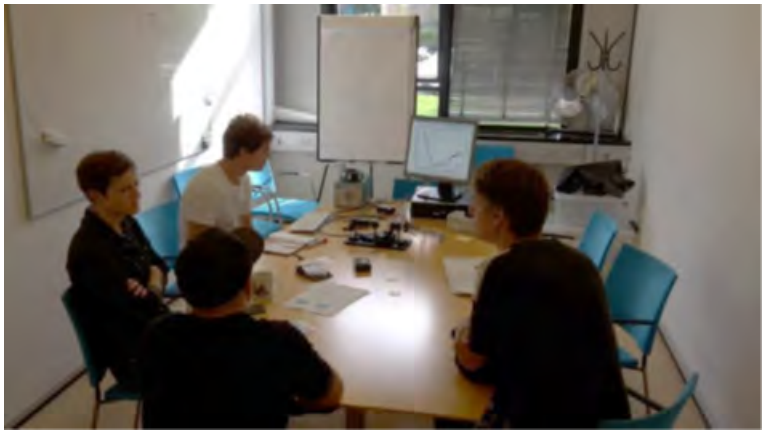

Figure 6.7: Photo of the very first demonstration of the compact scatterometer at NIL Technology.

NIL Technology A/S is a company specializing in nanopatterning and nanoimprint lithography. They produce shims of high quality, specialized for injection molding of nanostructures. In a collaboration with NIL Technology, we have demonstrated a method to characterize the produced parts in real time, using a compact scatterometer which can be transported to a production site. A photo of the very first demonstration of the prototype can be seen on figure 6.7, and some typical results are shown on figure 6.8. Based on these promising results, it was decided to schedule the first field test at DanChip. By performing running tests of the instrument together with industrial partners, it was ensured that the final instrument would be useful in a production environment. Paper 2 is based on the work carried out with NIL Technology in the eurostar project: SuperLens, and the EMPIR project: MetHPM.

The compact scatterometer is shown in figure 6.9. A Tungsten-Halogen light source

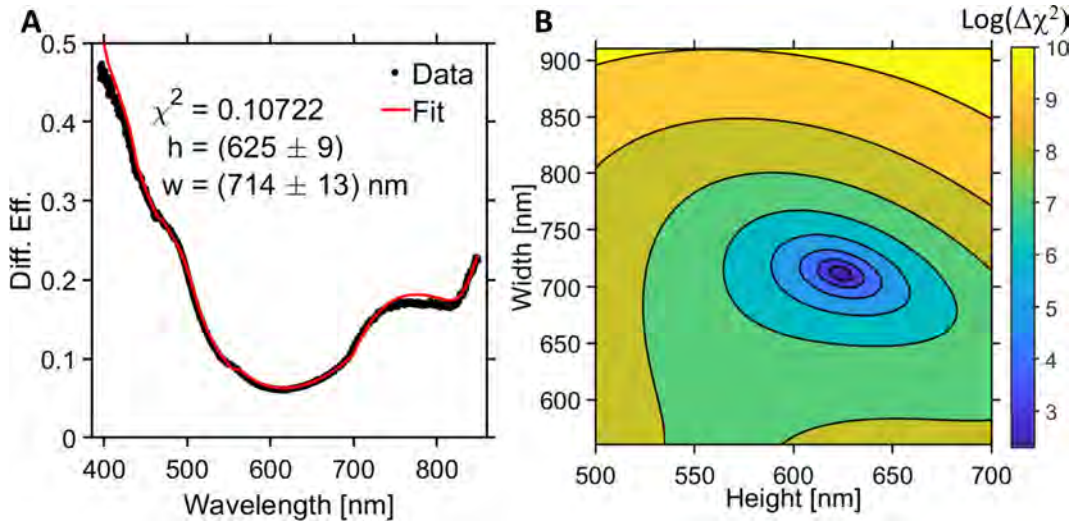

Figure 6.8: results from the demonstration at NIL Technology. (A) measured diffraction efficiencies and the best fitting model. The found χ^2 and estimated height and width are displayed. (B) $\Delta\chi^2$ as a function of the model parameters.

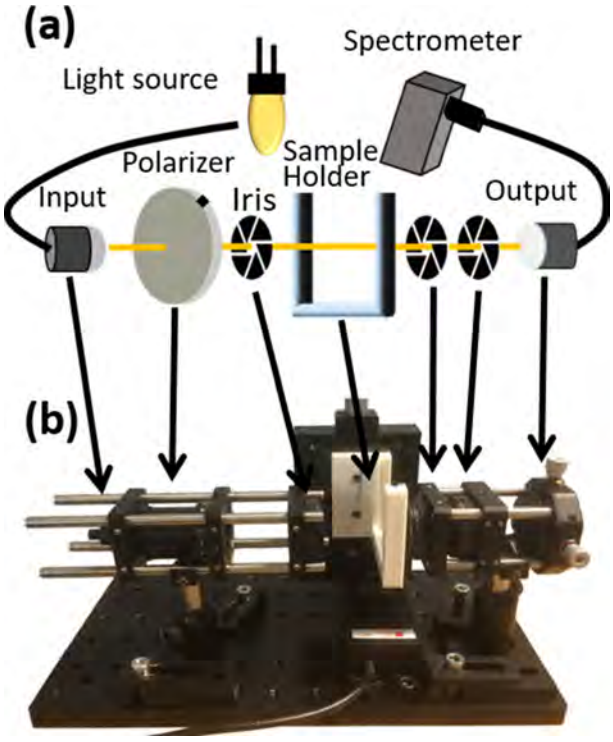

Figure 6.9: (a) sketch and (b) image og the components in the compact scatterometer. The figure is reprinted from Paper 2.

from Thorlabs was chosen due to a high intensity in the visible spectrum and compactness of the source. The source was found to have a stable intensity after a one hour warm up period (under 0.5 % drift over a 24 hour period in a temperature controlled room).
The spectrometer used was a USB-2000 series from ocean optics. The spectrometer was calibrated by using a Krypton source with known spectral lines. The spectrometer allows for acquisition times down to 3 ms, which was the limiting factor in the acquisition time for a single intensity measurement.
A Glan-Laser polarizing cube, coated for an optimal transmission of visible light, was used to control the polarization of the light impinging on the sample. The polarizer was mounted in a rotational stage, making it possible to change the polarization states of the light. This was done, so that we could measure the same area with different polarizations to increase the amount of spectral features in cases of an ambiguous sample reconstruction.
The sample holder was designed in The software Cubify Invent and 3D printed using a CubePro Duo 3D printer.

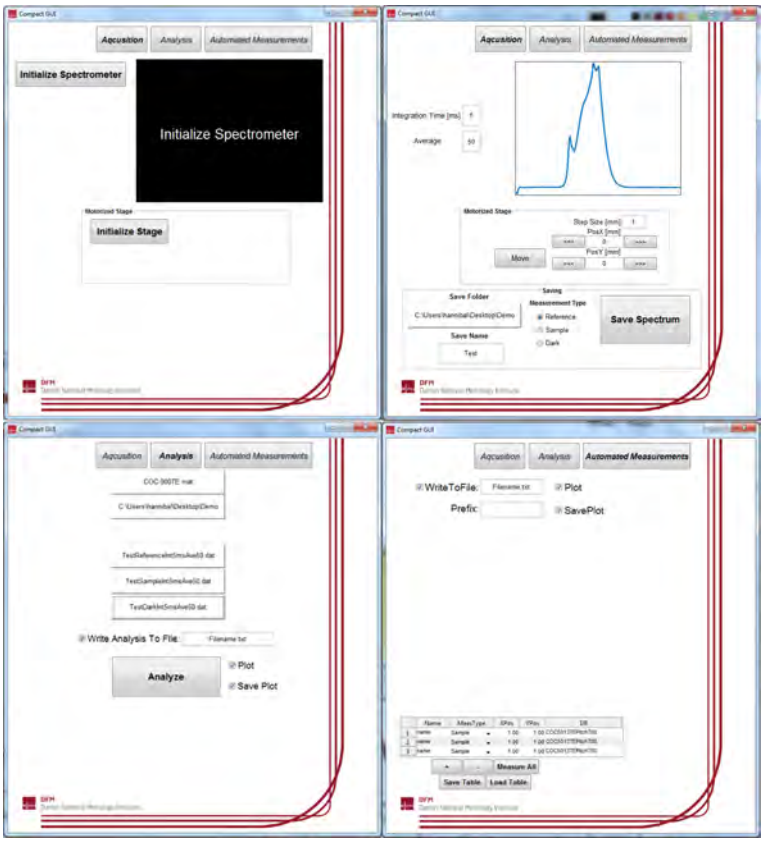

Figure 6.10: Screenshots from the different GUI modules. Initial screen (top left), Aqcusition panel after Initialization, Analysis panel (bottom left) and Automated Measurements panel (bottom right). The panels are navigated through using the buttoms at the top of each panel.

A Graphical User Interface was developed, to make the operation of the scatterometer as user friendly as possible. The GUI is divided into three modules: An acquisition module, where one can acquire data and tweak parameters associated with the measurements (integration time, number of spectras to average and measurement type) as well as translating the sample. An analysis module, where one can perform scatterometry analyses on the data acquired based on a specified database of simulated structures. Lastly, an automation module, where one can either create or load a recipe for how the measurements should be acquired and analyzed. The last module makes it possible for an operator to perform an analysis with a single click for each sample to be measured, making it very easy to use and simple to automate in the future. The data shown in Paper 2 was acquired in this way by different operators at the site. Screenshots of the GUI can be seen in figure 6.10.

In Paper 2, the influence of the shim temperature was investigated for two polymers Topas-5013 and Topas-8007. This work was carried out at DanChip using the compact scatterometer placed right next to the injection molding machine. A photo from the session can be seen in figure 6.11.
Since the scatterometer could characterize the nanostructures on the parts much faster than the injection molding machine could produce them, it was possible to measure on each produced sample without creating a bottleneck, and thereby enabling real-time feedback to the operator.

In Paper 3, the compact scatterometer was deployed at a production facility in Germany together with Poly Optics GmbH, Kleve . Poly Optics produces injection molded plastic lenses, but had no experience with injection molding nanostructures. The scatterometer was used to give feedback to the operator, making it possible to create and iteratively improve the injection molding recipe. Furthermore, the spatial variation on the sample was investigated by measuring six fields at different sample positions with the compact scatterometer, and by using an imaging scatterometer build in a transmission configuration.

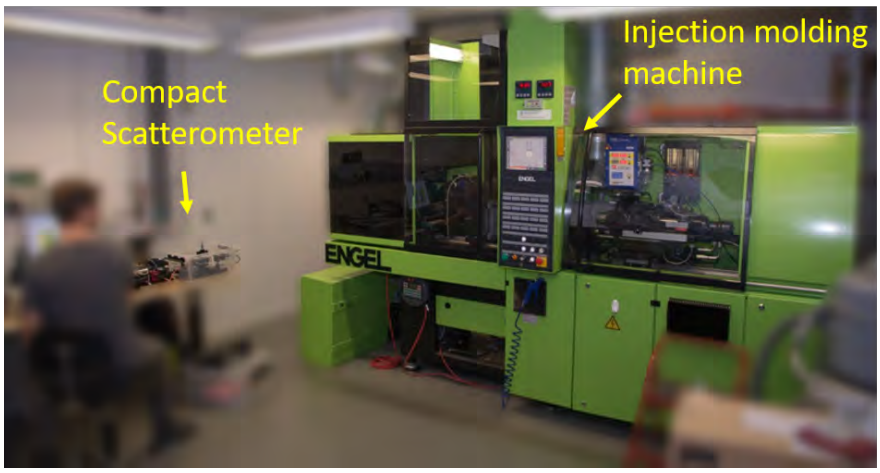

Figure 6.11: Photo from the production and characterization session showing the compact scatterometer and the injection molding unit.

Preprint of paper 2

Title:

In-line characterization of nanostructured mass-produced polymer components using scatterometry

Journal:

Journal of Micromechanics and Microengineering, vol. 27 (2017)

Authors:

J. S. Madsen, L. H. Thamdrup, I. Czolkos, P. E. Hansen, A. Johansson, J. Garnaes, J. Nygård and M.H. Madsen

DOI of published paper:

10.1088/1361-6439/aa7a3a

In-line characterization of nanostructured mass-produced polymer components using scatterometry

Abstract

Scatterometry is used as an in-line metrology solution for injection molded nanostructures to evaluate the pattern replication fidelity. The method is used to give direct feedback to an operator when testing new molding parameters and for continuous quality control. A compact scatterometer has been build and tested at a fabrication facility. The scatterometry measurements, including data analysis and handling of the samples, are much faster than the injection molding cycle time, and thus, characterization does not slow down the production rate. Fabrication and characterization of 160 plastic parts with line gratings are presented here, and the optimal molding temperatures for replication of nanostructures are found for two polymers. Scatterometry results are compared to state of the art metrology solutions: Atomic force- and scanning electron microscopy. It is demonstrated that the scatterometer can determine the structural parameters of the samples with an accuracy of a few nanometers in less than a second, thereby enabling in-line characterization.

1. Introduction

Polymer consumer products with nano- or micro structures can obtain new functionalities which enable them to gradually change color as the viewing angle or the illumination angle changes (iridescence) [1] or have surfaces which repel water (hydrophobicity) [2]. Current research within iridescence is focused on replacing chemical dyes with structural colors and thereby aims to reduce the impact on the environment during production and recycling [3,4]. It has been suggested to produce nano-textured plastic surfaces using *e.g.* injection molding [5].

Injection molding is a mass production technique where a product is replicated from a master structure by injecting molten polymer into a cavity, where it solidifies [6]. The technology is one of the most exploited processes in the plastic industry [7], capable of reproducing structures down to the nanoscale [8,9]. Typical cycle times for injection-molding nanostructures are a few minutes [10]. The added functionality depends highly on the quality of the replicated structures, making a high degree of replication fidelity important. However, high throughput is a challenge for monitoring of the fabricated parts, which means that suitably fast techniques for quality control of the fabricated structures by in-line characterization are needed [11]. In

addition, the injection molding process has an abundance of tunable parameters, making it tedious to optimize a recipe for a given fabricated component using common characterization techniques.

State of the art characterization techniques include atomic force microscopy (AFM) and scanning electron microscopy (SEM) [12]. Both techniques have a high resolution, but are time consuming, expensive and very sensitive to vibrations of the sample [13]. In addition, AFM is limited by a small field of view [14] and SEM requires the sample to be placed in a vacuum chamber [15]. These drawbacks make the techniques unsuitable for integration into a production line.

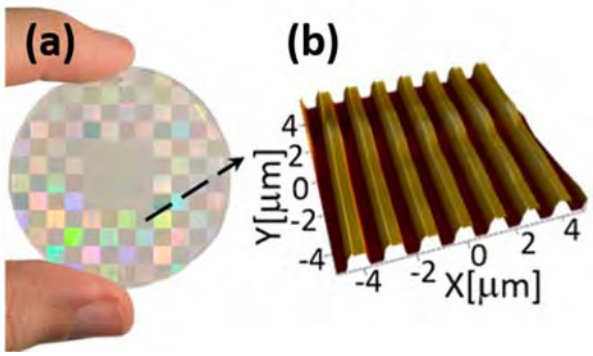

Figure 1. Fabricated and characterized samples. (a) Photograph of a plastic part. (b) 3D AFM image of the area marked by the arrow in (a). The nanostructures are line gratings with periods ranging from 700 nm to 1400 nm. Each grating field is aligned perpendicularly to adjacent grating fields. The colorful sample purely obtains its iridescence from the nanotextured surface.

Since structural coloring is an optical effect, it is intuitive to use an optical characterization technique. Scatterometry is a promising optical technique for in-line characterization since it is fast and robust [16]. In scatterometry, the information obtained from the light diffracted by the sample is used to reconstruct the sample using an inverse modeling approach [17]. In order to reduce the computation time, a library search method can be used [18], which is ideal for in-line characterization. Here prior knowledge of the fabricated structures is used to generate a database of theoretical diffraction signals, and the closest match to the experimental data is used to determine the morphological parameters of the sample. Scatterometry is already used in the semi-conductor industry for characterization of high-end devices [19,20]. Due to polymers having a higher transmission than reflection in the visible spectrum, it is ideal to use a transmission configuration rather than the reflection configuration commonly used for semiconductors.

A portable and compact scatterometer has been constructed and tested on-site next to an injection molding machine. We have characterized over 150 molded parts with nano-textures to provide the operator with

direct feed-back on the quality of the pattern replication. This has been used for fast optimization of the injection moulding parameters.

2. Methods

Plastic parts with nanostructures were fabricated using injection molding under varying conditions. Analysis of the consequential changes in the parts' nanostructures requires a high-throughput metrology method to determine the optimal molding parameters. All samples were characterized using spectroscopic scatterometry [19].

2.1 Spectroscopic Scatterometry

Spectroscopic scatterometry is based on an inverse modeling approach which reconstructs the sample topology. For the inverse modeling, experimentally measured wavelength dependent diffraction efficiencies, $\eta(\lambda)$, are compared to simulated diffraction efficiencies. The experimentally measured diffraction efficiencies are defined as the intensity of undiffracted transmitted light relative to the intensity of the incoming light [21]. In order to determine the diffraction efficiencies, three wavelength-dependent intensity measurements are needed. A measurement on the area with grating structures, $I_{\mathrm{sample}}(\lambda)$, a reference measurement, $I_{\mathrm{ref}}(\lambda)$, performed on an area without grating structures, and a dark measurement with the light source turned off, $I_{\mathrm{dark}}(\lambda)$. The dark measurement is used to correct for detector response and stray light. The diffraction efficiencies are then found according to ref. [17]:

$$\eta(\lambda) = \frac{I_{\mathrm{sample}}(\lambda) - I_{\mathrm{dark}}(\lambda)}{I_{\mathrm{ref}}(\lambda) - I_{\mathrm{dark}}(\lambda)} \tag{1}$$

The simulations for the inverse modeling are based on rigorous coupled wave analysis (RCWA) where the grating is divided into rectangular slabs [22]. In this study, seven slabs have been used and the Fourier components have been truncated to 19. A set of model parameters, $\boldsymbol{\alpha}$, describing the sample, and a set of system parameters, $\boldsymbol{\Omega}$, describing the measurement conditions, are used to simulate the diffraction efficiencies, $f(\boldsymbol{\Omega}, \boldsymbol{\alpha})$. In this study, it is found that the nanostructures can be described by their period, □, their height, *h*, their width, *w*, and the radius of the top corner rounding, *r*. Additional parameters, including sidewall angles and rounding of the bottom corner have also been investigated. These parameters where found to have a high cross correlation with the other parameters, and were therefore not examined further. If one requires information about more parameters, one could move to phase sensitive techniques, like ellipsometry, at the cost of more complicated instrumentation [23]. The measurement conditions taken into

account are the wavelength of the light, λ, and the polarization of the light, *P*. The angle of incidence is assumed to be normal to the surface for all simulations. We thus have $\boldsymbol{\alpha}(\Gamma, h, w, r)$ and b$\boldsymbol{\Omega}(\lambda, P)$, these parameters are sketched in Figure 2.

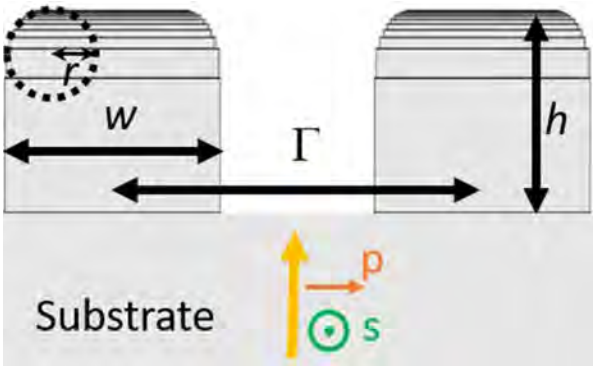

Figure 2. Sketch of the model parameters used for the simulations of the diffraction efficiency. The light travels through the substrate with a polarization either aligned parallel (s-polarization) or perpendicular (p-polarization) to the grating lines. The used grating parameters are period (Γ), height (*h*), width (*w*) and rounding of the upper corner (*r*).

A library is build, containing diffraction efficiencies simulated for a range of the values Γ, *h*, *w* and *r* contained in $\boldsymbol{\alpha}$. The measured diffraction efficiencies were then compared to all simulated diffraction efficiencies in the library using chi-square optimization given by:

$$\chi^2 = \frac{1}{N}\sum_{i=1}^{N}\left(\frac{\eta(\lambda_i) - f(\boldsymbol{\Omega_i}, \boldsymbol{\alpha})}{\delta\eta(\lambda_i)}\right)^2 \quad (2)$$

Where N is the number of wavelengths simulated, $\eta(\lambda_i)$ is the measured diffraction efficiency of the i'th wavelength, $f(\boldsymbol{\Omega_i}, \boldsymbol{\alpha})$ contains all simulated diffraction efficiencies for the i'th wavelength and $\delta\eta(\lambda_i)$ is the error from the measured diffraction efficiency of the i'th wavelength. The simulated model resulting in the lowest χ^2-value is assumed to best describe the topology of the actual physical sample. The confidence limits for the estimated model parameters are found statistically using constant chi-square boundaries [17].

2.2 Injection molding

A 20-ton injection moulder (Engel, Victory Tech 80/45) was fitted with a nickel shim (Ø 85 mm) with nanostructures on the surface for fabrication of nano-textured components. The process is governed by a vast amount of parameters, mainly related to pressure, temperature and time. These parameters may all affect the replication quality on the final product [23,24]. In this study, only the most influential parameters

(mold temperature and demolding temperature [25,26]) were varied. Polymer pellets were fed into a hopper, pre-dried and heated while transported through the injection cylinder. The polymers used were Topas 5013L-10 and Topas 8007S-04 (both from Topas Advanced Polymers GmbH, Germany). Once molten, the polymer was injected into the cavity where it cooled off and solidified under pressure, thereby replicating the nanostructures on the shim. For Topas 5013L-10, a cooling time of 20 s, independent of the molding temperature, and a holding pressure of 1134 bar were used, while for Topas 8007S-04, the cooling time was varied and the holding pressure was 1500 bar. For both polymers, a shot volume of 11 cm^3 and a tool clamping force of 450 kN were applied. Lastly, the clamping unit opened the cavity and the part was ejected before the next cycle started. The studied parts were fabricated over two days with cycle times varying from one to three minutes depending on the machine settings.

2.3 Shim fabrication

Fabrication of the nickel shim involves multiple steps which are briefly described here, and more details can be found in Ref. [5]. First, a silicon wafer was patterned using deep ultraviolet (DUV) lithography. Multiple line gratings with a period from 700 nm to 1400 nm were fabricated on a single shim. Each grating area was 4 mm x 4 mm and the width of the lines equaled half the period. The substrate was etched using dry reactive ion etching. Subsequently, seed layer deposition (NiV) and electroplating were conducted in order to form a 300 µm thick Ni layer. After electroplating, the Si wafer was etched away in KOH and the Ni shim was laser cut in the right shape for the molding tool. An AFM and an SEM image of the shim are shown in Figure 3.

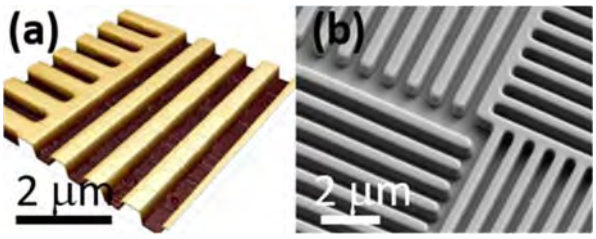

Figure 3. (a) AFM image (feature depth 633 nm), and (b) SEM image (tilt angle 30°) of the shim used for injection molding.

3. Scatterometer setup

Figure 4 shows a schematic of the setup. The light from a fiber-coupled Tungsten-Halogen light source (Thorlabs, SLS201L) is coupled to free space and polarized by a Glan-Laser (Thorlabs, GL10-A) linear polarizer crystal before impinging on the backside of the sample. The undiffracted part of the transmitted light is coupled to another fiber and guided to a spectrometer (Ocean Optics, USB-2000). The sample holder is placed on an XY-stage, making it possible to translate the sample in the grating plane. Irises are placed before the sample to control the illuminated area on the sample, and after the sample to control the area, from which the light is collected. For the measurements, light was collected from an area of roughly 1 × 1 mm^2 and consequently, the measured signal is an average from this area.

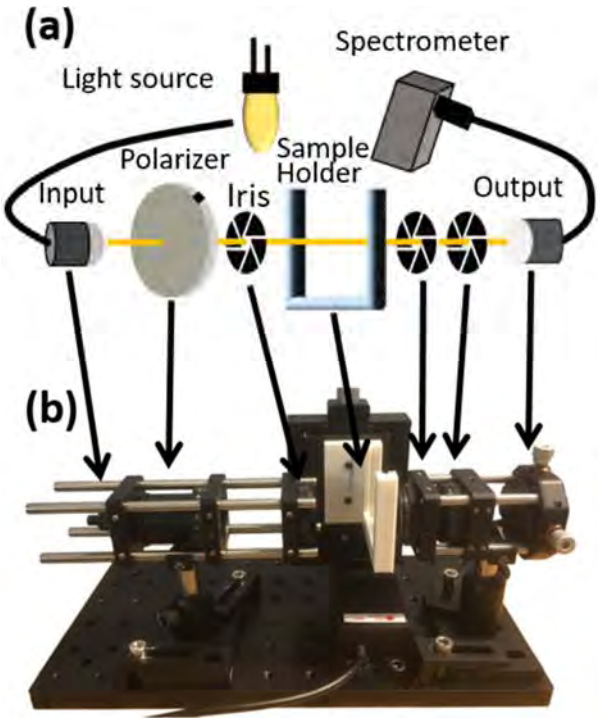

Figure 4. Prototype of the portable scatterometer. (a) Schematic drawing of the setup. (b) Photograph of the setup. The light enters from the left side and encounters the sample mounted in the white sample holder. The undiffracted light is collected at the right side. The light is polarized and collimated using a polarizer and irises.

The entire setup is mounted on two 30 × 15 cm^2 bread boards. One of the boards is shown on Figure 4(b), while the other board contains the spectrometer, the light source and a compact computer to control the different components. A graphical user interface has been developed in Matlab to automatically perform the scatterometry measurements and carry out the analysis.

3.1 Characterization Protocol

Molded parts were continuously evaluated using the scatterometer. For each part, a reference measurement was acquired at a non-structured location of the sample, and two measurements were acquired on patterned areas. Diffraction efficiencies for both patterned areas were calculated and analyzed according to equations (1) and (2). After the analysis, the sample was removed from the stage and wrapped in blue tape (Nitto Europe, Belgium) for protection of the patterned surface. All this could be done comfortably within one minute per sample, including mechanical movements, plotting and data storage. The acquisition time for a single intensity measurement was 3 ms and each database lookup was performed in roughly 40 ms. By implementing a fully automated and optimized system into the injection molding machine, it is estimated that characterization times can be reduced to well below 100 ms. Consequently, all fabricated samples could be characterized without reducing the production throughput.

4. Results and Discussion

Using Topas 5013L-10, a total of seven shim molding temperatures in the range from 90°C to 150°C were investigated and a minimum of five samples were molded for each temperature, resulting in over 50 samples. The shim temperature during the polymer injection phase was varied, while other parameters were kept constant. A total of 11 batches were molded using Topas 8007S-04, with shim temperatures varying from 20°C to 100°C. At least 10 samples were fabricated for each batch. The shim temperature and the cooling time were varied for the different batches.

Even though the difference in optical properties of the two materials is negligible, see Table 1, their glass transition temperatures varies from T_g(Topas 5013) = 134 °C to T_g(Topas 8007) = 78 °C. Consequently, the optimal molding parameters are different for the two materials.

λ/nm	**400**	**500**	**600**	**700**	**800**	**900**
n(5013)	1.547	1.535	1.529	1.526	1.523	1.522
n(8007)	1.549	1.537	1.531	1.528	1.525	1.524

Table 1. Refractive indices of the used polymers for different wavelengths[28].

Each fabricated sample was characterized by the scatterometer. The fields examined by scatterometry in all tests presented here were replicated from a shim field with a period of 1400 nm, and a line width of 700 nm. Furthermore, the grating depth was 633 nm and the sharp rectangular corners had an estimated radius of 0 nm. In order to validate the output from the scatterometer measurements, samples from each batch were characterized with AFM and SEM. In this study, injection molding was used for studying the degree of polymer filling as a result of varying the shim temperature.

Scatterometry measurements on different samples and corresponding SEM images are shown in figure 5. Different degrees of filling of gratings in Topas 5013L-10 yielded significantly different responses. Measured and calculated scatterometry data were found to be in good agreement for the entire temperature range. A sample from the batch using Topas 5013L-10 and a shim temperature near T_g was used for validating the scatterometry measurements, see figure 5(a). The scatterometer measures a height of (630 ± 7) nm, a width of (700 ± 13) nm, both within a confidence interval of 95%, and a sharp top corner with a radius of 0 nm. This corresponds to a good replication with complete filling, which is expected at T_g [29]. The height measured by AFM for the sample is (629 ± 6) nm, at a 68% confidence interval, and the measured width by SEM is (727 ± 27) nm. These findings are in excellent agreement with scatterometry results, which were acquired in a fraction of the time required for AFM and SEM. This demonstrates that the scatterometer is suitable for characterizing structures obtained by complete filling of the shim.

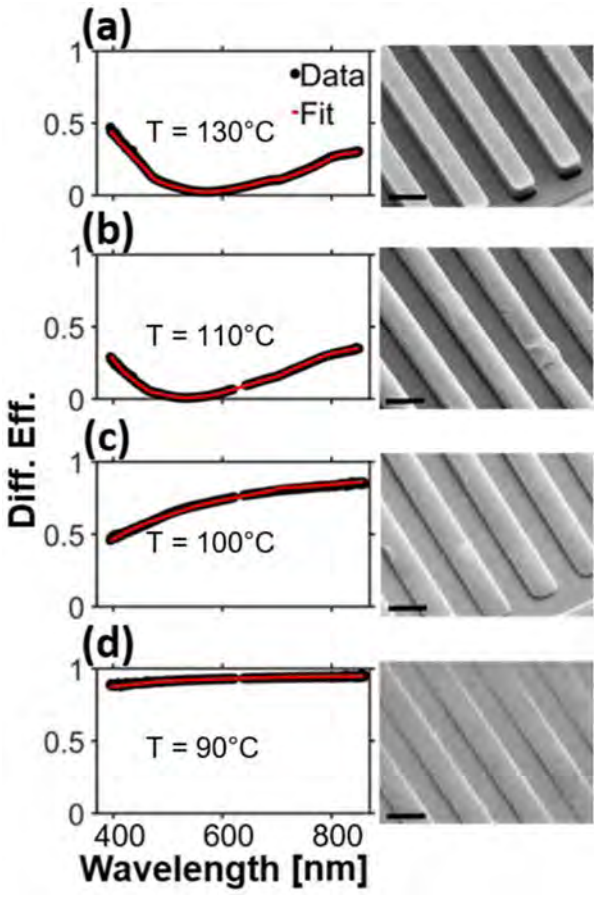

Figure 5. Scatterometry measurements and corresponding SEM images on samples molded at four different temperatures using Topas 5013L-10. The break in the points around 625 nm is due to a saturation of the detector for the reference measurement, these points are not considered in the reconstruction. The scale bar on the SEM images is 1 µm, the tilt angle is 30°.

When using shim temperatures far below T_g, the replicated structures are best described by a line grating with rounded corners and a reduced height. This suggests that the shim's trenches were not completely filled during molding.

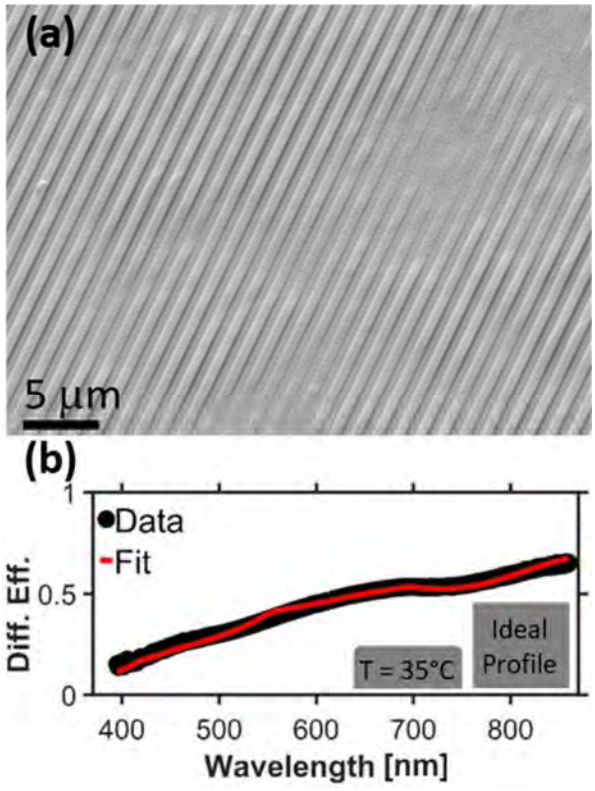

Figure 6. (a) SEM image of a sample molded at T_{Shim} = 35 °C, using Topas 8007S-04. (b) Diffraction efficiencies and best fitting model for the sample shown in (a). Topology variations of the replicated structures cause the found solution to lie within a broad interval. The best fitting model suggests: h = (315 ± 20) nm, w = (790 ± 40) nm and a corner rounding in the interval from 0 to 130 nm. The grating profile for the found structure and a perfectly replicated structure are shown as an insert.

The SEM image in figure 6(a) shows a sample molded at 35 °C. Comparing Figure 6(a) to Figure 5(a), it is clear that the filling of these nanostructures is incomplete. In addition, the height of the grating is subject to large local variations, and the corner roundings are larger at this temperature. Diffraction efficiencies and the best fitting model from a scatterometry measurement on the same sample are shown in Figure 6(b). The scatterometer finds a height of (315 ± 20) nm, a width of (790 ± 40) nm and a corner rounding in the interval of 0 to 130 nm. The height and width found by the scatterometer overlaps, within the 95% confidence interval, with the values measured by AFM and SEM. These measurements indicate a height of (269 ± 44) nm and a width of (711 ± 46) nm, respectively. This demonstrates that even though the scatterometer is not optimal for topology characterization of poorly replicated samples, it is still useful and efficient for distinguishing good and bad replications. Therefore, scatterometry is suitable for

performing quality control of nano-textured samples in production lines. The average height of each batch as a function of the shim temperature is shown in Figure 7(a).

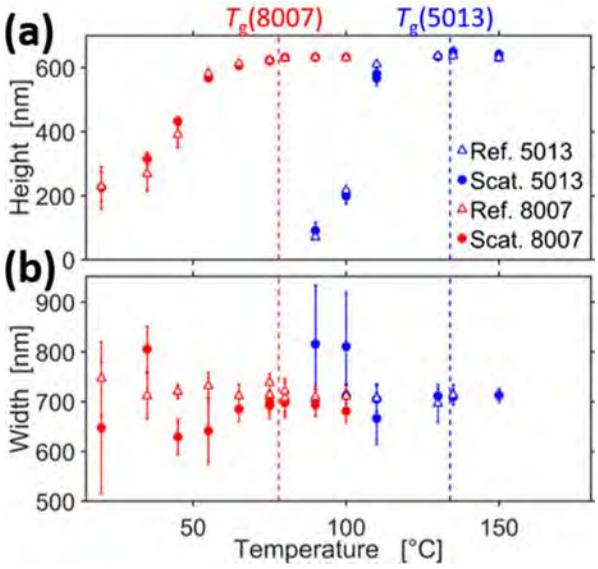

Figure 7. Parameters measured by the scatterometer accompanied by reference measurements. (a) Height of the molded structures as a function of the shim temperature. (b) Width of the molded structures as a function of the shim temperature. Error bars for scatterometry and SEM measurements indicates the 95% confidence limits and error bars for the AFM measurements denotes the *k*=2 expanded uncertainties. The glass transition temperatures for the two polymers are indicated by dashed vertical lines.

The heights reported by scatterometry are an average of all samples within a batch. AFM measurements were performed on three randomly selected samples from each batch. Overall, a good agreement between scatterometry and AFM results is evident. It was observed for both materials that the height decreases as the shim temperature decreases below T_g. No apparent change in height is observed for temperatures above T_g. Overall, the height of the structures is seen to decrease less abruptly for Topas 8007S-04 compared to the structures molded in Topas 5013L-10. The exact cause of this phenomenon is related to rheology [30] and goes beyond the scope of the current study. As a trend, a higher standard deviation is seen for the samples molded at lower temperatures. This implies that the uniformity of these structures is poor, and approximating them as periodic gratings becomes challenging.

The average width of each batch as a function of the shim temperature is seen in Figure 7(b). Here, good agreement between the scatterometer and the SEM is seen for temperatures near T_g. The width is stable around 700 nm, corresponding to the actual width of the lines on the shim. When the shim temperature is far below T_g, the scatterometer estimates the width to be within a very large confidence interval, just barely overlapping the SEM measurements. Again, this indicates that approximating these structures as periodic gratings is not valid when the replication is poor.

Comparison of Figure 5 and Figure 7 clearly shows that the molding temperature has a huge impact on the replicated nanostructures. In this study, we found that the optimal molding temperature is close to T_g. This parameter also influences the injection molding cycle time, since samples molded at higher temperatures would need a longer cooling time to solidify. Hence, the optimal shim temperature should be just high enough to ensure that the molded structures have a replication fidelity that meets the given dimensional tolerances. It is concluded that the optimal molding temperature for this specific injection molding equipment is 10 °C below the glass transition temperature of the used polymer. Optimal molding parameters for different machines can easily be found using the scatterometer.

This study demonstrates that scatterometry is able to characterize nanostructured samples at a pace faster than typical cycle times in injection molding. This makes real time characterization of mass-produced polymer products possible. Since the acquisition time for an intensity measurement is only 3 ms, this measurement is insensitive to vibrations from the injection molding machine. The presented scatterometer is compact and can, with relative ease, be implemented into an existing production line. Based on this, it is concluded that the presented scatterometry technique is highly suitable for checking and ensuring the quality of injection molded nanostructures. Scatterometry makes it possible to optimize injection molding parameters without the use of sophisticated, expensive and time consuming equipment such as AFM and SEM. Therefore, the presented technology offers a wide range of benefits when it comes to reducing waste, increasing throughput and ensuring the quality of polymer products with surface functionalities relying on a high degree of pattern replication fidelity in the production process.

5. Conclusion

This study demonstrates that scatterometry can be used for in-line characterization of injection molded nanostructures in bulk plastic products. 160 nanostructured samples have been fabricated and characterized at a production facility using the scatterometer. The molding parameters are optimized and an optimal mold temperature of 124°C and 68°C are found for the polymers Topas 5013L-10 and 8007S-04, respectively.

AFM and SEM measurements were performed for validation of the method, and excellent agreement with model predictions from scatterometry was found. The scatterometer makes it possible to perform on site characterization of injection molded products with an accuracy down to a few nanometers. The total time required for an intensity measurement including database lookup is below 50 ms, and therefore introducing in-line characterization will not slow down the production rate. These results show that scatterometry is suitable for in-line characterization of nanostructures in plastic consumer products.

Acknowledgements

The authors acknowledge the help of Jesper Fly Hansen during the fabrication and Søren Alkærsig Jensen for discussions and proof reading of the manuscript. The work presented has received funding from The Danish Agency for Science, Technology and Higher Education, the Quantum Innovation Center, the Eurostars project E9745- SuperLens, the EMPIR programme co-financed by the Participating States and from the European Union's Horizon 2020 research and innovation programme through the project 14IND09 MetHPM.

References

[1] A. Saito, Material design and structural color inspired by biomimetic approach, Science and Technology of Advanced Materials. 12 (2011) 064709. doi:10.1088/1468-6996/12/6/064709.
[2] Z. Guo, W. Liu, Biomimic from the superhydrophobic plant leaves in nature: Binary structure and unitary structure, Plant Science. 172 (2007) 1103–1112. doi:10.1016/j.plantsci.2007.03.005.
[3] V.E. Johansen, L.H. Thamdrup, K. Smistrup, T. Nielsen, O. Sigmund, P. Vukusic, Designing visual appearance using a structured surface, Optica. 2 (2015) 239. doi:10.1364/OPTICA.2.000239.
[4] J.S. Clausen, E. Højlund-Nielsen, A.B. Christiansen, S. Yazdi, M. Grajower, H. Taha, U. Levy, A. Kristensen, N.A. Mortensen, Plasmonic Metasurfaces for Coloration of Plastic Consumer Products, Nano Letters. 14 (2014) 4499–4504. doi:10.1021/nl5014986.
[5] M. Zalkovskij, L.H. Thamdrup, K. Smistrup, T. Andén, A.C. Johansson, N.J. Mikkelsen, M.H. Madsen, J. Garnæs, T.T. Kristiansen, M. Diemer, M. Døssing, D. Minzari, P.T. Tang, A. Kristensen, R. Taboryski, S. Essendrop, T. Nielsen, B. Bilenberg, Smart plastic functionalization by nanoimprint and injection molding, in: D.J. Resnick, C. Bencher (Eds.), 2015: p. 94230T. doi:10.1117/12.2085766.
[6] T.A. Osswald, L.-S. Turng, P.J. Gramann, eds., Injection molding handbook, 2nd ed., Updated 2nd ed, Carl Hanser Publishers ; Hanser Gardner Publications, Munich : Cincinnati, 2008.
[7] D.E. Dimla, M. Camilotto, F. Miani, Design and optimisation of conformal cooling channels in injection moulding tools, Journal of Materials Processing Technology. 164–165 (2005) 1294–1300. doi:10.1016/j.jmatprotec.2005.02.162.
[8] H. Schift, C. David, M. Gabriel, J. Gobrecht, L.J. Heyderman, W. Kaiser, S. Köppel, L. Scandella, Nanoreplication in polymers using hot embossing and injection molding, Microelectronic Engineering. 53 (2000) 171–174. doi:10.1016/S0167-9317(00)00289-6.
[9] A.B. Christiansen, J.S. Clausen, N.A. Mortensen, A. Kristensen, Injection moulding antireflective nanostructures, Microelectronic Engineering. 121 (2014) 47–50. doi:10.1016/j.mee.2014.03.027.
[10] P. Utko, F. Persson, A. Kristensen, N.B. Larsen, Injection molded nanofluidic chips: Fabrication method and functional tests using single-molecule DNA experiments, Lab Chip. 11 (2011) 303–308. doi:10.1039/C0LC00260G.
[11] J.A. Slotwinski, E.J. Garboczi, Metrology Needs for Metal Additive Manufacturing Powders, JOM. 67 (2015) 538–543. doi:10.1007/s11837-014-1290-7.
[12] R.K. Leach, Fundamental principles of engineering nanometrology, Second edition, Elsevier, William Andrew, Amsterdam, 2014.
[13] H. Amick, M. Gendreau, C.G. Gordon, Facility vibration issues for nanotechnology research, in: Proceedings of the Symposium on Nano Device Technology, Taiwan, Citeseer, 2002.
[14] H. Watanabe, T. Uchihashi, T. Kobashi, M. Shibata, J. Nishiyama, R. Yasuda, T. Ando, Wide-area scanner for high-speed atomic force microscopy, Review of Scientific Instruments. 84 (2013) 053702. doi:10.1063/1.4803449.
[15] D. Scharf, Viewing and Recording Live Hydrated Specimens with a High-Vacuum SEM, Microscopy Today. 25 (2017) 12–17. doi:10.1017/S1551929516001139.
[16] M.H. Madsen, P.-E. Hansen, M. Zalkovskij, M. Karamehmedović, J. Garnæs, Fast characterization of moving samples with nano-textured surfaces, Optica. 2 (2015) 301. doi:10.1364/OPTICA.2.000301.
[17] M.H. Madsen, P.-E. Hansen, Scatterometry—fast and robust measurements of nano-textured surfaces, Surface Topography: Metrology and Properties. 4 (2016) 023003–023028. doi:10.1088/2051-672X/4/2/023003.
[18] A.C. Diebold, ed., Handbook of silicon semiconductor metrology, Marcel Dekker, New York, 2001.
[19] C. Raymond, Overview Of Scatterometry Applications In High Volume Silicon Manufacturing, in: AIP, 2005: pp. 394–402. doi:10.1063/1.2062993.
[20] B. Bodermann, G. Ehret, J. Endres, M. Wurm, Optical dimensional metrology at Physikalisch-Technische Bundesanstalt (PTB) on deep sub-wavelength nanostructured surfaces, Surface Topography: Metrology and Properties. 4 (2016) 024014. doi:10.1088/2051-672X/4/2/024014.
[21] M.H. Madsen, P.-E. Hansen, Imaging scatterometry for flexible measurements of patterned areas, Optics Express. 24 (2016) 1109. doi:10.1364/OE.24.001109.
[22] M.G. Moharam, T.K. Gaylord, D.A. Pommet, E.B. Grann, Stable implementation of the rigorous coupled-wave analysis for surface-relief gratings: enhanced transmittance matrix approach, Journal of the Optical Society of America A. 12 (1995) 1077. doi:10.1364/JOSAA.12.001077.

[23] M. Kemal Karasu, M. Cakmakci, M.B. Cakiroglu, E. Ayva, N. Demirel-Ortabas, Improvement of changeover times via Taguchi empowered SMED/case study on injection molding production, Measurement. 47 (2014) 741–748. doi:10.1016/j.measurement.2013.09.035.
[24] D. Annicchiarico, J.R. Alcock, Review of Factors that Affect Shrinkage of Molded Part in Injection Molding, Materials and Manufacturing Processes. 29 (2014) 662–682. doi:10.1080/10426914.2014.880467.
[25] B. Sha, S. Dimov, C. Griffiths, M.S. Packianather, Investigation of micro-injection moulding: Factors affecting the replication quality, Journal of Materials Processing Technology. 183 (2007) 284–296. doi:10.1016/j.jmatprotec.2006.10.019.
[26] A. López, J. Aisa, A. Martinez, D. Mercado, Injection moulding parameters influence on weight quality of complex parts by means of DOE application: Case study, Measurement. 90 (2016) 349–356. doi:10.1016/j.measurement.2016.04.072.

Preprint of paper 3

Title:

Scatterometry for optimization of injection molded nanostructures at the fabrication line

Journal:

The International Journal of Advanced Manufacturing Technology, vol. 9-12 (2018)

Authors:

J. S. Madsen, S. A. Jensen, L. Nakotte, A. Vogelsang, L. H. Thamdrup, I. Czolkos, A. Johansson, J. Garnaes, T. Nielsen, J. Nygård and P. E. Hansen

DOI of published paper:

10.1007/s00170-018-2665-7

Scatterometry for optimization of Injection molded nanostructures at the fabrication line

Abstract

A compact scatterometer has been build and tested at a production facility. The scatterometer is used to characterize the feature dimensions of injection molded polymer nanostructures and give on-site direct feedback to the operator on the produced quality. In this way, the injection molding process parameters are iteratively improved until accurate replication of the nanostructures has been achieved. The tests are carried out on two-inch diameter samples with nearly 100 nanostructured areas, consisting of diffractive line gratings with different periods and orientations. It is found that different nanostructures require different process parameters to reach high replication fidelity. Scatterometry measurements are very fast, and will therefore not present a bottleneck when used for quality assurance during production. We furthermore examine the spatial variations in the replicated structures within molded polymer discs using an imaging scatterometer. We demonstrate that the imaging scatterometer is capable of characterizing the entire sample simultaneously, in contrast to the compact scatterometer which performs a local analysis based on measurements on the individual grating regions.

1. Introduction

In nature, micro- and nanostructures can add certain desirable functionalities to a surface. Examples of these include iridescence from the colorful wings of the butterfly [1], or the hydrophobicity of the lotus leaf, which is renowned for its self-cleaning surface [2]. By adding designed and deterministic surface topologies to existing bulk polymer products, one can obtain these functionalities without e.g. chemical modification [3]. This would be beneficial in terms of recycling, and thus reduce the environmental impact of the final product [4]. Furthermore, the colors resulting from structural coloring are very resistant to fading [5,6].

In order to meet the requirements of a mass-consumer market, ongoing research is aimed at introducing micro- and nanostructures in the plastics industry [7]. It has been suggested to produce these structures using injection molding of bulk samples or roll-2-roll embossing of foils [8–11].

Injection molding is a well-established technique in the plastics industry, where molten plastic is injected into a mold cavity. Here it solidifies and retains the form of the cavity [12]. However, high-fidelity injection molding of nanostructures is a challenging task governed by a cornucopia of parameters which must be optimized before functional parts can be produced.

An example of injection molded samples with low and high replication fidelity can be seen in Fig. 1. The structures on the left are barely replicated with heights under 100 nm while the structures on the right are replicated with a height of roughly 620 nm.

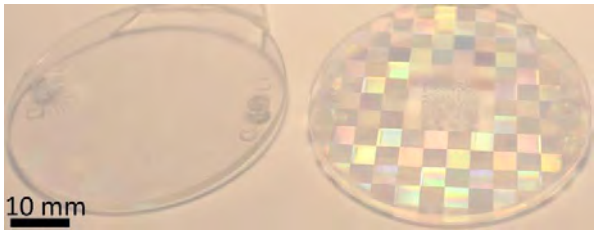

Fig. 1 *Low (left) and high (right) replication fidelity of nanostructures described in section 2.3. Parts consist of Topas 5013-L10, and the colors originate purely from iridescence due to line gratings on the surface*

Due to the high throughput of an injection molding machine, the implementation of current state-of-the-art nanoscale characterization techniques such as SEM and AFM is challenging, and quality assurance is usually only performed on a small subset of samples that are assumed to be representative. Here we show how scatterometry can be employed for at-line characterization and quality control of diffraction based 1D polymer line gratings fabricated by injection molding using a varying set of process parameters. The line gratings are characterized in real time using a portable custom-built scatterometer.

Scatterometry is a technique where the measured scattered light from a surface is compared to computer simulations. This makes it possible to determine the dimensions of the surface structures on the nanometer scale through the use of inverse modelling [13,14]. We demonstrate that the scatterometer measurement time is faster than the cycle time of the injection molding process, and thus enables real-time characterization [15]. This enables the user to continuously optimize an ongoing injection molding process and examine the pattern replication fidelity of a number of predefined small grating areas within the large polymer discs.

The results from these localized measurements are supported by results of all the grating areas of the full 2-inch disc obtained by a single measurement using imaging scatterometry [16]. Furthermore, it is demonstrated that imaging scatterometry makes it possible to detect defects with a resolution of approximately 10 µm within small grating areas.

2. Method

2.1 Scatterometry

In the spectroscopic scatterometry approach employed here, measured, wavelength dependent diffraction efficiencies, $\eta(\lambda)$, are compared to simulated diffraction efficiencies in order to reconstruct the structural parameters of the sample [17].

The measured diffraction efficiencies are defined as the intensity of undiffracted transmitted light relative to the intensity of the incoming light, which is impinging at normal incidence on the sample.

Three wavelength-dependent intensity measurements are used to find these diffraction efficiencies: A measurement on the area with grating structures, $I_{\mathrm{sample}}(\lambda)$, a reference measurement, $I_{\mathrm{ref}}(\lambda)$, performed on an area of the sample without surface structures, and a dark measurement with the light source turned off, $I_{\mathrm{dark}}(\lambda)$. The dark measurement is used to correct for stray light and detector noise.

The diffraction efficiencies can then be calculated according to [16]:

$$\eta(\lambda) = \frac{I_{\mathrm{sample}}(\lambda) - I_{\mathrm{dark}}(\lambda)}{I_{\mathrm{ref}}(\lambda) - I_{\mathrm{dark}}(\lambda)} \tag{1}$$

Simulated diffraction efficiencies are calculated using custom software based on rigorous coupled wave analysis (RCWA). The method has recently been revied in ref [13], which also describes how arbitrary grating profiles can be simulated by dividing the grating profile into rectangular slabs [13,18,19]. The input parameters for the simulation are divided into two categories, $\boldsymbol{\alpha}$ describing the geometrical sample parameters and $\boldsymbol{\Omega}$ describing all other experimental conditions. The periodic line gratings considered in this study, are described by a period, Γ, a height, h, and a width, w. From our experience, these are the most important parameters describing molded samples with low- and high replication fidelity. Other parameters, such as sidewall angle and rounding of the corners have been examined; however, these parameters were previously found to have a high cross correlation with the other parameters [20]. If one wishes to reconstruct more parameters, it is suggested to perform measurements at additional polarizations and/or wavelengths, or to use other characterization techniques to lock either the height or the width of the sample features [21,22]. The input parameters for the simulation are: The wavelength of the incoming light, λ, the polarization of the incoming light with respect to the grating, P, and the angle of incidence, θ. In the simulations, the period is locked to a known value for each grating area, and the angle of incidence is zero, in accordance with the transmission measurement. Hence we have $\boldsymbol{\alpha}(h,w)$ and $\boldsymbol{\Omega}(\lambda,P)$. Fig. **2** illustrates the model parameters.

In this study, we truncate the Fourier series in the RCWA by retaining the diffraction orders from -21 to 21 in the calculations.

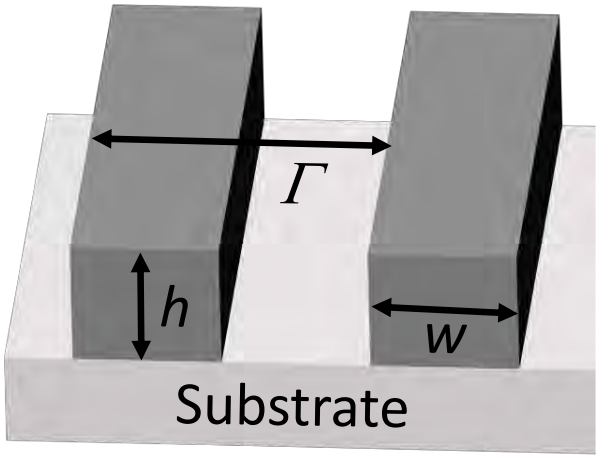

Fig. 2 *Sketch of the model parameters. The model parameters are period (Γ) height (h) and the width (w)*

A library of structures with varying geometrical parameters $\boldsymbol{\alpha}(h,w)$ is simulated in advance of the measurements. After measuring $\eta(\lambda)$, the calculated diffraction efficiencies and measured diffraction efficiencies are compared using a chi-square optimization:

$$\chi^2(\boldsymbol{\Omega}, \boldsymbol{\alpha}) = \frac{1}{N}\sum_{i=1}^{N}\left(\frac{\eta(\lambda_i) - f(\boldsymbol{\Omega_i}, \boldsymbol{\alpha})}{\delta\eta(\lambda_i)}\right)^2 \quad (2)$$

N is the number of wavelengths simulated, $\eta(\lambda_i)$ is the measured diffraction efficiency of the i'th wavelength, $f(\boldsymbol{\Omega_i}, \boldsymbol{\alpha})$ contains all simulated diffraction efficiencies for the i'th wavelength, and $\delta\eta(\lambda_i)$ is the uncertainty of the measured diffraction efficiency at the i'th wavelength. It is then assumed that the model resulting in the lowest chi-square describes the physical sample most accurately. As the time-consuming step of calculating the library of structures is done ahead of the actual measurements, the database comparison, which is performed in real time during in-line characterization, can be done within milliseconds.

For the imaging setup, a series of images is acquired using different wavelengths. In the post-processing, the user can select areas for scatterometry as described above and in ref. [16].

2.2 Instruments

The compact setup is described in detail in [15]. This setup uses a tungsten-halogen light source, which is polarized before impinging on the backside of the sample. The specular transmitted light is picked up from a beam spot of roughly 1 x 1 mm^2 and guided to a spectrometer, measuring in the

spectral range of 450 to 850 nm. The sample is mounted in a custom-build sample holder and placed on an automated XY translation stage. Six fields on a sample can be measured within two minutes. The measurement speed is solely restricted by mechanical movement. Signal acquisition and database lookup are performed in less than 100 ms.

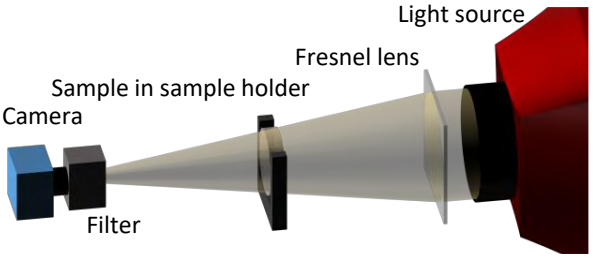

Fig. 3 *Sketch of the Imaging system. The nanostructured surface is facing the camera*

For the imaging scatterometry system, the sample is illuminated by a cold white LED (SOLIS-1C, Thorlabs) which is weakly focused by a Fresnel lens (Focal length 100 mm). A tunable band pass filter (VariSpec Cri, Perkin Elmer), characterized and described in [23], makes it possible to sequentially capture images at different wavelengths over the spectral range of 450-700 nm. A CCD camera (DMK 23UX174, The Imaging Source) with 1920 x 1200 pixels is used to take pictures of the sample. The system is sketched in Fig. 3.

2.3 Injection molding

Samples were produced using a 6-ton injection molding machine (Krauss Maffei, KM110-390C2) at Polyoptics GmbH. Pre-dried Topas 5013-L10 pellets were fed to a cold runner feeding system through a hopper. The pellets were melted under the transport through the injection unit, and subsequently shot into a 70 x 70 mm^2 cavity fitted with a nickel shim. The shim has fields with an area of 4 × 4 mm^2 each, covered by 1D line gratings with periods ranging from 700 nm to 1400 nm. All gratings have a height of roughly 630 nm and a width of half the grating period. Fabrication of the shim is described in ref. [24]. The shim is placed vertically, and the polymer is injected from the top. The grating structures on the shim are oriented either parallel or perpendicular to the flow direction of the polymer. The molten polymer is cooled down under pressure, thereby replicating the nanostructures on the shim. Once the polymer has solidified, the cavity is opened, the molded part is released, and the next cycle starts. The temperature and holding pressure of the cavity was varied for the different samples, while the shot volume was constantly kept at 13 cm^3 (20 cm^3 in the injection unit), the melt temperature in the injection unit was kept at 280 °C and the cooling time locked to 75% of the cycle time. The cavity temperature was controlled by a thermal water unit from HB-Therm. The injection speed was regulated in order to avoid flow lines (typically around 10 cm^3/s). Injection times

were approximately 3 seconds. Each sample was characterized using scatterometry immediately after the molding.

3. Results

For this study, over 100 samples were fabricated using different injection molding parameters. All samples were characterized by the compact scatterometer immediately after production.

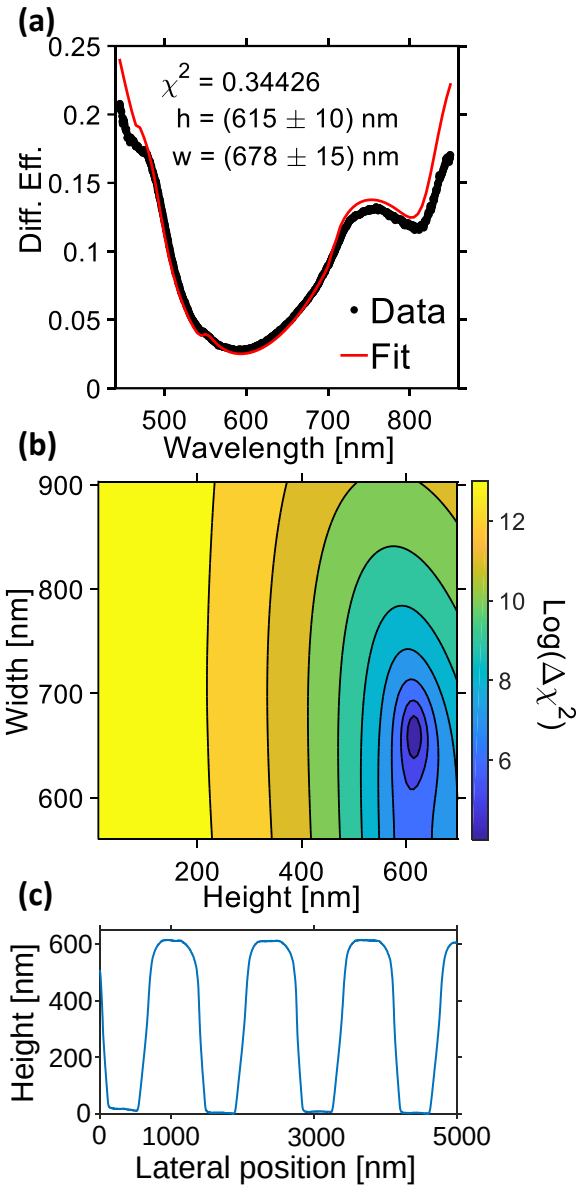

Fig. 4 *Reconstruction of the grating parameters. (a) Measured diffraction efficiencies, best fitting model and found model parameters. (b) Goodness of fit as a function of the model parameters. (c) AFM profile of the sample*

In Fig. 4 (a), the measured diffraction efficiencies, the best fitting model and the reconstructed structural parameters are shown. The sensitivity of the fit quality to changes in the structural parameters is quantified by calculating the difference in χ^2 between the model at a given set of parameters, and the best fitting model with the minimum χ^2 : $\Delta\chi^2 = \chi^2_{model} - \chi^2_{min}$.

In Fig. 4 (b), $\Delta\chi^2$ for a range of parameters is shown for a single sample. It is seen that a unique solution for a best fitting height and width was found. The fit becomes gradually worse as one moves away from this solution. An AFM profile from the sample can be seen in Fig. 4(c).

Fig. 5 shows the height of samples molded at increasing pressure at a cavity temperature of 120°C. Each data point represents the average height measured on five samples that were fabricated using identical pressure and temperature conditions. Three areas on each sample, corresponding to identical structures on the shim, were measured, as shown in the insert. The areas 1, 2 and 3 have vertical distances of 10 mm, 26 mm and 42 mm, respectively, from the injection gate, which is below position 1. Each of these areas contain a field (Γ=1400 nm) where the grating orientation is perpendicular to the flow of the injected polymer, and another field (Γ=1000 nm) with gratings parallel to the injection direction. The scatterometry measurements are accompanied by sampled AFM measurements for comparison. The AFM (Park Systems, NX 20) was operated in tapping mode and equipped with a specified apex radius below 10 nm (NanoSensors, PointProbe Plus). The scanned area was 10 x 10 μm^2. The microscope was calibrated in the z-direction using a step height reference as described in [25]. The scatterometry measurements are in agreement with the AFM measurements within the 95% confidence interval. Based on this comparison, it is concluded that the scatterometry height measurements are both accurate and reliable.

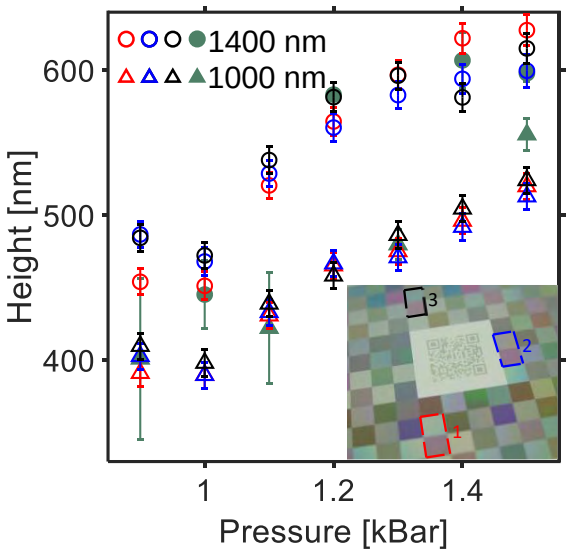

Fig. 5 *Measured heights of the samples as a function of molding pressure. The samples have been measured at the positions corresponding to the insert position 1, 2 and 3 for structures with a period of 1400 nm (circle) and 1000 nm (triangle). AFM measurements were performed on position 1, and indicated by filled markers. The molding temperature was kept constant at 120°C. It is noted that the height does not change as a function of the position*

We see that the polymer structure height approaches the target height of 630 nm on the Ni shim as the pressure increases. However, the grating fields with Γ=1000 nm are more prone to incomplete filling. The improved quality with increasing holding pressure is consistent with previous studies [26]. Line gratings with a period of 1000 nm do not reach the target height when using pressures below 1600 bar and a fixed cavity temperature of 120°C. Replication fidelity was previously found to depend intimately on temperature [15]. Based on these findings, it is concluded that the quality of injection molded nanostructures is favored by high holding pressure and high cavity temperature. It is found that the height does not depend on the position on the sample, but rather on what structure is replicated. This result suggests that we have an even distribution of pressure and temperature in the cavity.

In order to demonstrate that the scatterometer can be used to optimize the injection molding process parameters, samples were molded by starting out with a holding pressure of 800 bar and a cavity temperature of 100°C and iteratively increasing these parameters until a feature height corresponding to the target height on the Ni shim was obtained. These results are presented in Fig. ***6***. The target height was reached with a pressure of 1600 bar and a temperature of 130 °C. This clearly shows that the scatterometer can be used to optimize an injection molding recipe via a fast in-line procedure by finding the conditions necessary to replicate the shim structures. Due to the high measurement speed of the scatterometer, characterization of the fabricated samples did not slow down the production process, which had cycle times of around a minute.

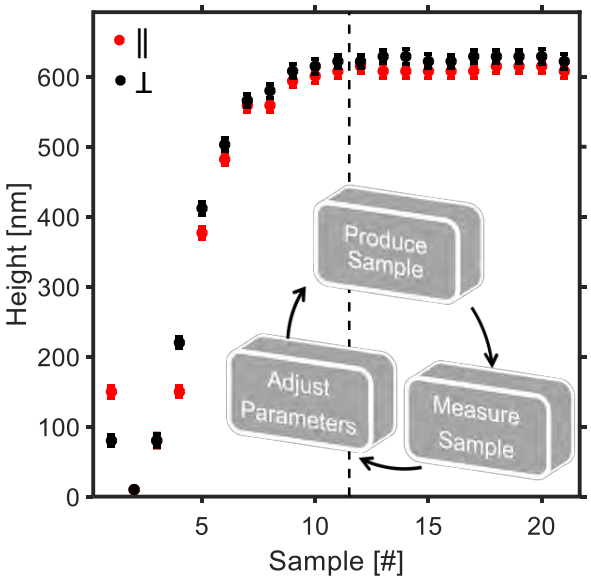

Fig. 6 *Height of the replicated structures. Between each sample, the temperature or pressure was changed to optimize the injection molding recipe. The measured gratings where either parallel (∥) or perpendicular (⊥) to the polymer melt injection direction. After eleven iterations, indicated by the dashed line, the molding parameters were locked and another ten samples were produced to monitor the stability of the process*

Fig. ***6*** shows data for areas where the orientation of the line gratings are both perpendicular and parallel to the injection direction of the polymer melt. Grating structures aligned parallel to the melt flow seems to have a slightly larger height, but once the optimum molding conditions have been established, the measured heights for the two fields overlap within the confidence intervals. Since the total time for an intensity measurement and a database lookup is below 100 ms, this technique is suitable for in-line characterization of injection molded samples, which have typical fabrication times from tens of seconds to minutes.

We conclude that structures of different dimensions need different molding parameters for optimizing the replication fidelity. It is therefore challenging to simultaneously replicate nanostructures of varying width and height accurately using injection molding. Here, the scatterometer is a valuable tool in terms of optimizing molding parameters without relying on time-consuming and expensive nanoscale characterization techniques such as SEM and AFM.

To further investigate the overall replication homogeneity on individual samples, measurements were performed using an imaging scatterometer. Diffraction efficiencies from all pixels in an area covering

a sample and measured at a wavelength of 650 nm are shown in Fig. **7**. The analyzed fields are indicated by the lines, and the corresponding spectra and spatial parameters can be seen on the left.

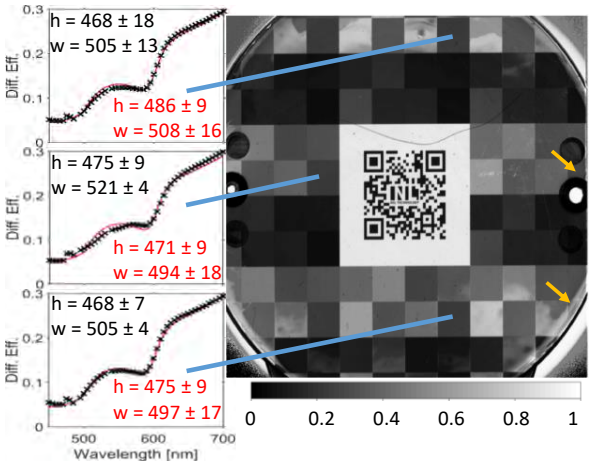

Fig. 7 *Diffraction efficiencies acquired for all pixels at a wavelength of 650 nm. Scatterometry analyses of the areas indicated by the lines are seen on the graphs. The parameters found by the imaging analysis are stated in the upper left, and the parameters found by the compact scatterometer in the lower right- all in units of [nm]. The three fields have a period of 1000 nm. Similar fields at the edge of the sample are analyzed. These areas are marked by an arrows and are found to have a height of (447 ± 31) nm and (447 ± 65) nm, for the upper and lower respectively. Macroscopic defects, like the scratch above the QR-code, can be detected by eye, and nanostructured areas can be analyzed with a click*

We see that the parameters found by the imaging setup are consistent with those found by the compact scatterometer and AFM in Fig. **5**. The average signal from 5 x 5 pixels is analyzed for each marked area. Furthermore, we have examined two areas near the edges in Fig. **7**. These areas would at best be very hard to measure with conventional scatterometry. The scatterometer estimates the heights to be (447 ± 31) nm and (447 ± 65) nm, respectively. The heights found from these fields have a larger variation, which might come from a worse replication. The heights found seem lower, however this cannot be concluded since the values overlap within the confidence intervals.

The technique makes it very intuitive to perform the scatterometry analysis, and the operator can clearly see, on which portion of the sample the analysis is performed. This makes it straightforward to ascertain the reliability of the measurements and to remedy misalignment of the sample or to detect macroscopic defects. If the sample is rotated around the plane of the beam, the polarization of collected light with respect to the grating will become a mix of two polarizations, with a ratio determined by the rotation angle. This can easily be corrected by the user in the post processing of the data, and would not necessitate a new measurement.

It is again found, that the replication fidelity is independent of the macroscale location on the molded sample. This could be interpreted as a result of the pressure and temperature being constant at

different positions within the cavity. This enables a control of non-periodic structures through periodic test structures. If test structures are well replicated, functional structures with similar feature size and geometry should also be subject to complete filling.

To demonstrate the usefulness of breaking the spot size limit associated with conventional scatterometry [15], a zoomed-in measurement series was performed at the center of a sample, see Fig. ***8***(a). Scatterometry analyses were performed on 20,000 individual pixels in the marked area. The found height for each pixel is shown in Fig. ***8***(b). The analyses clearly distinguish between areas with- or without grating pattern. Furthermore, some defects can be seen on the grating, pinpointing exactly where the replication quality is poor.

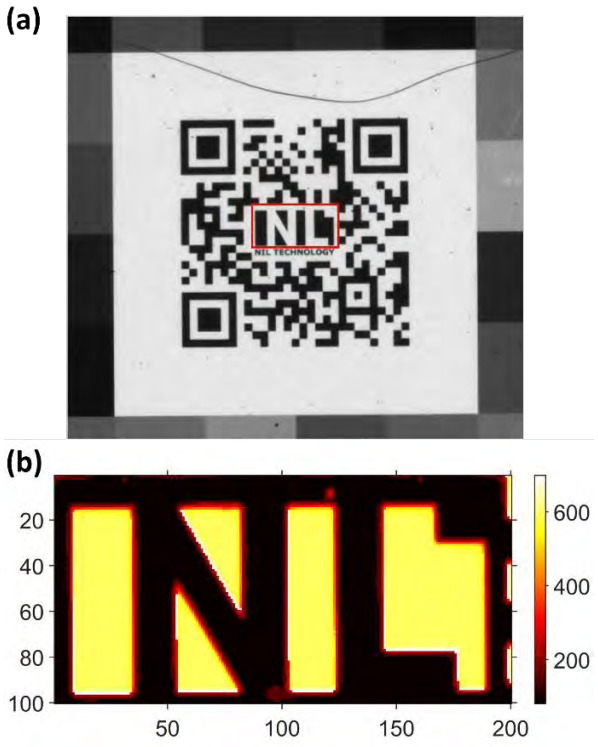

Fig. 8 *(a) Diffraction efficiencies for a wavelength of 650 nm. (b) Found heights from the marked area in (a). The gratings have been used to print a logo. The scatterometer clearly distinguishes between grating and non-grating areas, and defects/impurities can be spotted*

Defects outside the grating area are also observed. These defects are approximated as gratings in the analyses. We find it important to emphasize that this is not several small patterned areas, but the compound result of the scatterometer always finding a best fit solution. Hence an area with severe defects would appear more like a patterned area than a plain substrate to the scatterometer. We are not able to characterize these defects, but we are able to detect them and show where they are on the sample.

Pixels on the edge of the grating reconstruct heights and widths differently than pixels within the grating. As a trend, the pixels on the edge reconstructs a lower height and a larger width. This could be interpreted to mean that the structures are poorly replicated at the edges of the grating. However, this cannot be concluded from scatterometry, since the pixels at the edge of the grating get a mixed signal from grating and non-grating areas. The analyses have no information about scattering from different sample segments, but assumes a uniform grating, and therefore the analyses are not valid for the edge areas. The extent of these edge areas are roughly 50 µm, which corresponds to three pixels. This would imply that each pixel gets a signal contribution from the adjacent pixels. The same measurement was performed without the Fresnel lens, giving the same results for the edge areas, thus hinting that this is not due to a focusing effect. These edge areas cannot be reconstructed reliably. We can, however, safely reconstruct the structural parameters for areas within the grating.

The robustness of the reconstruction depends highly on the wavelengths used for the measurement. Using more wavelengths makes the reconstruction more stable. This however, comes at the cost of increased measurement time in the imaging setup. Ideally, the signal should have a lot of curve features to ensure stability. With a priori knowledge of the sample, one could use a non-linear wavelength distribution to put emphasis on wavelengths requiring a low exposure time, and which have unique features. This can be achieved by testing whether a section of the spectra, defined by a moving window of variable size, can be described by a straight line within a given tolerance. The points within a window passing the test can then be reduced to the end points in the window. Looking at Fig. 7, one would find that the majority of data points should be in-between wavelengths of 500 and 600 nm, where we see the most gradient changes as a function of wavelength, while most of the signal above 615 nm can be well approximated by straight lines.

The acquisition time of the image scatterometer is similar to the time it takes the compact scatterometer to measure and analyze six fields, but currently it requires an operator for the analysis. Machine learning might be implemented to automate this step. Our future work will focus on performing the imaging analysis on all the fields in parallel. With a smart selection of the measurement wavelength regime and automation of the analysis, the system might be implemented for autonomous in-line characterization.

Non-imaging spectroscopic scatterometry has the advantage of measuring more wavelengths over a broader spectrum, making the reconstruction more robust. On the other hand, the imaging setup makes it possible to measure areas smaller than the beam spot. This makes it possible to shrink the area of test structures, which is already desired in the semiconductor industry [27]. In terms of speed, non-imaging measurements are much faster when measuring on a single field, and have been demonstrated to work for in-line purposes [15]. However, due to the physical translation required

when measuring multiple fields, the measurement time drastically increases for multiple areas. Here the Imaging scatterometer is faster, since it addresses the entire area of the sample simultaneously.

4. Conclusion

A compact scatterometer was demonstrated at a production facility, where it was used to characterize injection molded nanostructures during production. This proved very useful in optimizing the injection molding parameters. Samples were molded at different holding pressures and cavity temperatures, and different areas on the discs were examined using scatterometry. The heights determined by the scatterometer were in agreement with AFM measurements. An imaging scatterometer capable of measuring a full 2-inch disc was demonstrated, where areas down to tens of square microns can be analyzed with nanometer precision. Future work will focus on parallelization and automation of the imaging analysis. We found good replication fidelity with sufficiently high pressure and temperature. This work demonstrates that scatterometry can enable implementation of functional nanostructures in mass-production and become an essential technique for quality control or process optimization in the production of nanostructured plastic parts.

Funding information

The work presented has received funding from The Danish Agency for Institutions and Educational Grants, the Quantum Innovation Center, the Eurostars projects: E9745- SuperLens and E8875-InFoScat, and the EMPIR programme co-financed by the Participating States and from the European Union's Horizon 2020 research and innovation programme through the project 14IND09 MetHPM.

References

[1] L.P. Biró, J.P. Vigneron, Photonic nanoarchitectures in butterflies and beetles: valuable sources for bioinspiration, Laser Photonics Rev. 5 (2011) 27–51. doi:10.1002/lpor.200900018.

[2] Z. Wang, L. Xu, X. Wu, J. Chen, A designable surface via the micro-molding process, Microsyst. Nanoeng. 4 (2018) 17099. doi:10.1038/micronano.2017.99.

[3] J.S. Clausen, E. Højlund-Nielsen, A.B. Christiansen, S. Yazdi, M. Grajower, H. Taha, U. Levy, A. Kristensen, N.A. Mortensen, Plasmonic Metasurfaces for Coloration of Plastic Consumer Products, Nano Lett. 14 (2014) 4499–4504. doi:10.1021/nl5014986.

[4] V.E. Johansen, L.H. Thamdrup, K. Smistrup, T. Nielsen, O. Sigmund, P. Vukusic, Designing visual appearance using a structured surface, Optica. 2 (2015) 239. doi:10.1364/OPTICA.2.000239.

[5] A.S. Roberts, A. Pors, O. Albrektsen, S.I. Bozhevolnyi, Subwavelength Plasmonic Color Printing Protected for Ambient Use, Nano Lett. 14 (2014) 783–787. doi:10.1021/nl404129n.

[6] H. Jiang, M. Rezaei, M. Abdolahi, B. Kaminska, Solvent-free optical recording of structural colours on pre-imprinted photocrosslinkable nanostructures, Nano Futur. 1 (2017) 025001. doi:10.1088/2399-1984/aa7986.

[7] A.B. Christiansen, J.S. Clausen, N.A. Mortensen, A. Kristensen, Injection moulding antireflective nanostructures, Microelectron. Eng. 121 (2014) 47–50. doi:10.1016/j.mee.2014.03.027.
[8] M. Matschuk, N.B. Larsen, Injection molding of high aspect ratio sub-100 nm nanostructures, J. Micromechanics Microengineering. 23 (2013) 025003. doi:10.1088/0960-1317/23/2/025003.
[9] S. Murthy, M. Matschuk, Q. Huang, N.K. Mandsberg, N.A. Feidenhans'l, P. Johansen, L. Christensen, H. Pranov, G. Kofod, H.C. Pedersen, O. Hassager, R. Taboryski, Fabrication of Nanostructures by Roll-to-Roll Extrusion Coating: Roll-to-Roll Fabrication of Nanostructures, Adv. Eng. Mater. 18 (2016) 484–489. doi:10.1002/adem.201500347.
[10] C. Zhang, P. Yi, L. Peng, X. Lai, J. Chen, M. Huang, J. Ni, Continuous fabrication of nanostructure arrays for flexible surface enhanced Raman scattering substrate, Sci. Rep. 7 (2017) 39814. doi:10.1038/srep39814.
[11] H. Jiang, B. Kaminska, Scalable Inkjet-Based Structural Color Printing by Molding Transparent Gratings on Multilayer Nanostructured Surfaces, ACS Nano. (2018). doi:10.1021/acsnano.7b08580.
[12] T.A. Osswald, L.-S. Turng, P.J. Gramann, eds., Injection molding handbook, 2nd ed., Updated 2nd ed, Carl Hanser Publishers ; Hanser Gardner Publications, Munich : Cincinnati, 2008.
[13] M.H. Madsen, P.-E. Hansen, Scatterometry—fast and robust measurements of nano-textured surfaces, Surf. Topogr. Metrol. Prop. 4 (2016) 023003–023028. doi:10.1088/2051-672X/4/2/023003.
[14] C. Raymond, Overview Of Scatterometry Applications In High Volume Silicon Manufacturing, in: AIP, 2005: pp. 394–402. doi:10.1063/1.2062993.
[15] J.S. Madsen, L.H. Thamdrup, I. Czolkos, P.-E. Hansen, A. Johansson, J. Garnaes, J. Nygard, M.H. Madsen, In-line Characterization of Nanostructured Mass-produced Polymer Components Using Scatterometry, J. Micromechanics Microengineering. 27 (2017) 085004–085010. doi:10.1088/1361-6439/aa7a3a.
[16] M.H. Madsen, P.-E. Hansen, Imaging scatterometry for flexible measurements of patterned areas, Opt. Express. 24 (2016) 1109. doi:10.1364/OE.24.001109.
[17] M.H. Madsen, P.-E. Hansen, M. Zalkovskij, M. Karamehmedović, J. Garnæs, Fast characterization of moving samples with nano-textured surfaces, Optica. 2 (2015) 301. doi:10.1364/OPTICA.2.000301.
[18] J.J. Hench, Z. STRAKOvS, The RCWA method-a case study with open questions and perspectives of algebraic computations, Electron. Trans. Numer. Anal. 31 (2008) 331–357.
[19] M.G. Moharam, T.K. Gaylord, D.A. Pommet, E.B. Grann, Stable implementation of the rigorous coupled-wave analysis for surface-relief gratings: enhanced transmittance matrix approach, J. Opt. Soc. Am. A. 12 (1995) 1077. doi:10.1364/JOSAA.12.001077.
[20] J.S. Madsen, P.E. Hansen, P. Boher, D. Dwarakanath, J.F. Jørgensen, B. Bilenberg, J. Nygård, M.H. Madsen, Study on Micrograting Using Imaging, Spectroscopic, and Fourier Lens Scatterometry, J. Micro Nano-Manuf. 5 (2017) 031005–031011. doi:10.1115/1.4036889.
[21] X. Niu, N. Jakatdar, J. Bao, C.J. Spanos, Specular spectroscopic scatterometry, IEEE Trans. Semicond. Manuf. 14 (2001) 97–111.
[22] A. Vaid, B.B. Yan, Y.T. Jiang, M. Kelling, C. Hartig, J. Allgair, P. Ebersbach, M. Sendelbach, N. Rana, A. Katnani, E. Mclellan, C. Archie, C. Bozdog, H. Kim, M. Sendler, S. Ng, B. Sherman, B. Brill, I. Turovets, R. Urensky, A holistic metrology approach: hybrid metrology utilizing scatterometry, CD-AFM, and CD-SEM, in: C.J. Raymond (Ed.), 2011: p. 797103. doi:10.1117/12.881632.
[23] D. Wierzbicki, M. Wili, Liquid crystal tunable filters in detecting water pollution, in: Vilnius Gediminas Technical University Press "Technika" 2014, 2014. doi:10.3846/enviro.2014.013.
[24] M. Zalkovskij, L.H. Thamdrup, K. Smistrup, T. Andén, A.C. Johansson, N.J. Mikkelsen, M.H. Madsen, J. Garnæs, T.T. Kristiansen, M. Diemer, M. Døssing, D. Minzari, P.T. Tang, A. Kristensen, R. Taboryski, S. Essendrop, T. Nielsen, B. Bilenberg, Smart plastic functionalization by nanoimprint and injection molding, in: D.J. Resnick, C. Bencher (Eds.), 2015: p. 94230T. doi:10.1117/12.2085766.
[25] J. Garnaes, N. Kofod, A. Kühle, C. Nielsen, K. Dirscherl, L. Blunt, Calibration of step heights and roughness measurements with atomic force microscopes, Precis. Eng. 27 (2003) 91–98. doi:10.1016/S0141-6359(02)00184-8.
[26] M. Calaon, G. Tosello, H.N. Hansen, C. Ravn, A. Islam, Packing parameters effect on injection molding of polypropylene nanostructured surfaces, in: Proc. 70th Annu. Tech. Conf. Exhib., 2012.
[27] 2013 ITRS, Int. Technol. Roadmap Semicond. (n.d.). http://www.itrs2.net/2013-itrs.html (accessed March 16, 2018).

Chapter 7

Optimizations

Up until now, most structural parameters estimated by the different scatterometer setups have been reported with a confidence limit based on the goodness of fit between simulated and measured data. This chapter demonstrates a method to calculate uncertainties for scatterometry measurements based on general Least Square Optimization (LSQ). The general least square rutine used in this thesis is based on the work described in [29]. The first section describes the general Least Square rutine with a few examples from the world of scatterometry, while the second section shows some scatterometry results and discusses the found uncertainties. The third section describes how a Tinkhonov regularization works and how it can be applied to the inverse modelling to make it more robust.

7.1 General LSQ

Let us for a general measurement of m quantities denote the exact value $\boldsymbol{\zeta}$ such that: $\boldsymbol{\zeta}$=(ζ_1,...,ζ_m), but due to measurement errors, the measured value is $\boldsymbol{z}$: $\boldsymbol{z}$=(z_1,...,z_m), with uncertainties denoted $u(z_i)$ for the i'th measurement. The m quantities can be found either by direct measurement or from well established tables in literature.
From scatterometry, an example of these quantities could be three intensity measurements: Sample, I_{Sample}, Reference, I_{Ref}, and Dark, I_{Dark}, all performed at the same wavelengths.

In addition, the set of measurements may involve k quantities with no a priori information. These quantities will be denoted: $\boldsymbol{\beta}$=(β_1,...,β_k). Going back to the world of scatterometry, these quantities could be the grating period, height, width or other parameters used to describe the structure of the grating. $\boldsymbol{\zeta}$ and $\boldsymbol{\beta}$ are connected by physical laws or constraints, $\boldsymbol{f}(\boldsymbol{\zeta}, \boldsymbol{\beta})$, which can be described as:

$$\boldsymbol{f}(\boldsymbol{\zeta}, \boldsymbol{\beta}) = \begin{pmatrix} f_1(\boldsymbol{\zeta}, \boldsymbol{\beta}) \\ f_2(\boldsymbol{\zeta}, \boldsymbol{\beta}) \\ \vdots \\ f_N(\boldsymbol{\zeta}, \boldsymbol{\beta}) \end{pmatrix} = \mathbf{0} \tag{7.1}$$

where N is the number of constraints. For scatterometry, we would have:

$$\eta(\boldsymbol{\beta}, \lambda_i) = \frac{I_{\text{Sample}}(\lambda_i) - I_{\text{Dark}}(\lambda_i)}{I_{\text{Ref}}(\lambda_i) - I_{\text{Dark}}(\lambda_i)} \tag{7.2}$$

meaning that the diffraction efficiency for each wavelength depends on $\boldsymbol{\beta}$. Rewriting it as a constraint of the form of equation (7.1):

$$f_i(\boldsymbol{\zeta}, \boldsymbol{\beta}) = I_{\text{Sample}}(\lambda_i) - I_{\text{Dark}}(\lambda_i) - \eta(\boldsymbol{\beta}, \lambda_i)(I_{\text{Ref}}(\lambda_i) - I_{\text{Dark}}(\lambda_i)) = 0 \tag{7.3}$$

In the above case, one would have a constraint for each wavelength the three measurements have been performed at. These constraints are used to find $\boldsymbol{\zeta}$ and $\boldsymbol{\beta}$ by minimizing the chi-square function:

$$\chi^2 = (\boldsymbol{z} - \boldsymbol{\zeta})\boldsymbol{\Sigma}^{-1}(\boldsymbol{z} - \boldsymbol{\zeta}) \tag{7.4}$$

where $\boldsymbol{\Sigma}$ is the covariance matrix given by:

$$\begin{pmatrix} u(z_1)^2 & u(z_1, z_2) & \cdots & u(z_1, z_m) \\ u(z_2, z_1) & u(z_2)^2 & & \\ \vdots & & \ddots & \vdots \\ u(z_m, z_1) & & \cdots & u(z_m)^2 \end{pmatrix} \tag{7.5}$$

where, $u(z_i, z_j) = u(z_i)\boldsymbol{r}(z_i, z_j)u(z_j)$, and $\boldsymbol{r}(z_i, z_j)$ is the correlation between the i'th and the j'th measurement [46]. In most, cases the different measurements are initially assumed to be independent of one another, and the correlation matrix, $\boldsymbol{r}$, becomes unity. Under this assumption (7.4) reduces to the chi-square function described in section 2.3.

A practical way to connect the chi-square function and the constrains is through Lagrange multipliers [47], $\boldsymbol{\lambda}$, not to be confused with λ used for the wavelength. One can formulate a function:

$$\boldsymbol{\Phi}(\boldsymbol{\zeta}, \boldsymbol{\beta}, \boldsymbol{\lambda}, \boldsymbol{z}) = (\boldsymbol{z} - \boldsymbol{\zeta})\boldsymbol{\Sigma}^{-1}(\boldsymbol{z} - \boldsymbol{\zeta}) + \boldsymbol{\lambda}\boldsymbol{f}(\boldsymbol{\zeta}, \boldsymbol{\beta}) \tag{7.6}$$

If a solution $(\hat{\boldsymbol{\zeta}}, \hat{\boldsymbol{\beta}})$ exists to this problem, the gradient at that point should be zero. Taking the gradient of $\boldsymbol{\Phi}$ at the solution, one arrive at the so called "normal equations" of the least square problems:

$$\begin{aligned} -\boldsymbol{\Sigma}^{-1}(\boldsymbol{z} - \hat{\boldsymbol{\zeta}}) + \nabla_\zeta \boldsymbol{f}(\hat{\boldsymbol{\zeta}}, \hat{\boldsymbol{\beta}})\boldsymbol{\lambda} = 0 \\ \nabla_\beta \boldsymbol{f}(\hat{\boldsymbol{\zeta}}, \hat{\boldsymbol{\beta}})\boldsymbol{\lambda} = 0 \\ \boldsymbol{f}(\hat{\boldsymbol{\zeta}}, \hat{\boldsymbol{\beta}}) = 0 \end{aligned} \tag{7.7}$$

Where:

$$\nabla_\zeta \boldsymbol{f} = \begin{pmatrix} \frac{\partial f_1}{\partial \zeta_1} & \cdots & \frac{\partial f_1}{\partial \zeta_m} \\ \vdots & \ddots & \vdots \\ \frac{\partial f_n}{\partial \zeta_1} & \cdots & \frac{\partial f_n}{\partial \zeta_m} \end{pmatrix} \quad \text{and} \quad \nabla_\beta \boldsymbol{f} = \begin{pmatrix} \frac{\partial f_1}{\partial \beta_1} & \cdots & \frac{\partial f_1}{\partial \beta_k} \\ \vdots & \ddots & \vdots \\ \frac{\partial f_n}{\partial \beta_1} & \cdots & \frac{\partial f_n}{\partial \beta_k} \end{pmatrix}$$

By using an initial solution, one can refine the solution through iteration. This is done by changing $\boldsymbol{\beta}$ and $\boldsymbol{\zeta}$ in small steps, $\Delta\boldsymbol{\beta}$ and $\Delta\boldsymbol{\zeta}$, according to:

$$\begin{pmatrix} \boldsymbol{\beta}_{l+1} \\ \boldsymbol{\zeta}_{l+1} \\ \boldsymbol{\lambda}_{l+1} \end{pmatrix} = \begin{pmatrix} \boldsymbol{\beta}_l \\ \boldsymbol{\zeta}_l \\ 0 \end{pmatrix} + \begin{pmatrix} \Delta\boldsymbol{\beta}_l \\ \Delta\boldsymbol{\zeta}_l \\ \boldsymbol{\lambda}_{l+1} \end{pmatrix} \tag{7.8}$$

here l is the step index and the stepsize is given by:

$$\boldsymbol{D}(\boldsymbol{\beta}_l, \boldsymbol{\zeta}_l) \begin{pmatrix} \Delta\boldsymbol{\beta}_l \\ \Delta\boldsymbol{\zeta}_l \\ \boldsymbol{\lambda}_{l+1} \end{pmatrix} = \begin{pmatrix} \mathbf{0} \\ -\boldsymbol{\Sigma}^{-1}(\boldsymbol{z} - \boldsymbol{\zeta}_l) \\ -\boldsymbol{f}(\boldsymbol{\zeta}_l, \boldsymbol{\beta}_l) \end{pmatrix} \tag{7.9}$$

Where:

$$\boldsymbol{D}(\boldsymbol{\beta}_l, \boldsymbol{\zeta}_l) = \begin{pmatrix} \mathbf{0}^{(k,k)} & \mathbf{0}^{(k,m)} & \nabla_\beta \boldsymbol{f}(\boldsymbol{\zeta}_l, \boldsymbol{\beta}_l) \\ \mathbf{0}^{(m,k)} & \boldsymbol{\Sigma}^{-1} & \nabla_\zeta \boldsymbol{f}(\boldsymbol{\zeta}_l, \boldsymbol{\beta}_l) \\ \nabla_\beta \boldsymbol{f}(\boldsymbol{\zeta}_l, \boldsymbol{\beta}_l) & \nabla_\zeta \boldsymbol{f}(\boldsymbol{\zeta}_l, \boldsymbol{\beta}_l) & \mathbf{0}^{(n,n)} \end{pmatrix} \tag{7.10}$$

Here $\mathbf{0}^{(i,j)}$ is a matrix of zeros of the size $i \times j$. Given that the initial starting guess is sufficiently good, the iterations should converge towards the best solution:

$$\begin{pmatrix} \hat{\boldsymbol{\beta}} \\ \hat{\boldsymbol{\zeta}} \\ \hat{\boldsymbol{\lambda}} \end{pmatrix} = \lim_{l \to \infty} \begin{pmatrix} \boldsymbol{\beta}_l \\ \boldsymbol{\zeta}_l \\ \boldsymbol{\lambda}_l \end{pmatrix} \tag{7.11}$$

The trivial stating value for $\boldsymbol{\zeta_1}$ is the measured value $\boldsymbol{z}$. The starting value of $\boldsymbol{\beta_1}$ is more challenging. In this thesis, the least square approach is only used to improve scatterometry results and refine the uncertainties, $\boldsymbol{\beta_1}$ is taken to be the parameters from the original "traditional scatterometry analysis" described in Chapter 2.

Normally, if the scatterometry analysis is succesfull, the converged $\boldsymbol{\beta}$ will be close to $\boldsymbol{\beta_1}$, so all this tedious math may seem redundant, however, what is won here is quite significant: The inverse of the calculated matrix $\boldsymbol{D}(\boldsymbol{\beta}_l, \boldsymbol{\zeta}_l)$ contains information about the uncertainty of the solutions $\boldsymbol{\beta}$, $\boldsymbol{\zeta}$ and the correlation between them.

$$\boldsymbol{D}(\boldsymbol{\beta}_l, \boldsymbol{\zeta}_l)^{-1} = \begin{pmatrix} u(\hat{\boldsymbol{\beta}}, \hat{\boldsymbol{\beta}}) & u(\hat{\boldsymbol{\beta}}, \hat{\boldsymbol{\zeta}}) & [] \\ u(\hat{\boldsymbol{\zeta}}, \hat{\boldsymbol{\beta}}) & u(\hat{\boldsymbol{\zeta}}, \hat{\boldsymbol{\zeta}}) & [] \\ [] & [] & -u(\boldsymbol{\lambda}, \boldsymbol{\lambda}) \end{pmatrix} \tag{7.12}$$

Where the square brackets denotes entries in the matrix not containing information about the variance. This means that the uncertainties of $\boldsymbol{z}$ can be rigorously propagated to the unknown parameters $\boldsymbol{\beta}$. In addition, we also obtain the full correlation matrix for all values of $\boldsymbol{z}$ and $\boldsymbol{\beta}$. Hopefully the correlation between the individual beta parameters are sufficiently low, otherwise one should consider if the correlated parameters can be safely reconstructed simultaneously. This can be utilized as a meticulous method to estimate if the number of free parameters in a scatterometry model is sufficient or if it should be increase or decreased.

7.2 Scatterometry Example

Examples of scatterometry measurements on rectangular plastic gratings, described in Chapter 6, can be seen in figure 7.1. The measured parameters ($\boldsymbol{\zeta}$): I_{Sample}, I_{Dark} and I_{Ref} and the model parameters ($\boldsymbol{\beta}$): Grating height and width, are evolved with the constraint (7.3). After each iteration, the values of the constraint is checked. When the constraint is below a user specified threshold for all wavelengths (in our case 10^{-8}), the evolution is stopped, and the reached parameters are believed to be the best estimate of the true value, shown on the right. In table 7.1, the model parameters before and after are shown for the three gratings. It can be seen that the uncertainties found by the least square approach is significantly lower than the ones estimated by the confidence intervals. This warrants a short discussion of the uncertainties.

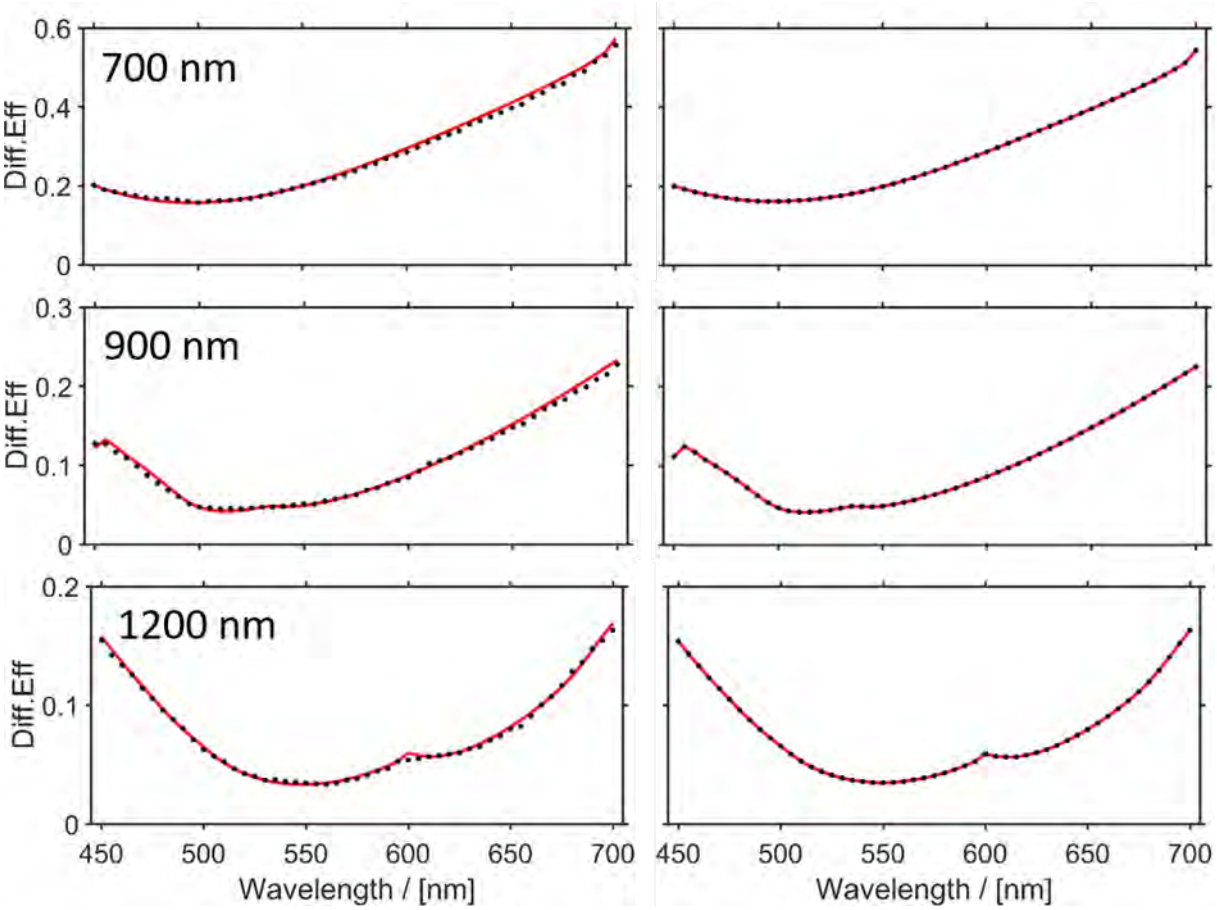

Figure 7.1: (left) Measured diffraction efficiencies (black dots) and best fitting model (red line) for three transparent gratings of different periods of 700 nm, 900 nm and 1200 nm. (Right) "True" value of measurements found by using least square approach and best fitting model. The changes in $\boldsymbol{\beta}$ (red line) are more subtle than the changes in $\boldsymbol{\zeta}$ (black dots).

The intensity measurements are performed with a detector measuring N counts for a given wavelength. The N counts are assumed to be Poisson distributed, and the uncertainty is therefore $u_I = \sqrt{N}$. These initial uncertainties affect the $\boldsymbol{\Sigma}^{-1}$, which in turn affects χ^2 as described in (7.4). Thus a simple way to evaluate if these initial uncertainties are "fair" is by looking at the resulting χ^2. Given that $\boldsymbol{\Sigma}^{-1}$ has been

correctly estimated, a χ^2-value, after normalizing with the number of wavelengths minus the number of β parameters, should be expected to obtain values close to unity [48]. The χ^2-values and the correlation between height and width is reported in table 7.2.

Nominal Pitch	Height Before[a]	Height After[b]	Width Before[a]	Width After[b]
700	624 ± 16	617 ± 4	364 ± 28	374 ± 7
900	626 ± 17	624 ± 3	468 ± 27	473 ± 3
1200	624 ± 16	614 ± 2	624 ± 24	627 ± 2

[a]± denotes confidence interval.
[b]± denotes k=2 expanded uncertainties.

Table 7.1: Model parameters h and w before and after the least square rutine. All units are in nanometers.

Nominal Pitch	χ^2	ρ
700	0.217	-0.67
900	0.331	-0.15
1200	0.985	-0.28

Table 7.2: Normalized χ^2 and the correlation, ρ, between height and width of the rectangular grating.

Looking at table 7.2 we can see that the χ^2-values are all below, but close to 1. Therefore it is concluded, that the reported uncertainties are realistic, and that the confidence interval overestimates the uncertainties. This does imply that given a good scatterometry reconstruction, it is safe to assume that the true value of the measured parameter is within the range specified by the confidence limit. One should be warned that this least square method is quite computational and time consuming. Therefore one should consider if the extra information obtained is needed for a given application. This method does provide a way to obtained uncertainties on the reconstructed parameters traceable to the instrument, which was the goal of this chapter.

7.3 Tinkhonov Regularizations

When the inverse problem does not have a unique best solution, the problem is considered ill-posed [49]. The most common way to deal with ill-posed problems are Tinkhonov regularizations. It is also known as "ridge regression" in the field of statistics [50] and goes by the name of "weight decay" in modern machine learning [51]. The Tinkhonov regularization is easily explained by looking at the simple system:

$$\boldsymbol{ax} = b, \quad \text{or} \quad \boldsymbol{ax} - b = 0 \tag{7.13}$$

A simple minimization method would minimize the euclidean norm: $|\boldsymbol{ax} - b|$. However, if more values of $\boldsymbol{x}$ gives similar solutions, additional information is required for a robust reconstruction. Given a priori information about the system, one can add a regularization term, $\Gamma|\boldsymbol{x} - \boldsymbol{x_0}|$, so the system to be minimized would read: $|\boldsymbol{ax} - b| + \Gamma|\boldsymbol{x} - \boldsymbol{x_0}|$. Here x_0 is the a priori expected solution and $|\Gamma|$ is the magnitude of penalty usually inversely proportional to the accuracy of the measurement. By using a good physical choice for $|\Gamma|$ and x_0, solutions with certain values of $\boldsymbol{x}$ are preferred. In addition, this can be used to avoid overfitting noisy data, as shown in figure 7.2, by setting entries of $\boldsymbol{x_0}$ to zero in order to penalize higher order, non linear terms. In the case of scatterometry, the optical response is modelled as a function of the experimental conditions and the sample $f(\Omega, \alpha)$. By comparing the measured diffraction efficiencies η with the modeled response, one would minimize: $|f(\Omega, \alpha) - \eta|$, by changing α. This is usually a simple task, but in cases where several solutions exist, reference measurements will typically be used to choose the correct solution. With a Tinkhonov regularization, the reference measurement can be directly incorporated into the reconstruction by minimizing:

$$|f(\Omega, \alpha) - \eta| + \Gamma|\alpha - \alpha_0| \tag{7.14}$$

Here α_0 would take the value measured by a reference measurement and Γ would be inversely proportional to the uncertainty of the measurement. This is also extremely helpful in cases where the found solution is unphysical. Here the regularization term can be used to penalize unphysical solutions. In Chapter 8 it will be shown how this regularization is used to combine measurements from the AFM with measurements from ellipsometry and scatterometry to characterize a complex sample.

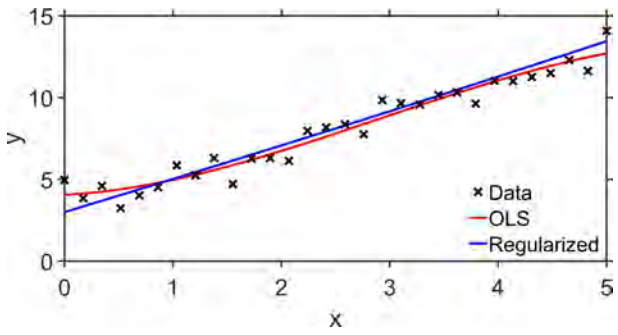

Figure 7.2: Simple example showing how Tinkhonov can be used to avoid overfitting of noisy data (black crosses). The red line represents an ordinary least square fit using a third order polynomial. The blue line shows a fit using a Tinkhonov regularized fit penalizing large non-linear terms.

Chapter 8

Hybrid Metrology

Samples from the real world are often rather complex and not well described by simple gratings. In these cases, it is necessary to include additional model parameters to describe the samples. However, to avoid "over-fitting", additional data is needed to make the inverse modeling robust. In this chapter, it is shown how data from different instruments can be incorporated into the inverse modeling to obtain additional information. This allows for a more complex reconstruction. We call this combination of measurement instruments hybrid metrology. Specifically, this is done by combining: Spectroscopic scatterometry, spectroscopic ellipsometry, and AFM. The work presented here is a result of the Euramet project Traceable three-dimensional nanometrology (Project number 15SIB09). Part of this work is also reported in a paper submitted to Optics Express.

8.1 Sample

The investigated sample is a grating of silicon cylinders in a square lattice with a nominal period of 200 nm, in both the x- and y-direction, placed on a silicon substrate. The cylinders have a nominal height of 100 nm and a nominal width of 80 nm. The sample parameters are sketched in figure 8.1.

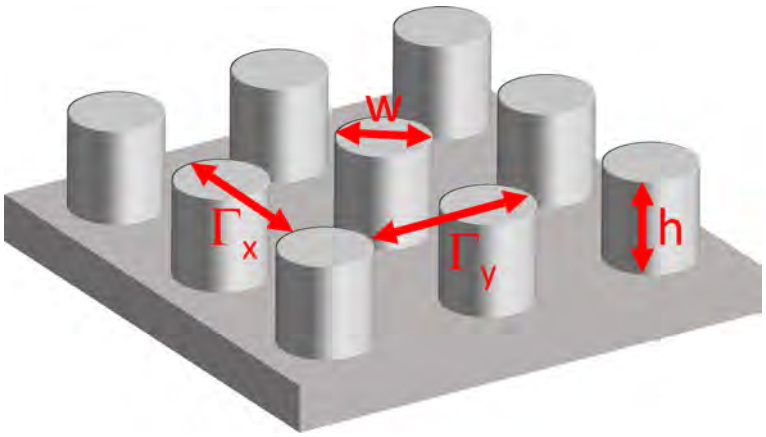

Figure 8.1: Sketch of the sample measured in the 3D Nano project.

8.2 Scatterometry

For the optical measurements, the sample was illuminated by a laser-driven light source (Energetic, EQ-99X) at an angle of incidence of 70 degrees with respect to the sample normal. The light was polarized, both before and after the sample, perpendicular to the illumination plane. A spectrometer (Ocean Optics, FLAME-S-XR1-ES) was used to collect the wavelength resolved intensity signal. The reference measurement was taken on a flat piece of Si100. The dark measurement was taken with the light source blocked.

Assuming heights and widths according to the nominal values of the sample, a scatterometry library was calculated by letting the height vary from 50 nm to 150 nm, and the width from 40 to 140 nm. The results are shown in figure 8.2. The best fitting model finds a height of 78 nm, a width of 108 nm, and estimates the uncertainties of these parameters to be sub nanometer. However, this model finds a chi-square of 39.4, indicating that we do not have a very good fit. This result suggests that the two parameters height and width are insufficient to fully characterize the sample. In order to justify a more complex model, additional data is acquired using other characterization techniques, we employ ellipsometry and AFM.

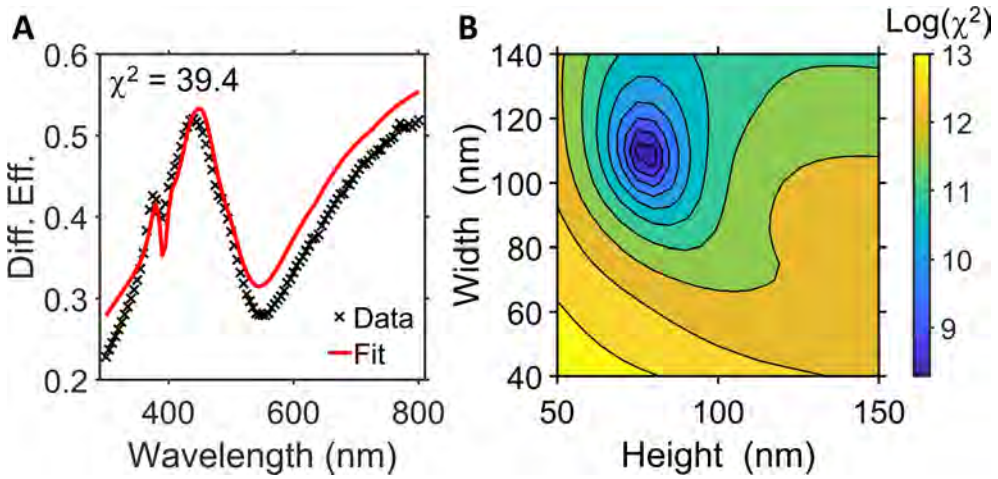

Figure 8.2: Scatterometry measurement and reconstruction of the sample. (A) Measured diffraction efficiency and best fitting model. (B) Goodness of fit as a function of the model parameters. The best fitting solution finds a height of (78 ± 2) nm and a width of (108 ± 4) nm. The χ^2 of 39.4 indicates that we do not have a very good fit between model and data.

8.3 Ellipsometry

Ellipsometry is a technique closely related to scatterometry [52]. It was originally designed to measure optical properties and thicknesses of thin films [53]. Rather than measuring the intensity of the reflected light, ellipsometry measures the change in polarization. This is done by illuminating a specific polarized state from a polarization state generator (PSG) and measuring the reflected or transmitted light using a polarization state analyzer (PSA). The PSG and PSA each consist of a polarizer and a photo elastic modulator. The setup is sketched in figure 8.3.

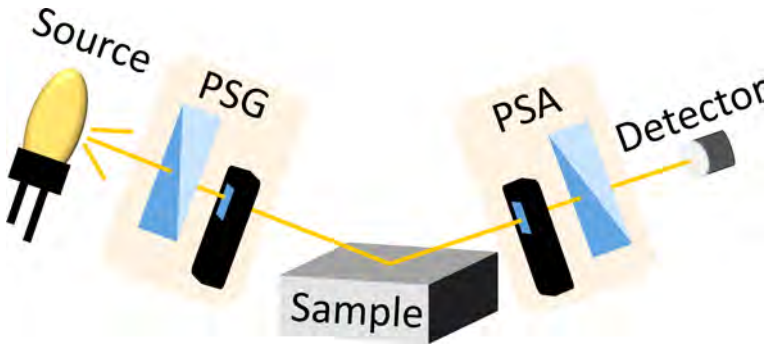

Figure 8.3: Sketch of a basic ellipsometer. The output from a light source is passed through the PSG before impinging on the sample. The reflected light is modulated by the PSA before it enters the detector.

The interaction between light and sample as measured by the ellipsometer is commonly described by the vector:

$$\rho(\lambda) = \frac{r_p(\lambda)}{r_s(\lambda)} = |\rho(\lambda)| \cdot e^{i\Delta(\lambda)} \tag{8.1}$$

Where $r_p(\lambda)$ and $r_s(\lambda)$ are the Fresnel reflection coefficients for p- and s-polarized light respectively. The measured values of $|\rho(\lambda)|$ and $\Delta(\lambda)$ are shown in figure 8.4. Ellipsometry has a couple of advantages compared to scatterometry: First, the ellipsometer finds two parameters for the inverse modeling. $|\rho|$ commonly carries information similar to η from scatterometry, while the phase parameter Δ is often very sensitive so small changes. This means that $|\rho|$ can be used to estimate a rough model and Δ can be used for fine-tuning the model parameters. Since ellipsometry measures the relation between two polarization states, a reference measurement of the incoming light is not needed.
Since RCWA can be used to calculate the field reflection coefficients r_p and r_s, it can also be used to find $|\rho(\lambda)|$ and $\Delta(\lambda)$. Thus these parameters can be used in the inverse modeling of ellipsometry data as $\eta(\lambda)$ is used in intensity based scatterometry.

8.4 AFM

The working principle of the AFM can be seen in figure 8.5. The AFM is operated in non-contact mode where the tip is set to oscillate a few nanometers over the sample surface [54]. As the tip experiences forces from the surface (mainly van der Waals

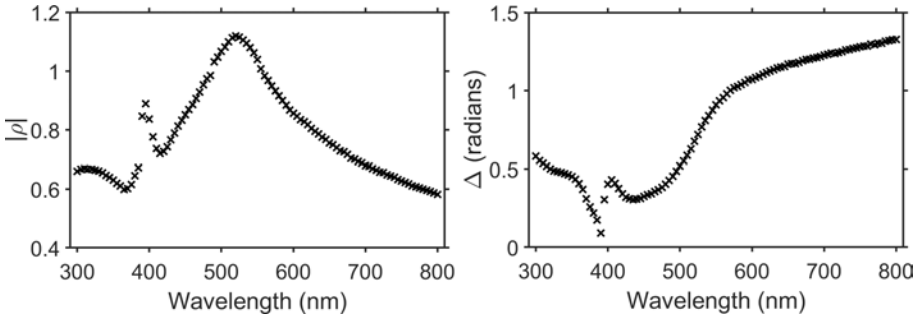

Figure 8.4: Measurements of $|\rho|$ (right) and Δ (left) as a function of the wavelength.

forces for non conducting samples) the frequency of the oscillation changes [55]. A laser beam hits the backside of the cantilever, and the reflected beam is measured by a quadrant detector to determine the position of the cantilever; this signal is passed to a feedback loop controlling the Z-stage. This makes it possible to get very accurate readings of the Z-profile of a surface. A more detailed explanation of the feedback loop can be found in [56]. The AFM used is a metrology AFM (Park Systems,

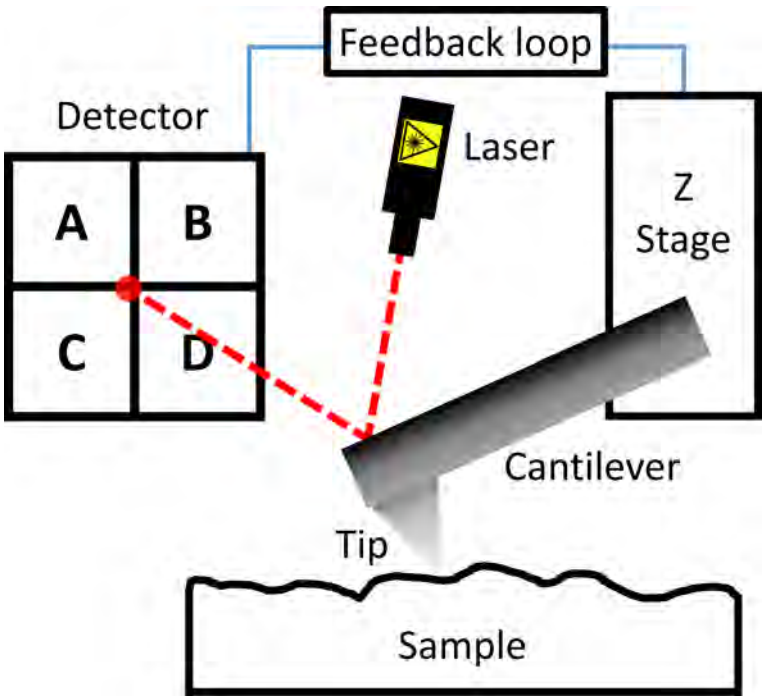

Figure 8.5: Sketch of the working principle behind the AFM.

NX 20). An AFM profile from the sample can be seen in figure 8.6. The acquired measurements are analyzed in the SPIP software package (Image Metrology, Vers. 6.5.1). The step heights are calculated according to the ISO 5436 standard. A height of $h = (93 \pm 3)$ nm is found. This height is closer to the nominal value of the sample and supports the idea that a non-optimal model has been used in the scatterometry reconstruction.

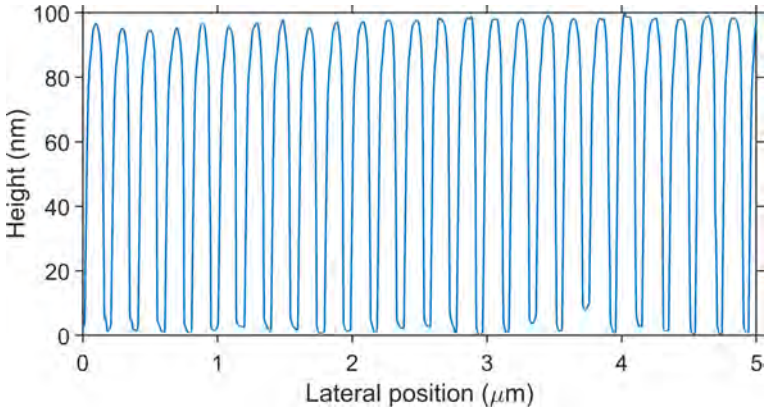

Figure 8.6: Sample profile from the AFM. The Height is found to be $h = (93 \pm 3)$ nm

8.5 Hybrid Reconstruction

Based on the scatterometers inability to reconstruct the sample, a more complex model is needed. In order to avoid overfitting additional data obtained from the ellipsometer and the AFM is incorporated into the inverse modeling. Using all the acquired data from the three systems, the best fitting model is found by minimizing the following χ^2:

$$\chi^2 = \frac{(h_{AFM} - h^c)^2}{\sigma(h_{AFM})^2} + \frac{1}{3N}\sum_i^N \frac{(\eta_i - \eta_i^c)^2}{\sigma(\eta_i)^2} + \frac{(\rho_i - \rho_i^c)^2}{\sigma(\rho_i)^2} + \frac{(\Delta_i - \Delta_i^c)^2}{\sigma(\Delta_i)^2} \tag{8.2}$$

Where the superscript c indicates values calculated by RCWA, σ indicates the uncertainty on the measurement, i is an index over the different wavelengths used in the scatterometry and ellipsometry reconstruction. Note that the scatterometry and ellipsometry data are performed at the same wavelengths. This method is essentially a standard chi-square formulation with the Tikhonov term $\frac{(h_{AFM}-h^c)^2}{\sigma(h_{AFM})^2}$ added. With this additional information, it can be justified to add additional model parameters. Four additional parameters have been added to describe the sample:

1. A sidewall angle, θ.
2. A convex smearing of the top corner.
3. A concave smearing of the bottom corner.
4. A native oxide layer

The added parameters (except for the oxide layer) are sketched in figure 8.7. Ideally all the new parameters should be reconstructed together with the height and the width, however, this proved unfeasible due to a slow convergence rate and restrictions on computation time. Instead this was done, by iteratively keeping two of the four new parameters locked in the new simulations, it was found that the sidewall angle had the largest influence on the reconstruction. Based on the simulations, the values of R_{top} and R_{bot} was locked to 5 nm. A corner rounding on this scale would be expected from the resolution of large area EBL. These structures were most likely written with a large current, and therefore a large beam diameter. The thickness of

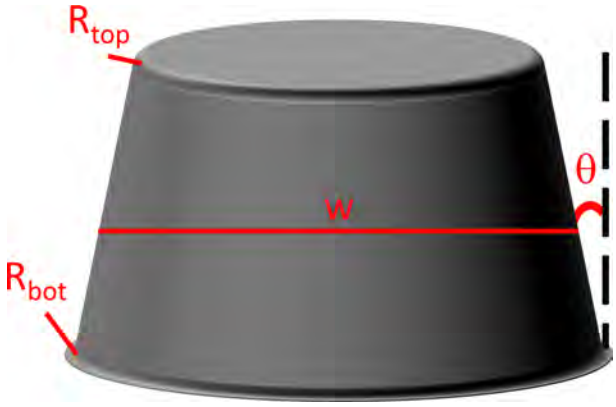

Figure 8.7: Sketch of the final sample model and the new parameters. R_{top} and R_{bot} denotes the radius of the circle describing the corner roundings. θ denotes the sidewall angle and w is now taken to be the FWHM of the trapezoidal. The oxide layer has been omitted in this sketch.

the native oxide layer was locked to 2 nm, a value in agreement with literature [57]. The results of the final analysis using the three free parameters h, w and θ can be seen in figure 8.8. We can see that the best fitting model agrees with all of the different measurements. The resulting fit has a chi-square value of $\chi^2 = 1.3$. Here 0.8 comes from the sum term and 0.5 from the Tinkohonov term. This shows, not surprisingly, that a more advanced model finds a better fit, and that combining different instruments one gets a more robust measurement.

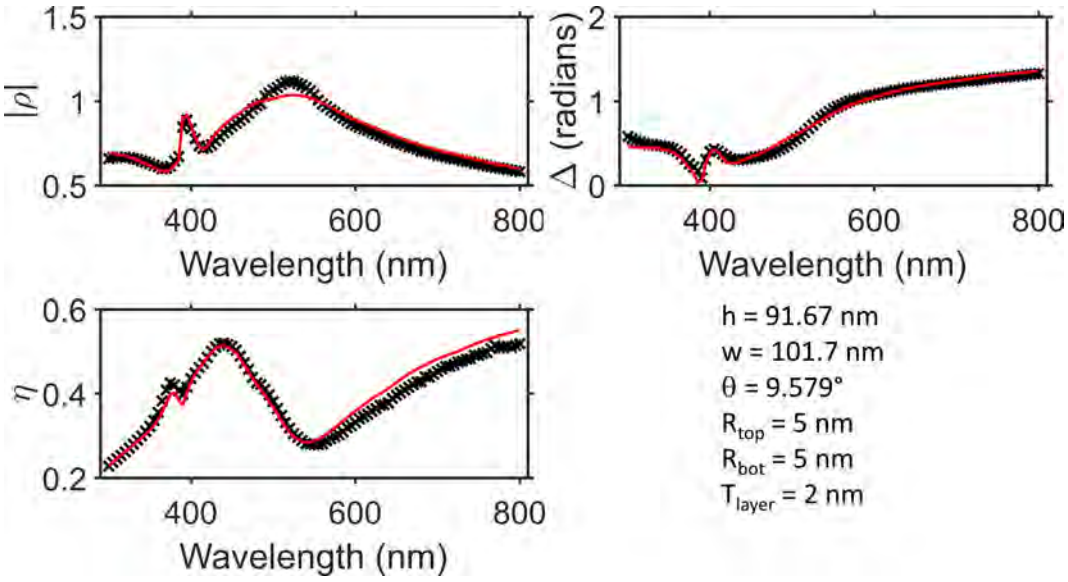

Figure 8.8: Ellipsometry measurements of $|\rho|$ (top left) and Δ (top right), scatterometry measurements of η (bottom left) and the parameters found by the combined inverse modelling (bottom right).

Once a solution has been found, the uncertainty for the evaluated parameters are found from the diagonal elements of the covariance matrix Σ defined by:

$$\Sigma = \left(\boldsymbol{J}^T \boldsymbol{U}^{-1} \boldsymbol{J}\right)^{-1} \tag{8.3}$$

Where $\boldsymbol{U}$ is a matrix containing all the squared measurement uncertainties in the diagonal and all other entries are zero:

$$\boldsymbol{U} = \begin{bmatrix} \sigma(\eta_1)^2 & & & & & & & & & \\ & \ddots & & & & & & & & \\ & & \sigma(\eta_N)^2 & & & & & \mathbf{0} & & \\ & & & \sigma(\rho_1)^2 & & & & & & \\ & & & & \ddots & & & & & \\ & & & & & \sigma(\rho_N)^2 & & & & \\ & & & & & & \sigma(\Delta_1)^2 & & & \\ & & & & & & & \ddots & & \\ & & & \mathbf{0} & & & & & \sigma(\Delta_N)^2 & \\ & & & & & & & & & \sigma(h_{AFM}) \end{bmatrix} \tag{8.4}$$

and $\boldsymbol{J}$ is a Jacobian of the RCWA solver given by:

$$\boldsymbol{J} = \begin{pmatrix} \frac{\partial \eta_1^c}{\partial h} & \frac{\partial \eta_1^c}{\partial w} & \frac{\partial \eta_1^c}{\partial \theta} \\ \vdots & \vdots & \vdots \\ \frac{\partial \eta_N^c}{\partial h} & \frac{\partial \eta_N^c}{\partial w} & \frac{\partial \eta_N^c}{\partial \theta} \\ \\ \frac{\partial \rho_1^c}{\partial h} & \frac{\partial \rho_1^c}{\partial w} & \frac{\partial \rho_1^c}{\partial \theta} \\ \vdots & \vdots & \vdots \\ \frac{\partial \rho_N^c}{\partial h} & \frac{\partial \rho_N^c}{\partial w} & \frac{\partial \rho_N^c}{\partial \theta} \\ \\ \frac{\partial \Delta_1^c}{\partial h} & \frac{\partial \Delta_1^c}{\partial w} & \frac{\partial \Delta_1^c}{\partial \theta} \\ \vdots & \vdots & \vdots \\ \frac{\partial \Delta_N^c}{\partial h} & \frac{\partial \Delta_N^c}{\partial w} & \frac{\partial \Delta_N^c}{\partial \theta} \\ \\ \frac{\partial h^c}{\partial h} & \frac{\partial h^c}{\partial w} & \frac{\partial h^c}{\partial \theta} \end{pmatrix} \tag{8.5}$$

Which is numerically evaluated at the found solution. The results are reported in table 8.1. It should be noted that the width reported here is measured at FWHM. Given the found height and sidewall angle, this would correspond to a top width of $w_{top} = 86 \pm 1$ nm, which is not far from the nominal value from the manufacturer.

h (nm)	w (nm)	θ (°)
92 ± 1	101.7 ± 0.3	9.6 ± 0.8

Table 8.1: Results of the hybrid reconstruction.

Based on these results, it is concluded that given enough information, it is possible to safely reconstruct complex samples in the inverse modeling.

Chapter 9

Nanowires

One prospective application for electronic nanostructures is quantum computing [58]. The key component of a quantum computer is the quantum bit, qubit, which is the quantum analog to a classical bit [59]. The main difference between a classical bit and a qubit is that the qubit exists in a superposition of on ($|1\rangle$) and off ($|0\rangle$). This fundamental property may be used in future quantum computing to parallelize a computation problem. One of the most promising candidates for a semiconductor qubit is the semiconductor nanowire [61, 62]. A nanowire can be, primitively, described as a cylinder with a diameter under 100 nm and a length of microns. SEM images of wires are shown in figure 9.1.

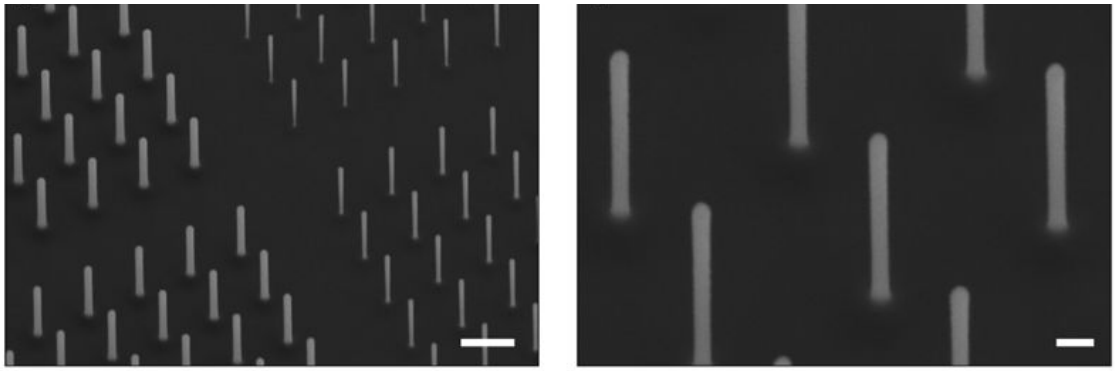

Figure 9.1: (left) Wires with different widths in square arrays with a pitch of 1 μm, all wires have a height of 1.7 μm. (right) zoomed image on the lower right field. The scale bars are 1 μm and 200 nm respectively. Image from [60].

Nanowires made of heavy-element III-V semiconductors such as InAs, have a strong spin-orbit interaction and a high g-factor meaning that they require a smaller magnetic field to reach the same level of energetic effects [63].
Nanowires can be grown by Molecular Beam Epitaxy (MBE), which is a complicated science involving several process steps [64]. When fabricating wires, a common practice is to follow a well-established recipe and only characterize the finalized wires after all process steps. This is partly because conventional characterization techniques such as SEM are very time-consuming and in some cases damages the sample, e.g. before and after an electron beam lithography process. If the final wires are found to be flawed, the operator has to guess what went wrong and start

all over. It is therefore desirable to have a characterization method to monitor the progress before- and after each of the different fabrication steps.

At the University of Lund they have already demonstrated an interference based reflectometry method, used for in-situ monitoring of nanowires in their MBE system [65]. Furthermore, they have deployed scatterometry like methods to characterize large arrays of thick wires in a dense hexagonal lattice (widths of over 120 nm and periods of 400 nm) [66]. Here the nanowires were investigated using a microscope with a field of view of 100 by 100 square microns and a scan was used to measure 2.2 mm line. Optical simulations of nanowires are already used in research to investigate their effects in areas such as solar cell energy harvesting, LED lighting, opto electrical effects and biosensing [67–70] and could therefore also become an essential tool at the growth site, both for fabrication and characterization.

This chapter is divided in three sections. A section concerning characterization of the different fabrication steps in the nanowire growth process, a section concerning concerning characterization of the final wires, and a section using the Lyot filter described in Chapter 5 to perform imaging scatterometry on the wires.

9.1 Fabrication

A simplified fabrication process for nanowires is outlined in the following [71]:

Wire fabrication steps:

1. A wafer is cleaned in HF (typically InAs at QDev).
2. Electron resist in spin coated onto the wafer.
3. A pattern is written on the wafer using electron beam lithography.
4. The exposed resist is removed in a developement step.
5. A thin layer of gold is evaporated onto the wafer.
6. The electron resist is removed from the sample during a lift-off process, leaving only the gold particles directly in contact with the wafer. This results in a pattern of small gold droplets.
7. The wafer is cleaned in HF, before being loaded into the MBE system, where indium and arsenide particles gather under the gold droplets and form the nanowires.

NB: This is a simplified description of the full MBE nanowire growth process.

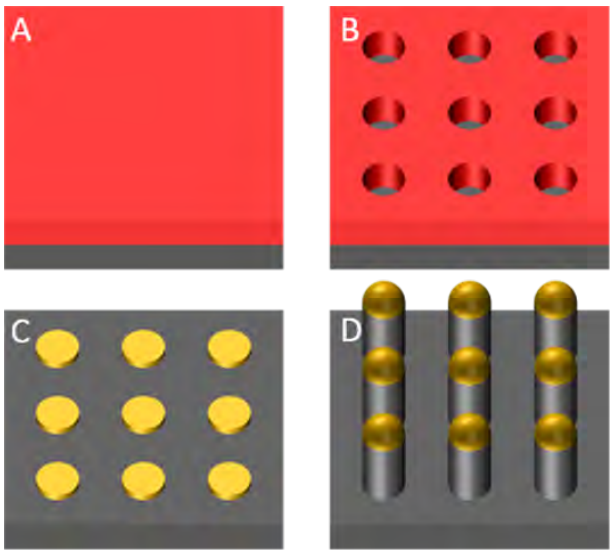

Figure 9.2: Sketch of the sample after different fabrication process steps. (A) Spin coating of electron resist onto sample. (B) Electron beam lithography and development. (C) Gold evaporation and lift-off. (D) Nanowires grown by molecular beam epitaxy.

Since most of (if not all) of the process in MBE can be tailored to produce periodic structures on the sample, scatterometry might be suitable for this characterization, given that the structure has a distinguishable optical fingerprint in an experimental configuration. It is therefore interesting to investigate if we can find a scatterometry hardware configuration suitable to perform scatterometry on nanowires. Four

fabrication steps which might be ideal for scatterometry are sketched in figure 9.2. This corresponds to a characterization after step 2, step 4, step 6 and step 7 in the box above. It should be noted that the characterization of these steps must be fast enough to avoid bottle-necks between process steps in order to be considered for implementation in a production line, but for deployment at an agile research facility, flexibility is usually preferred over speed.
In order to test if scatterometry would be suitable for characteriation of the different process steps, a compact imaging scatterometer based on the commercial tuneable Lyot filter was build and transported to the University of Copenhagen. Here the system was used to perform scatterometry in-between selected process steps. This system uses the same hardware as the imaging system described in paper 1. First, an InAs two inch quarter wafer was cleaned in HF-acid and an electron resist (PMMA) was spin coated onto the wafer. After the spin coating step, the sample is simply modeled as a thinfilm of PMMA described only by the height (or thickness) of the film. A reconstruction of the resist height can be seen on figure 9.3. χ^2 has been plotted as a function of the height, and a unique solution is clearly found. Here we do not have a reference measurement, but we do however find a height close to the value of 195 nm expected by the fabrication staff.

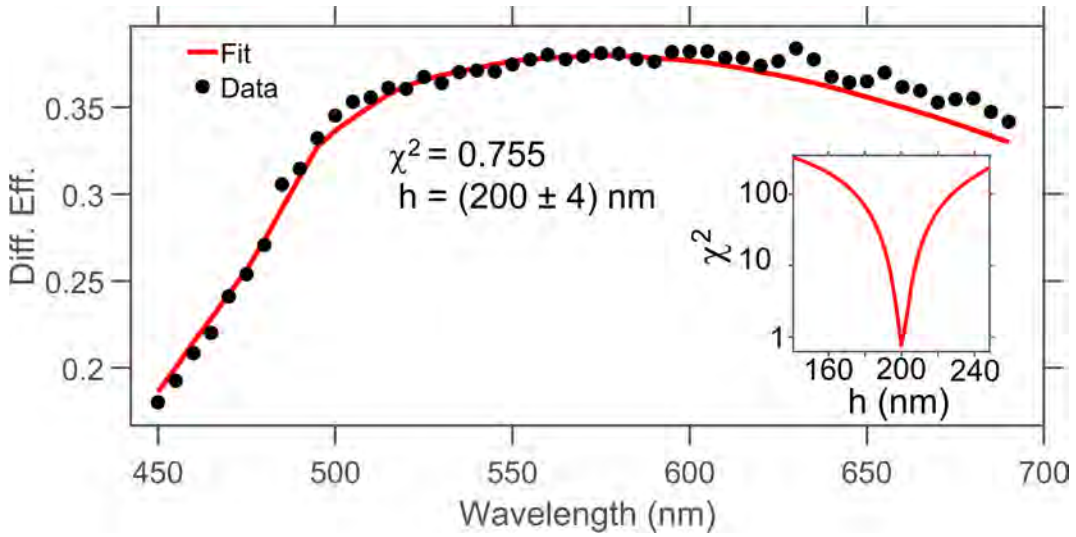

Figure 9.3: Reconstruction of layer height of PMMA spin coated onto the wafer. A good agreement between data (black dots) and best fitting model (red line) is found. The insert shows χ^2 as a function of the simulated height. It can be seen that a unique solution is found at h = 200.

After the successful spin coating, holes with a period of one micron were written in the electron resist using EBL. After the EBL step, the sample was developed to remove the exposed resist. This sample is modeled as pillars of air surrounded by PMMA. A reconstruction of the sample can be seen in figure 9.4. It is noted that the optical signal is more sensitive to changes in the height rather than changes in the width. The found values are also in agreement with what is expected by the fabrication staff. Since SEM measurements of the holes would be damaging to the resist, a reference measurement of the width was not performed. The height is in agreement with what was found in the previous step.

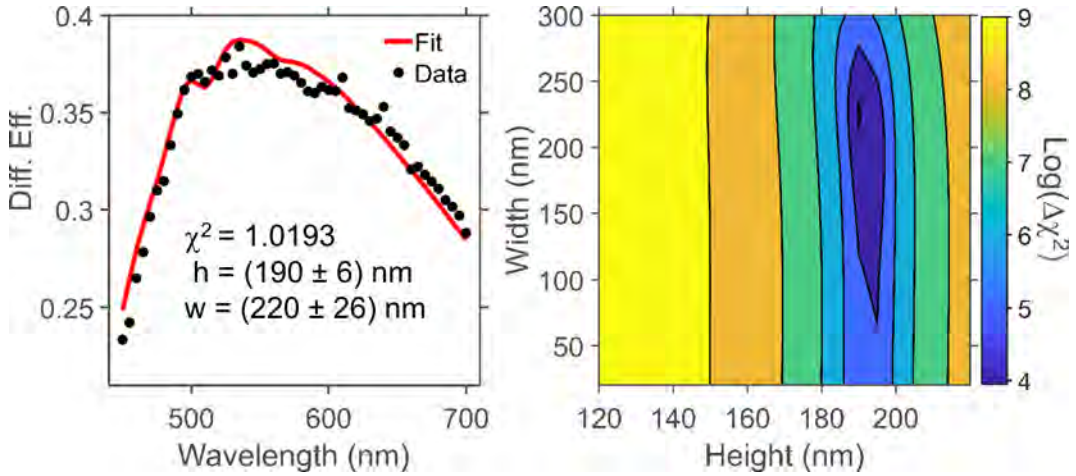

Figure 9.4: Reconstruction of the holes written into the electron resist. (left) data, best fit and parameters for the best fitting model. (right) goodness of fit as a function of model parameters.

After the EBL step, the sample was argon milled to slightly reduce the amount of resist, and gold was evaporated onto the sample. After gold evaporation, a lift-off process was performed to remove the resist and gold not directly in contact with the wafer. An SEM image of the sample after lift-off can be seen in the left part

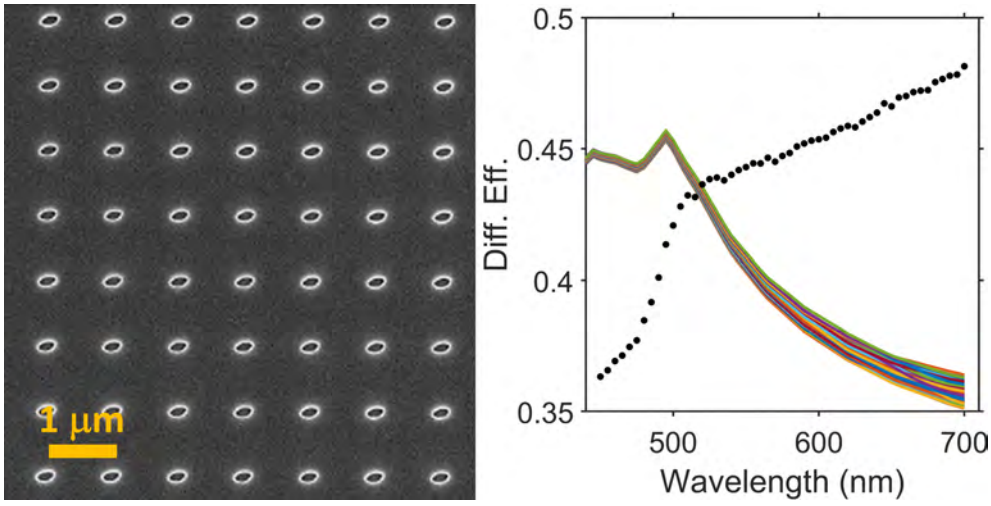

Figure 9.5: Sample after lift-off. (left) SEM image of the gold droplets deposited on the substrate. (right) colored lines show simulated signals with heights varying from 6 nm to 14 nm and widths ranging from 20 nm to 300 nm. The blacks dots shows the measured signal. The disagreement between data and theory stands out here.

of figure 9.5. The area of each disk is found, from the SEM images, and the width is found by approximating them as circles ($A = \pi(\frac{w}{2})^2$). The mean width of the circles is found to be 167 nm with a standard deviation of 7 nm. This value is lower than expected based on the results from the measurements on the patterned resist. To the right in figure 9.5, the fully drawn lines show simulated optical responses for heights varying from 6 nm to 14 nm and widths ranging from 20 nm to 300 nm. It is evident that we have a very little change in the simulated signal as a function of the

structural parameters. The simulated signals are almost identical to the reflection of plain InAs, meaning that discs of a few nanometers in thickness have little influence on how visible light interacts with the sample at normal incidence. The measured signal (black dots) does not resemble the expected signal at all. This was believed to be a problem with the simulations rather than a defect in the sample. This hypothesis was support by literature reporting a slow convergence of gold structures in RCWA [72].
Due to time constraints, this was not further investigated before the prepared substrate was placed in the MBE chamber. The wires after the MBE step can be seen in figure 9.6. Parasitic growth on the substrate is observed. The wires are not very homogeneous and have defects at the tops, which are larger than expected. The wires are thinner and shorter than expected, this is believed to be caused by a large amount of the InAs deposited ending up on the substrate.

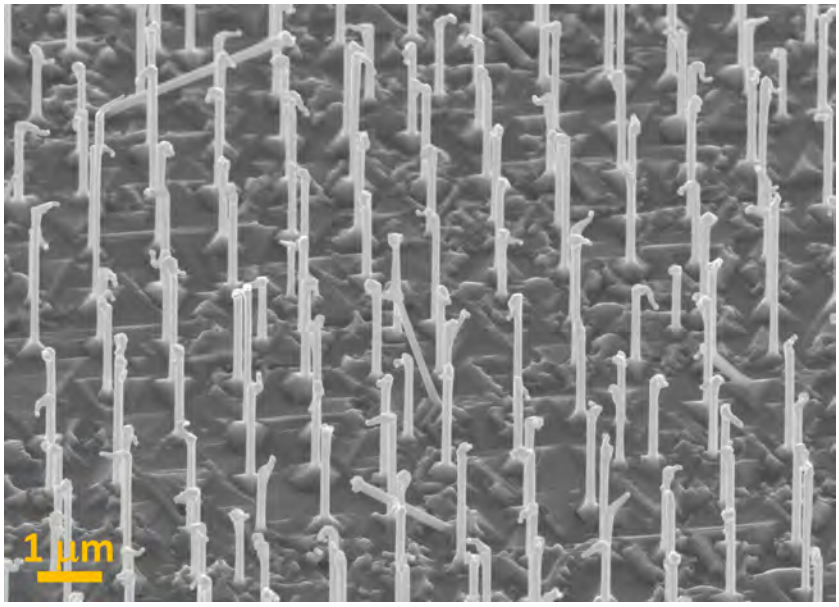

Figure 9.6: Final wires after the MBE step. The substrate is subject to a large amount of parasitic growth and the wires are not very homogeneous.

After further examination of the SEM images acquired after lift-off and discussions with the staff at QDev, it was discovered that the milling step had been too aggressive, and most, if not all, of the resist was removed. Furthermore, shallow holes were created where the substrate was exposed. This is believed to have resulted in a sample sketched in figure 9.7. Since the reflected signal resembles a mix between Au and InAs, with more Au than InAs, we believe that gold has been present all over the sample, although we can not confirm how the sample actually looked in between Argon milling and MBE.

Unfortunately the final wires are not suitable for a scatterometry analysis since too many parameters would be needed to describe the complex geometry. This section does, however, highlight the importance of reliable process control in the fabrication. If we had been more confident in the scatterometer results after the lift-off process, we could have discarded the sample and started preparing a new wafer, and thus

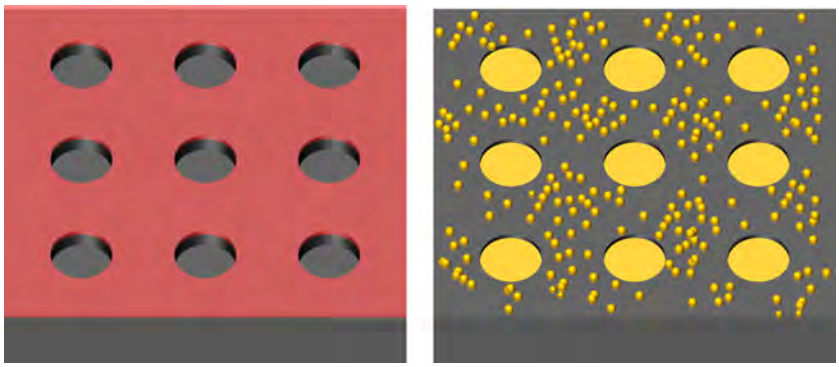

Figure 9.7: A guess of how the sample looked after Argon milling. (left) Before gold evaporation and (right) after gold evaporation and lift-off. Gold atoms are present on the entire sample and droplets are collected at the holes in the substrate.

saved the expensive MBE step for a well prepared sample. It can be concluded that even though gold droplets might be hard to characterize with high precision using the presented setup, it is very clear when something has gone completely wrong. This also showed us that it would be ideal to implement another measurement after or during the Argon milling. Based on this field test it is concluded that scatterometry would be ideal to monitor the different process steps in nanowire fabrication.

9.2 Scatterometry on Nanowires

For a second experiment, nanowires grown by MBE at QDev were transported to DFM for characterization. The main goal here was to establish if scatterometry can be used to characterize the finalized wires. A final characterization step is already performed by sampled SEM measurements. If this characterization could be done by scatterometry, it would, at the very least, be a convenience improvement to the nanowire fabrication activities, since it would be much faster and circumvent the need for the sample to be placed in vacuum.

An SEM image of fabricated wires investigated in this section can be seen in figure 9.8. From figure 9.8 the following is gathered: The wires have a width of

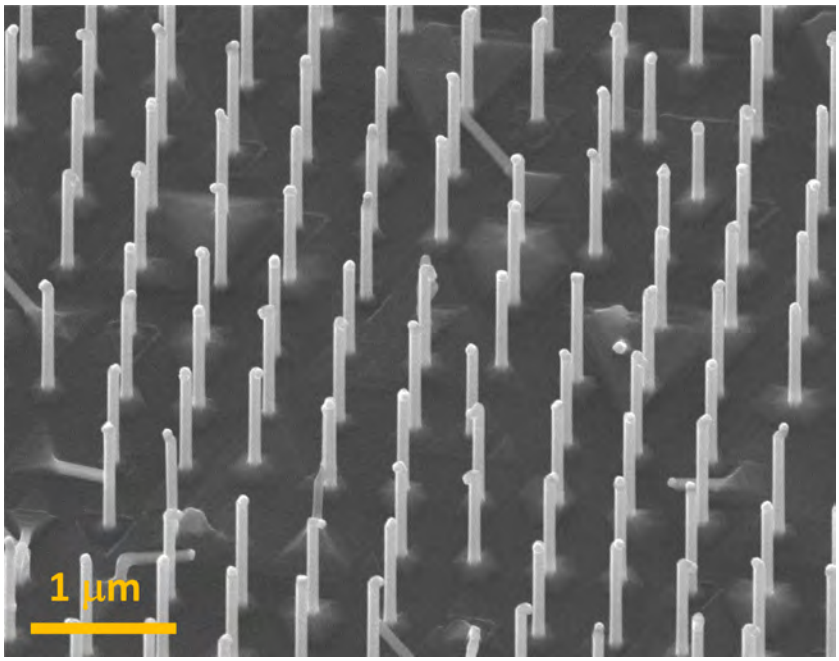

Figure 9.8: SEM image of nanowires in a 2D array. The two grating periods are both 500 nm and perpendicular. SEM images acquired by Miķelis Marnauza.

approximately 70 nm and a height of 1200 nm. Furthermore, it is observed that the wires have a "beak" at the top, and are placed on a "base". It is assumed, that the direction of the beak is random, and that the optical responses of the beaks average out so they can be ignored in the optical simulations. The base is included in the modeling as a truncated cone. The parasitic growth and tipped/missing wires are not included in the first iteration of simulations. The yield of perfect wires is estimated to be around 95% based on the SEM imaging.

The wire and the base are assumed to be well approximated by circular structures. A sketch of the simulated structure can be seen in figure 9.9.
The parameters w_{wire}, h_{wire}, $w_{\text{base-bottom}}$ and h_{base} are all varied in the simulations, while the parameters Γ_x and Γ_y are locked to 500 nm. The parameter $w_{\text{base-bottom}}$ is locked to the width of the wire for simplicity.

20 rectangular slabs are used to approximate cylinders. The base is approximated by

five cylinders, while the wire part is a single cylinder. The Fourier series is truncated by retaining 19 diffraction orders in the simulations. The sample was measured us-

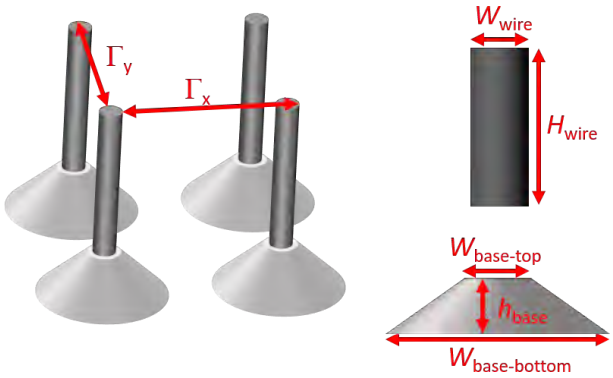

Figure 9.9: (left) Simulated structure. The structures are not drawn to scale. (right) Explanation of the model parameters used in the simulation.

ing an LDLS light source (Energetic, EQ-99X) giving a broad wavelength range. The light was s-polarized with respect to the sample plane before impinging on the sample at a 50 degree angle of incidence. The specular reflection was passed through another polarizer, to remove the a possible signal from depolarizing effects, before it was collected by a spectrometer (Ocean Optics, FLAME-S-XR1-ES). The reference measurement was taken on a flat piece of Si100. The dark measurement was taken with the light source blocked.

A reconstruction of the nanowires can be seen in figure 9.10. The fit finds the general features of the signal, but can still be optimized by adding parameters to describe the wires. The best fitting model finds height and width values which are in good agreement with the SEM measurements. The parameter h_{base} is hard to evaluate based on the SEM image, and the parameter $w_{\text{base-bottom}}$ seems a little high, but not unreasonable compared to the SEM images ($w_{\text{base-bottom}} = (291 \pm 20)$ nm, measured using the SEM image). The discrepancies between data and simulation might be a result of parasitic growth or wires falling onto the substrate. It was attempted to use the semi-analytical model described in Paper 4, to account for the defects. This did however not work well. This is not too surprising since the defects are believed to be associated with the substrate. In the paper, it was shown that the semi-analytical model was not capable of treating substrate defects. Based on the reconstruction in figure 9.10, we continue towards imaging scatterometry measurements of the nanowires. For this purpose the custom Lyot filter from Chapter 5 is tested and used as described in the next section.

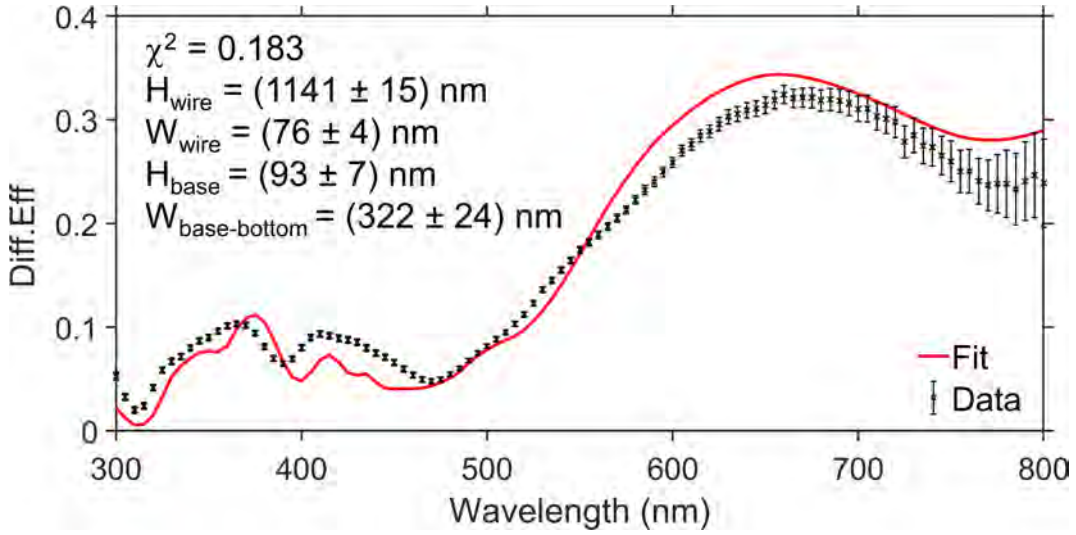

Figure 9.10: Measured diffraction efficiencies (black crosses) and simulated diffraction efficiencies (red line). The model parameters for the best fitting model can be seen in the upper left corner.

9.3 Imaging Scatterometry on Nanowires

Using the custom Lyot filter, images of the sample were acquired for different wavelengths. To use the full dynamic range of the camera, different exposure times was used for the different images. These exposure times are tabulated in table 9.1. Summing up the exposure times, we seen that the total camera time is typically just under 30 seconds. Since the software and filter switching times are small compared to this value, a measurement series can be performed in well under a minute. An

λ (nm)	422	450	492	532	570	610	630	660	680	720	750	770
T (ms)	2529	1647	1328	1219	2538	2204	2018	1527	2182	3200	7451	1890

Table 9.1: Exposure times, T, of the images acquired at different nominal wavelengths.

image of the sample, taken at a nominal wavelength of 630 nm, can be seen in figure 9.11. We can clearly see several artifacts on the image. Some of these arise from sample defects, and others from defect or particles on the filter or camera. It is believed that the ripples seen on the image are caused by impurities at the different interfaces in the filter.

For the first reconstruction, all parameters have been locked with the exception of the wire height, based on the results seen in figure 9.10. It is observed that the nanowire array is subdivided into 17 by 17 boxes. These boxes are believed to be a result of the write field during the EBL step, as literature suggest that structures at the edges of the write field ends up with a lower fidelity [73]. This effect was also observed on the sample from the previous section after the EBL step. Within these boxes heights between 1100 nm and 1200 nm are found (excluding the static height of the base locked at 93 nm). This value is in excellent agreement with the SEM images. At the edges of these boxes a larger height is typically found (between 1500 nm and 1700 nm). Reconstructions from pixels within defects are also seen to find a different height. These heights are not physical, but rather a symptom of inability

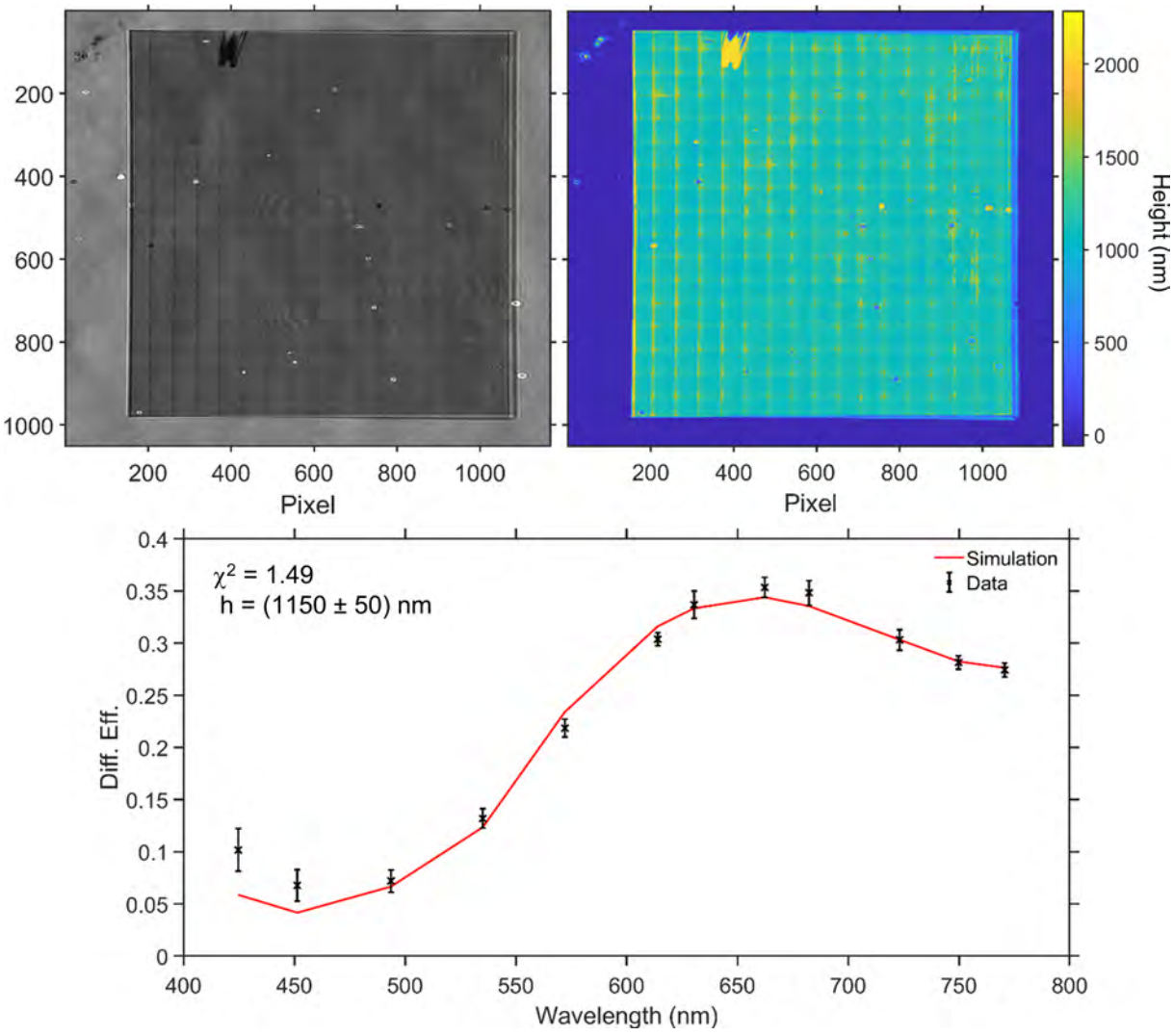

Figure 9.11: (top left) Image of the nanowire array. (top right) Reconstruction of the height for all pixels in the image. The first axis has been stretched to correct for the off axis recording of the image. (bottom) Data and best fitting model for a single pixel in the center. A good agreement between simulated and measured data is found.

to fit to the selected model.
Based on the reconstruction of the height, a larger database was made allowing the width to range from 60 nm to 100 nm in steps of 4 nm. Using this database, the same data was used to reconstruct the height and the width simultaneously, and the results are shown in figure 9.12. The write fields are still evident from this reconstruction. The reconstructed heights are in fairly good agreement with previous results, but a clear correlation between the height and width is found (areas reconstructing a large height tends to reconstruct a low width and vice versa).

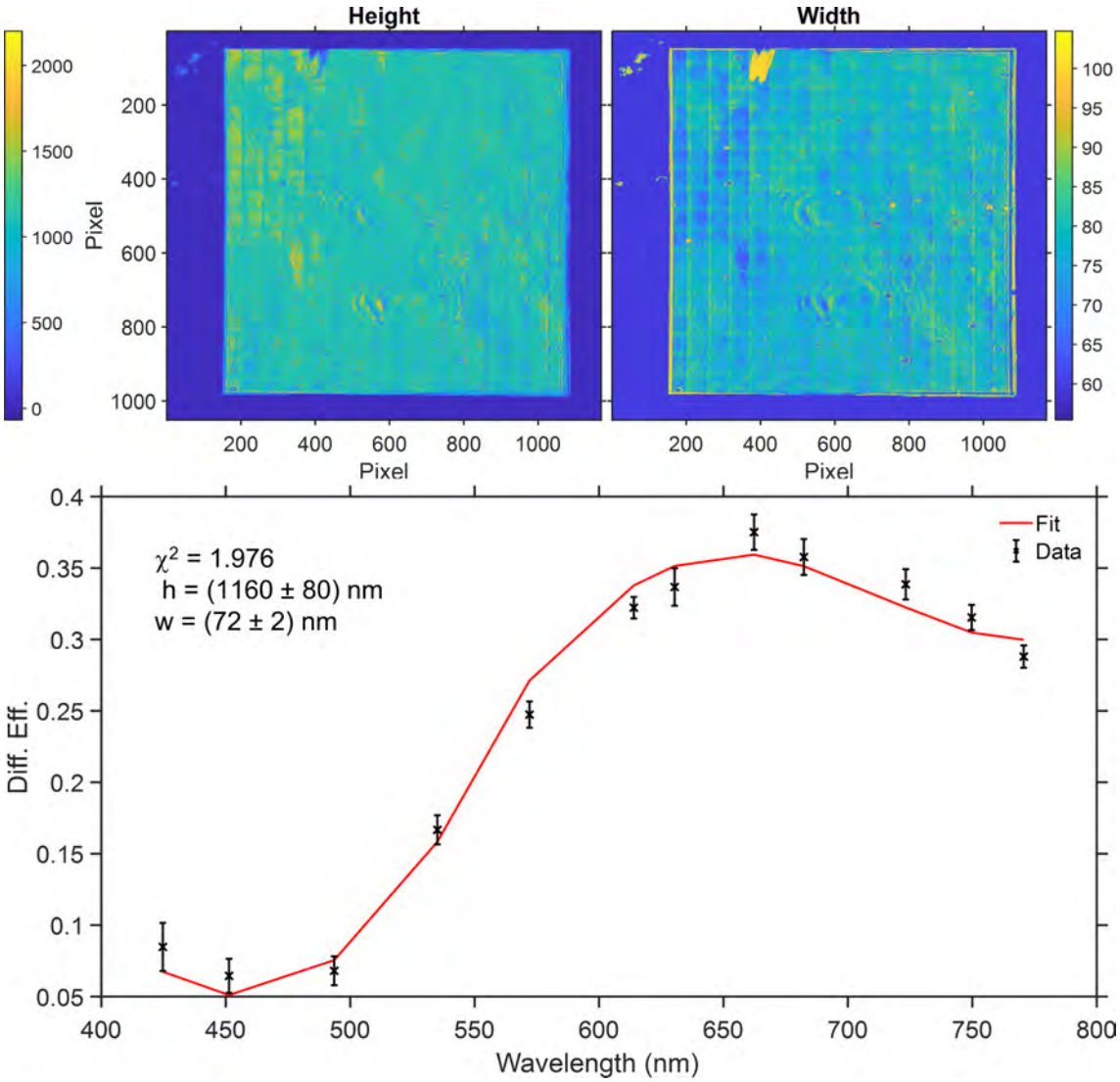

Figure 9.12: Reconstruction of two parameters simultaneously. (top left) Reconstruction of the height for all pixels in the image. (top right) reconstruction of the width for all pixels in the image. The scale bar for both images are in units of nm. (bottom) Data and best fitting model for a single pixel in the center. A good agreement between simulated and measured data is found.

Since we can determine the height with a locked width, but not safely reconstruct the height and the width, a natural next step is to use the SEM data in the reconstruction as demonstrated in Chapter 8. Doing so, the chi-square to optimize becomes:

$$\chi^2 = \frac{1}{2}\left(\frac{(h_{\mathrm{SEM}} - h^c)^2}{\sigma_h^2} + \frac{(w_{\mathrm{SEM}} - w^c)^2}{\sigma_w^2}\right) + \frac{1}{N}\sum_i^N \frac{(\eta_i - \eta_i^c)^2}{\sigma(\eta_i)^2} \tag{9.1}$$

where h_{SEM} and w_{SEM} is the height and width found by the SEM measurements, σ_h and σ_w is the uncertainties on the height and the width of the SEM measurements and h^c and w^c are the calculated heights and widths from the RCWA calculations. Using this approach, the determination of the height using a locked width would correspond to a regularization where $\sigma_h \to \mathrm{inf}$ and $\sigma_w \to 0$. h_{SEM} and w_{SEM} is set to be 1200 nm and 70 nm respectively, based on the SEM image in figure 9.8. However, since the uncertainty associated with the SEM images is not well-known, different values of uncertainties are investigated by looking at a sub-section of the whole array, namely the top left corner. This area is selected, since the heights reconstructed here tends to be larger than expected. The reconstructed height for different estimates of the SEM uncertainties can be seen in figure 9.13. It is evident that the uncertainties of the SEM measurements have a large impact on the reconstruction.

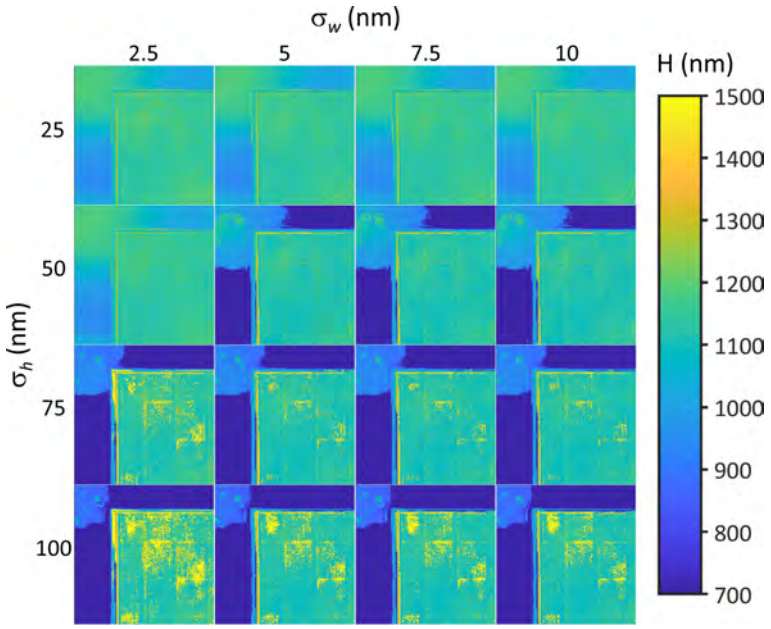

Figure 9.13: Reconstructions of the height from the top left corner of the nanowire array for different estimates of the SEM uncertainties.

The regularization should be just strong enough to suppress noise (we should not see a large deviation of structures within a write field) without losing information of the sample (i.e. areas without structures and physical structures such as those believed to originate from the write field should still be visible). We see that the regularization of the height has the biggest impact, while regularization of the width only changes the results notably in the extreme case $\sigma_w = 2.5$ nm. From the figure it can be seen that a height regularization using $\sigma_h = 25$ nm, overregulates and it becomes hard to distinguish areas with and without structures. This suggests that

the combination of height variance and uncertainty on the height measurements on SEM surpasses 25 nm. Using $\sigma_h = 100$ nm has little effect on the reconstructed height. This could mean two things: The uncertainty of the SEM measurements is smaller than 100 nm or that the scatterometer is more sensitive to the height than measured by the SEM. It is likely that both of the above statements are true. Based on figure 9.13 it is assumed that $\sigma_h = 50$ nm and σ_w is in the 5-8 nm range. Ideally, the reconstruction would be more beneficial if it could be used solely on scatterometry data. However, since scatterometry measurements are fast, it might be opted to do SEM on a few sampled areas of a large sample and then do a scatterometry analysis for the entire sample. This would work as a fast way of screening a macroscopic array of nanowires within minutes.
In addition, one could use the image in combination with simple image recognition software to identify areas where growth was intended (In this specific case a square of area 5×5 mm^2), and use this information to find defects automatically.
Based on these results, it is concluded that the imaging scatterometer is suitable for a screening of large, dense arrays of nanowires, given some a priori information.
Future work will emphasize an extension of the wavelength range of the Lyot filter. A problem to overcome is to separate the peaks in the UV region. Based on simulations, this can be solved by using another plate with thickness of 1.25 mm. Given a broader spectrum with more measurement points, it is believed that we can reconstruct nanowire samples without the need of additional regularizations.

Chapter 10

Conclusion and Outlook

This thesis describes a selection of the scatterometry activities at DFM. The focus has been on the emerging industries of plastic nanostructures and nanowires.
A study comparing conventional spectroscopic scatterometry and imaging scatterometry with state of the art measurement techniques have been conducted. Here it was found that the scatterometers were in agreement with AFM measurements. Methods to replace conventional scatterometry libraries using neural networks or semi-analytical models are developed. This allows for a characterization of different sample defects, at a reduced RCWA calculation time.
The work with nanostructured plastic demonstrates that scatterometry can be used for in-line characterization of injection molded nanostructures in bulk plastic products and have been used to characterize over 250 samples. The developed instrument showed an excellent agreement with AFM and SEM measurements. It was used to optimize an existing fabrication recipe and used to create a new one at the fabrication site. An imaging scatterometer capable of measuring a full two-inch disc was build and demonstrated, where areas down to tens of square microns can be analyzed with nanometer precision. This technique can be further improved by applying image recognition techniques to automate the process of area selection. Based on this work it is concluded that scatterometry has the potential to become an essential technique for quality control or process optimization in the production of nanostructured plastic parts.
Further work will emphasize on adapting imaging scatterometry for in-line control of even faster production techniques such as roll-to-roll. Here the bottle-neck for the imaging system is the acquisition time. It is currently attempted to use a camera and a spectrograph as a line-scan-camera. By moving the sample perpendicular to the spatial recording direction, a hyper-spectral image can be recorded as the sample is transported on a roll or conveyor belt.
A method to combine different measurement techniques, namely scatterometry, ellipsometry, and AFM, in the inverse modeling has been demonstrated. This allows for more robust reconstruction of a sample with a complex structure.
In this thesis, it has been demonstrated that scatterometry can be used to characterize different steps in the fabrication of nanowires. This gives the user immediate feedback on the completed step before moving on and can thus be used to avoid errors early in a long process chain. Characterizing the final wires can be done using conventional spectroscopic scatterometry given an array of wires larger than the beam spot and a suitable illumination/detection wavelength range. When us-

ing imaging scatterometry, the characterization becomes more challenging due to the reduced information. A Lyot filter has been constructed to enhance the measurement capabilities of the imaging scatterometer system. This filter improves the signal and wavelength range of the system. It was, however, found that a further increase in the wavelength range would improve the robustness of the reconstruction. To increase the wavelength range, new waveplates have been ordered to separate the transmission peaks in the low wavelength regime. A new polishing method has been found to reduce the surface roughness of the plates in the Lyot filter and in turn, increase the transmission, especially at lower wavelengths. It is believed that the added sensitivity gained from the UV-region will make it possible to reliably reconstruct nanowires using imaging scatterometry. It is concluded, that even at this current state of the imaging scatterometer it can still be used to detect defects in the fabricated nanowires. In the future, we will also investigate the possibilities of using imaging scatterometry with a high numerical aperture. Here the angular spectrum from a small area might be used to reconstruct single wires. As the trends of IoT move overtake production facilities, the neural network approach becomes increasingly interesting, with the increased amount of generated data. Here the key requirement is that one can feed a network with sufficient data. Exploiting this, one can further decrease the time of the inverse modeling part for complex samples. As shown in chapter Chapter 8 and Chapter 9 increasing the amount of data in the inverse modeling makes for more robust reconstructions. Based on the achieved results, it is concluded that scatterometry can be used for high-throughput metrology of nanostructured plastic surfaces, and the different process steps in nanowire fabrication.

References

[1] T. D. Cope, "The rittenhouse diffraction grating," *Journal of the Franklin Institute*, vol. 214, pp. 99–104, July 1932.

[2] T. Young, "II. The Bakerian Lecture. On the theory of light and colours," *Philosophical Transactions of the Royal Society of London*, vol. 92, pp. 12–48, Jan. 1802.

[3] C. J. Raymond, "Metrology of subwavelength photoresist gratings using optical scatterometry," *Journal of Vacuum Science & Technology B: Microelectronics and Nanometer Structures*, vol. 13, p. 1484, July 1995.

[4] M. H. Madsen and P.-E. Hansen, "Scatterometry—fast and robust measurements of nano-textured surfaces," *Surface Topography: Metrology and Properties*, vol. 4, pp. 023003–023028, Apr. 2016.

[5] C. E. W and P. D. P, "Method and apparatus for measuring the profile of small repeating lines," Jan. 2019.

[6] X. Y and A. I, "Spectroscopic scatterometer system," 2002.

[7] D. B. A. J and D. M, "Inspection apparatus and method of inspection," 2008.

[8] K. K. Mehta and R. J. Ram, "Precise and diffraction-limited waveguide-to-free-space focusing gratings," *Scientific Reports*, vol. 7, Dec. 2017.

[9] J. Filevich, K. Kanizay, M. C. Marconi, J. L. A. Chilla, and J. J. Rocca, "Dense plasma diagnostics with an amplitude-division soft-x-ray laser interferometer based on diffraction gratings," *Optics Letters*, vol. 25, p. 356, Mar. 2000.

[10] H. Cen and Y. He, "Theory and application of near infrared reflectance spectroscopy in determination of food quality," *Trends in Food Science & Technology*, vol. 18, pp. 72–83, Feb. 2007.

[11] J.-L. Kou, M. Ding, J. Feng, Y.-Q. Lu, F. Xu, and G. Brambilla, "Microfiber-Based Bragg Gratings for Sensing Applications: A Review," *Sensors*, vol. 12, pp. 8861–8876, June 2012.

[12] X. Feng, R. Su, T. Happonen, J. Liu, and R. Leach, "Fast and cost-effective in-process defect inspection for printed electronics based on coherent optical processing," *Optics Express*, vol. 26, p. 13927, May 2018.

[13] M. Born and E. Wolf, *Principles of optics: electromagnetic theory of propagation, interference and diffraction of light*. Cambridge ; New York: Cambridge University Press, 7th expanded ed ed., 1999.

[14] M. H. Madsen and P.-E. Hansen, "Imaging scatterometry for flexible measurements of patterned areas," *Optics Express*, vol. 24, p. 1109, Jan. 2016.

[15] M. Calaon, M. H. Madsen, J. Weirich, H. N. Hansen, G. Tosello, P. E. Hansen, J. Garnaes, and P. T. Tang, "Replication fidelity assessment of large area sub-u m structured polymer surfaces using scatterometry," *Surface Topography: Metrology and Properties*, vol. 3, p. 045005, Sept. 2015.

[16] J. W. Goodman, *Introduction to Fourier optics*. Englewood, Colo: Roberts & Co, 3rd ed ed., 2005. OCLC: ocm56632414.

[17] J. E. Harvey, C. L. Vernold, A. Krywonos, and P. L. Thompson, "Diffracted radiance: a fundamental quantity in nonparaxial scalar diffraction theory," *Applied Optics*, vol. 38, pp. 6469–6481, Nov. 1999.

[18] M. G. Moharam, T. K. Gaylord, D. A. Pommet, and E. B. Grann, "Stable implementation of the rigorous coupled-wave analysis for surface-relief gratings: enhanced transmittance matrix approach," *Journal of the Optical Society of America A*, vol. 12, p. 1077, May 1995.

[19] J. J. Hench and Z. STRAKOvS, "The RCWA method-a case study with open questions and perspectives of algebraic computations," *Electronic Transactions on Numerical Analysis*, vol. 31, pp. 331–357, 2008.

[20] J. C. M. Garnett, "Colours in Metal Glasses and in Metallic Films," *Philosophical Transactions of the Royal Society A: Mathematical, Physical and Engineering Sciences*, vol. 203, pp. 385–420, Jan. 1904.

[21] D. A. G. Bruggeman, "Berechnung verschiedener physikalischer Konstanten von heterogenen Substanzen. I. Dielektrizitätskonstanten und Leitfähigkeiten der Mischkörper aus isotropen Substanzen," *Annalen der Physik*, vol. 416, no. 7, pp. 636–664, 1935.

[22] Kane Yee, "Numerical solution of initial boundary value problems involving maxwell's equations in isotropic media," *IEEE Transactions on Antennas and Propagation*, vol. 14, pp. 302–307, May 1966.

[23] A. Taflove and S. C. Hagness, *Computational electrodynamics: the finite-difference time-domain method*. Artech House antennas and propagation library, Boston: Artech House, 3rd ed ed., 2005.

[24] "Understanding the FDTD Method."

[25] T. Delort and D. Maystre, "Finite-element method for gratings," *Journal of the Optical Society of America A*, vol. 10, pp. 2592–2601, Dec. 1993.

[26] R. Barlow, *Statistics: a guide to the use of statistical methods in the physical sciences*. The Manchester physics series, Chichester, England ; New York: Wiley, 1989.

[27] W. H. Press, ed., *Numerical recipes in C++: the art of scientific computing*. Cambridge, UK ; New York: Cambridge University Press, 2nd ed ed., 2002.

[28] E. Agocs, B. Bodermann, S. Burger, G. Dai, J. Endres, P.-E. Hansen, L. Nielson, M. H. Madsen, S. Heidenreich, M. Krumrey, B. Loechel, J. Probst, F. Scholze, V. Soltwisch, and M. Wurm, "Scatterometry reference standards to improve tool matching and traceability in lithographical nanomanufacturing," p. 955610, Aug. 2015.

[29] J. Levesley, I. Anderson, J. Mason, H. U. G. B. S. O. COMPUTING, and MATHEMATICS., *Algorithms For Approximation IV. Proceedings of the 2001 International Symposium.* AD-a412 833, huddersfield univ (united kingdom) school of computing and mathematics, p. 170-186, 2002.

[30] K. Levenberg, "A method for the solution of certain non-linear problems in least squares," *Quarterly of Applied Mathematics*, vol. 2, pp. 164–168, July 1944.

[31] D. W. Marquardt, "An Algorithm for Least-Squares Estimation of Nonlinear Parameters," *Journal of the Society for Industrial and Applied Mathematics*, vol. 11, pp. 431–441, June 1963.

[32] V. A. Ukraintsev, "A comprehensive test of optical scatterometry readiness for 65-nm technology production," p. 61521G, Mar. 2006.

[33] P.-E. Hansen, M. H. Madsen, J. Lehtolahti, and L. Nielsen, "Traceable Mueller polarimetry and scatterometry for shape reconstruction of grating structures," *Applied Surface Science*, vol. 421, pp. 471–479, Nov. 2017.

[34] P. Boher, M. Luet, T. Leroux, J. Petit, P. Barritault, J. Hazart, and P. Chaton, "Innovative rapid photogoniometry method for CD metrology," (Santa Clara, CA), p. 1302, May 2004.

[35] M. H. Madsen, P. Boher, P.-E. Hansen, and J. F. Jørgensen, "Alignment-free characterization of 2d gratings," *Applied Optics*, vol. 55, p. 317, Jan. 2016.

[36] E. S. for Precision Engineering and Nanotechnology, *Proceedings of the 16th International Conference of the European Society for Precision Engineering and Nanotechnology: May 30th-3rd June 2016, Nottingham, UK.* Bedford, UK: Euspen, 2016. OCLC: 952090092.

[37] B. Lyot, "Optical apparatus with wide field using interference of polarized light," *C. R. Acad. Sci. Paris 197*, p. 1593, 1933.

[38] R. C. Jones, "A New Calculus for the Treatment of Optical SystemsI Description and Discussion of the Calculus," *Journal of the Optical Society of America*, vol. 31, p. 488, July 1941.

[39] A. M. Title and W. J. Rosenberg, "Tunable Birefringent Filters," *Optical Engineering*, vol. 20, Dec. 1981.

[40] D. Wierzbicki and M. Wiliam, "Liquid crystal tunable filters in detecting water pollution," Vilnius Gediminas Technical University Press "Technika" 2014, 2014.

[41] M. H. Madsen, P.-E. Hansen, M. Zalkovskij, M. Karamehmedović, and J. Garnæs, "Fast characterization of moving samples with nano-textured surfaces," *Optica*, vol. 2, p. 301, Apr. 2015.

[42] K. Pathakoti, M. Manubolu, and H.-M. Hwang, "Nanostructures: Current uses and future applications in food science," *Journal of Food and Drug Analysis*, vol. 25, pp. 245–253, Apr. 2017.

[43] M. Zalkovskij, L. H. Thamdrup, K. Smistrup, T. Andén, A. C. Johansson, N. J. Mikkelsen, M. H. Madsen, J. Garnæs, T. T. Kristiansen, M. Diemer, M. Døssing, D. Minzari, P. T. Tang, A. Kristensen, R. Taboryski, S. Essendrop, T. Nielsen, and B. Bilenberg, "Smart plastic functionalization by nanoimprint and injection molding," p. 94230T, Mar. 2015.

[44] D. Dimla, M. Camilotto, and F. Miani, "Design and optimisation of conformal cooling channels in injection moulding tools," *Journal of Materials Processing Technology*, vol. 164-165, pp. 1294–1300, May 2005.

[45] T. A. Osswald, L.-S. Turng, and P. J. Gramann, eds., *Injection molding handbook*. Munich : Cincinnati: Carl Hanser Publishers ; Hanser Gardner Publications, 2nd ed., updated 2nd ed ed., 2008. OCLC: ocn170057853.

[46] D. Freedman, R. Pisani, and R. Purves, *Statistics*. New York: W.W. Norton & Co, 4th ed ed., 2007. OCLC: ocm76142955.

[47] H. Goldstein, C. P. Poole, and J. L. Safko, *Classical mechanics*. San Francisco, NJ: Addison Wesley, 3. ed ed., 2002. OCLC: 248389949.

[48] P. R. Bevington and D. K. Robinson, *Data reduction and error analysis for the physical sciences*. Boston: McGraw-Hill, 3rd ed ed., 2003.

[49] J. Hadamard, "Sur les problèmes aux dérivées partielles et leur signification physique," *Princeton University Bulletin*, pp. 49–52, 1902.

[50] A. E. Hoerl and R. W. Kennard, "Ridge Regression: Biased Estimation for Nonorthogonal Problems," *Technometrics*, vol. 12, pp. 55–67, Feb. 1970.

[51] C. M. Bishop, *Neural networks for pattern recognition*. Oxford : New York: Clarendon Press ; Oxford University Press, 1995.

[52] H.-T. Huang and F. L. Terry Jr, "Spectroscopic ellipsometry and reflectometry from gratings (Scatterometry) for critical dimension measurement and in situ, real-time process monitoring," *Thin Solid Films*, vol. 455-456, pp. 828–836, May 2004.

[53] A. Rothen, "The Ellipsometer, an Apparatus to Measure Thicknesses of Thin Surface Films," *Review of Scientific Instruments*, vol. 16, pp. 26–30, Feb. 1945.

[54] M. Ohring, "Characterization of Thin Films and Surfaces," in *Materials Science of Thin Films*, pp. 559–640, Elsevier, 2002.

[55] B. Cappella and G. Dietler, "Force-distance curves by atomic force microscopy," *Surface Science Reports*, vol. 34, pp. 1–104, Jan. 1999.

[56] K. Kuchuk, I. Schlesinger, and U. Sivan, "Autopilot for frequency-modulation atomic force microscopy," *Review of Scientific Instruments*, vol. 86, p. 103703, Oct. 2015.

[57] C. Bohling and W. Sigmund, "Self-Limitation of Native Oxides Explained," *Silicon*, vol. 8, pp. 339–343, July 2016.

[58] T. D. Ladd, F. Jelezko, R. Laflamme, Y. Nakamura, C. Monroe, and J. L. O'Brien, "Quantum computers," *Nature*, vol. 464, p. 45, Mar. 2010.

[59] B. Schumacher, "Quantum coding," *Physical Review A*, vol. 51, pp. 2738–2747, Apr. 1995.

[60] H. Park and K. B. Crozier, "Multispectral imaging with vertical silicon nanowires," *Scientific Reports*, vol. 3, Dec. 2013.

[61] S. Nadj-Perge, S. M. Frolov, E. P. A. M. Bakkers, and L. P. Kouwenhoven, "Spin–orbit qubit in a semiconductor nanowire," *Nature*, vol. 468, p. 1084, Dec. 2010.

[62] A. Kringhøj, L. Casparis, M. Hell, T. W. Larsen, F. Kuemmeth, M. Leijnse, K. Flensberg, P. Krogstrup, J. Nygård, K. D. Petersson, and C. M. Marcus, "Anharmonicity of a superconducting qubit with a few-mode Josephson junction," *Physical Review B*, vol. 97, Feb. 2018.

[63] G. W. Winkler, D. Varjas, R. Skolasinski, A. A. Soluyanov, M. Troyer, and M. Wimmer, "Orbital Contributions to the Electron g Factor in Semiconductor Nanowires," *Physical Review Letters*, vol. 119, July 2017.

[64] M. A. Herman and H. Sitter, *Molecular Beam Epitaxy: Fundamentals and Current Status*. Berlin, Heidelberg: Springer Berlin Heidelberg, 1996. OCLC: 851392298.

[65] M. Heurlin, N. Anttu, C. Camus, L. Samuelson, and M. T. Borgström, "In Situ Characterization of Nanowire Dimensions and Growth Dynamics by Optical Reflectance," *Nano Letters*, vol. 15, pp. 3597–3602, May 2015.

[66] N. Anttu, M. Heurlin, M. T. Borgström, M.-E. Pistol, H. Q. Xu, and L. Samuelson, "Optical Far-Field Method with Subwavelength Accuracy for the Determination of Nanostructure Dimensions in Large-Area Samples," *Nano Letters*, vol. 13, pp. 2662–2667, June 2013.

[67] N. Anttu, "Physics and design for 20% and 25% efficiency nanowire array solar cells," *Nanotechnology*, vol. 30, p. 074002, Feb. 2019.

[68] P. Kivisaari, Y. Chen, M.-E. Pistol, and N. Anttu, "Full optoelectronic simulation of nanowire LEDs: Effects of temperature," in *2017 International Conference on Numerical Simulation of Optoelectronic Devices (NUSOD)*, (Copenhagen, Denmark), pp. 109–110, IEEE, July 2017.

[69] N. Anttu, S. Lehmann, K. Storm, K. A. Dick, L. Samuelson, P. M. Wu, and M.-E. Pistol, "Crystal Phase-Dependent Nanophotonic Resonances in InAs Nanowire Arrays," *Nano Letters*, vol. 14, pp. 5650–5655, Oct. 2014.

[70] D. Verardo, F. W. Lindberg, N. Anttu, C. S. Niman, M. Lard, A. P. Dabkowska, T. Nylander, A. Månsson, C. N. Prinz, and H. Linke, "Nanowires for Biosensing: Lightguiding of Fluorescence as a Function of Diameter and Wavelength," *Nano Letters*, vol. 18, pp. 4796–4802, Aug. 2018.

[71] R. G. Hobbs, N. Petkov, and J. D. Holmes, "Semiconductor Nanowire Fabrication by Bottom-Up and Top-Down Paradigms," *Chemistry of Materials*, vol. 24, pp. 1975–1991, June 2012.

[72] M. Weismann, D. F. G. Gallagher, and N. C. Panoiu, "Accurate near-field calculation in the rigorous coupled-wave analysis method," *Journal of Optics*, vol. 17, p. 125612, Dec. 2015.

[73] L. Vivien, ed., *Handbook of silicon photonics*. Series in optics and optoelectronics, Boca Raton: CRC Press, Taylor & Francis Group, 2013.